SOUTHERN PLAINS
TRANSPORTATION CENTER

Quantifying Thermomechanical Fatigue of Hot Mix Asphalt: A Feasibility Study

Calvin M Stewart, Ph.D.

SPTC14.1-96-F

Southern Plains Transportation Center
201 Stephenson Parkway, Suite 4200
The University of Oklahoma
Norman, Oklahoma 73019

DISCLAIMER

The contents of this report reflect the views of the authors, who are responsible for the facts and accuracy of the information presented herein. This document is disseminated under the sponsorship of the Department of Transportation University Transportation Centers Program, in the interest of information exchange. The U.S. Government assumes no liability for the contents or use thereof.

Technical Report Document Sheet

<table>
<tr><td colspan="2">1. Report No.SPTC14.1-96</td><td>2. Government Accession No.</td><td>3. Recipient's Catalog No.</td></tr>
<tr><td colspan="3">4. Title and Subtitle

Quantifying Thermomechanical Fatigue of Hot Mix Asphalt: A Feasibility Study</td><td>5. Report Date: October 2018

6. Performing Organization Code</td></tr>
<tr><td colspan="3">7. Author(s)

Calvin M. Stewart</td><td>8. Performing Organization Report No.

SPTC 14.1-96</td></tr>
<tr><td colspan="3">9. Performing Organization Name and Address

Center for Transportation Infrastructure Systems
The University of Texas at El Paso
El Paso, Texas 79968-0516</td><td>10. Work Unit No.

11. Contract or Grant No.
DTRT13-G-UTC36</td></tr>
<tr><td colspan="3">12. Sponsoring Agency Name and Address

Southern Plains Transportation Center
201 Stephenson Pkwy, Suite 4200
The University of Oklahoma Norman, OK 73019</td><td>13. Type of Report and Period Covered

Final - 1/15/2016 – 05/15/2018

14. Sponsoring Agency Code</td></tr>
<tr><td colspan="4">15. Supplementary Notes</td></tr>
<tr><td colspan="4">16. Abstract

Highway agencies and the research community have struggled for many years to improve the repeatability of lab tests that characterize the fracture and fatigue properties of hot mix asphalt (HMA) materials. The major source of uncertainty stems from the fact that specimens grossly deviate from the requirements of solid and continuum mechanic; thus the test protocols and interpretation schemes are inaccurate. Even though this mismatch between theory and experiment is pragmatic and practical for day-to-day use, a systematic experimental-theoretical-numerical paradigm is needed to evaluate the fracture and fatigue resistance of HMA materials; especially when subjected to boundary conditions imposed by common lab tests. The outcome of this study are laboratory results that can be used with certainty and improved test specifications and procedures that can delineate material-, equipment-, and operator-related uncertainties. In this study, the feasibility of adapting state-of-the-art testing techniques are evaluated towards understanding better the problems of fracture and fatigue in HMA.</td></tr>
<tr><td colspan="2">17. Key Words
fracture, fatigue, asphalt, feasibility</td><td colspan="2">18. Distribution Statement

No restrictions. This publication is available at www.sptc.org and from the NTIS.</td></tr>
<tr><td>19. Security Classif. (of this report)
Unclassified</td><td>20. Security Classif. (of this page)
Unclassified</td><td>21. No. of Pages
138</td><td>22. Price</td></tr>
</table>

SI* (MODERN METRIC) CONVERSION FACTORS

APPROXIMATE CONVERSIONS TO SI UNITS

SYMBOL	WHEN YOU KNOW	MULTIPLY BY	TO FIND	SYMBOL
		LENGTH		
in	inches	25.4	millimeters	mm
ft	feet	0.305	meters	m
yd	yards	0.914	meters	m
mi	miles	1.61	kilometers	km
		AREA		
in^2	square inches	645.2	square millimeters	mm^2
ft^2	square feet	0.093	square meters	m^2
yd^2	square yard	0.836	square meters	m^2
ac	acres	0.405	hectares	ha
mi^2	square miles	2.59	square kilometers	km^2
		VOLUME		
fl oz	fluid ounces	29.57	milliliters	mL
gal	gallons	3.785	liters	L
ft^3	cubic feet	0.028	cubic meters	m^3
yd^3	cubic yards	0.765	cubic meters	m^3
		NOTE: volumes greater than 1000 L shall be		
		MASS		
oz	ounces	28.35	grams	g
lb	pounds	0.454	kilograms	kg
T	short tons (2000 lb)	0.907	megagrams (or "metric ton")	Mg (or "t")
		TEMPERATURE (exact degrees)		
°F	Fahrenheit	5 (F-32)/9 or (F-32)/1.8	Celsius	°C
		ILLUMINATION		
fc	foot-candles	10.76	lux	lx
fl	foot-Lamberts	3.426	$candela/m^2$	cd/m^2
		FORCE and PRESSURE or STRESS		
lbf	poundforce	4.45	newtons	N
lbf/in^2	poundforce per square inch	6.89	kilopascals	kPa

APPROXIMATE CONVERSIONS FROM SI UNITS

SYMBOL	WHEN YOU KNOW	MULTIPLY BY	TO FIND	SYMBOL
		LENGTH		
mm	millimeters	0.039	inches	in
m	meters	3.28	feet	ft
m	meters	1.09	yards	yd
km	kilometers	0.621	miles	mi
		AREA		
mm^2	square millimeters	0.0016	square inches	in^2
m^2	square meters	10.764	square feet	ft^2
m^2	square meters	1.195	square yards	yd^2
ha	hectares	2.47	acres	ac
km^2	square kilometers	0.386	square miles	mi^2
		VOLUME		
mL	milliliters	0.034	fluid ounces	fl oz
L	liters	0.264	gallons	gal
m^3	cubic meters	35.314	cubic feet	ft^3
m^3	cubic meters	1.307	cubic yards	yd^3
		MASS		
g	grams	0.035	ounces	oz
kg	kilograms	2.202	pounds	lb
Mg (or "t")	megagrams (or "metric ton")	1.103	short tons (2000 lb)	T
		TEMPERATURE (exact degrees)		
°C	Celsius	1.8C+32	Fahrenheit	°F
		ILLUMINATION		
lx	lux	0.0929	foot-candles	fc
cd/m^2	$candela/m^2$	0.2919	foot-Lamberts	fl
		FORCE and PRESSURE or STRESS		
N	newtons	0.225	poundforce	lbf
kPa	kilopascals	0.145	poundforce per square inch	lbf/in^2

*SI is the symbol for the International System of Units. Appropriate rounding should be made to comply with Section 4 of ASTM E380. (Revised March 2003)

Final Report For

Quantifying Thermomechanical Fatigue of Hot Mix Asphalt: A Feasibility Study

Calvin M. Stewart, Ph.D.

Center for Transportation Infrastructure Systems

The University of Texas at El Paso

El Paso, Texas 79968-0516

SPTC 14.1-96-F

Southern Plains Transportation Center

201 Stephenson Parkway, Suite 4200

Norman, Oklahoma 73019

Table of Contents

List of Tables

List of Figures

Executive Summary

Highway agencies and the research community have struggled for many years to improve the repeatability of lab tests that characterize the fracture and fatigue properties of hot mix asphalt (HMA) materials. The major source of uncertainty stems from the fact that specimens grossly deviate from the requirements of solid and continuum mechanic; thus the test protocols and interpretation schemes are inaccurate. Even though this mismatch between theory and experiment is pragmatic and practical for day-to-day use, a systematic experimental-theoretical-numerical paradigm is needed to evaluate the fracture and fatigue resistance of HMA materials; especially when subjected to boundary conditions imposed by common lab tests. This paradigm should accommodate the stochastic nature observed in HMA samples (i.e., the exact same constituents will always produce a unique HMA internal structure). The outcome of this study are laboratory results that can be used with certainty and improved test specifications and procedures that can delineate material-, equipment-, and operator-related uncertainties. In this study, the feasibility of adapting state-of-the-art testing techniques are evaluated towards understanding better the problems of fracture and fatigue in HMA. The goal is not to increase the complexity of current methods but to create the scientific breakthrough needed to better interpret them and ultimately improve reliability. This effort will produce a provisional standard test method for the fracture and fatigue of HMAs subjected to thermomechanical conditions.

1. Introduction

1.1. Problem Statement

The mechanical behavior of hot mix asphalt (HMA) is by nature stochastic where the constituent materials (crushed stone, sand, mineral filler, and asphalt binder) and mixing and compacting processes create a truly heterogeneous product. Efforts to evaluate the fracture and fatigue resistance of HMAs suffer from uncertainties observed in the results during experiments. The use of low-fidelity displacement measurement devices (such as extensometers and linear variable differential transformers, LVDTs) exacerbate uncertainty. The large size of aggregate particles relative to the dimensions of the specimens make the data interpretation based on the continuum and solid mechanics concepts inaccurate. These uncertainties further negatively impact the repeatability of tests that characterize the fracture and fatigue properties of HMAs.

Laid down HMA layers in the field are subject to thermomechanical fatigue (TMF) during their service lives where extreme weather can lead to embrittlement (cold weather) and/or healing effects (kneading from traffic coupled with hot weather). Thermomechanical fatigue experiments are needed to characterize the response of HMAs subject to these conditions. A new systematic fracture and fatigue resistance test program for HMA subject to thermal extremes must be developed. This collaborative effort between a mechanics and pavements expert while have a broader impact on the test methods and characterization techniques used in the southern plains region and national pavement industry.

1.2. **Background**

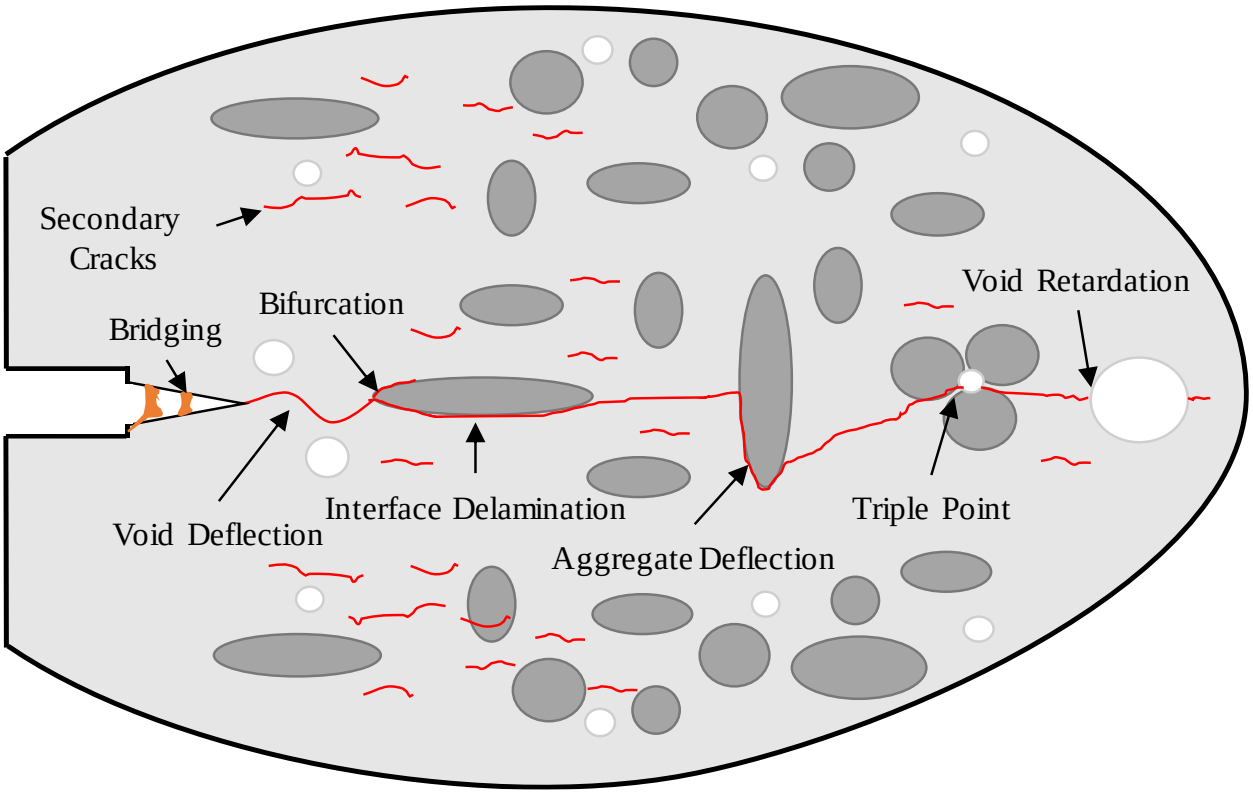

Figure 1.1 – Fracture in Hot Mixed Asphalts

1.2.1. **Fracture Mechanisms in Hot Mix Asphalt**

The fracture mechanisms observed in HMA are similar to those observed in other heterogeneous particulate composites where interfacial bond energy plays a large role in cracking phenomena [1]. The aggregates (particulates) consist of crushed stone (large), sand (fine), and mineral (filler) at different sizes and spatial distributions. The stone particles are brittle and exhibit an elastic-perfect plastic mechanical response. The sand and mineral filler act to increase density, achieve an optimum air-void content, and

provide load transfer between the larger stone particles. Asphalt acts as a binding agent and can contain up to 40% recycled asphalt pavement. The binder exhibits a linear viscoelastic response at low temperature and acts as a Newtonian fluid at high temperature [2]. The interaction of the constituents in the heterogeneous particulate composite produces a viscoelastic-viscoplastic response. The mechanisms of fracture include: friction between aggregates coated with binder, interlocking between the aggregates that is responsible for material dilation, and the energy dissipation of the bond between the binder elements (cohesion) and the aggregate-binder interfaces (adhesion) [3]. During cracking, the stress, strain, and damage zones are highly localized about the aggregates and cavities. The primary crack exhibits cracking bridging ahead of the crack tip and a traction free crack behind the crack tip as depicted in Figure 1.1 [4]. Crack bridging acts to blunt the crack tip where the stress concentration at the crack tip is reduced and the local equivalent stress is more evenly distributed across the damage zone such that fatigue resistance is increased. Secondary cracks often form in the vicinity of the primary crack but grow at a slower rate and have the possibility of arresting under cycling loading conditions. The dominant fracture mechanism in HMA is the nucleation and growth of microcracks within the binder and at the aggregate-binder interfaces [1]. Particulate sizes plays an integral role in the repeatability of fracture and fatigue tests where increased size will produce high variability in mechanical response due to an increased dependence on a limited number of meso-scale aggregate-binder interfaces to maintain mechanical integrity [5]. Society would benefit from knowledge concerning the evolution of defects, stress, and strain fields with in HMA with respect to

space and time. This knowledge would allow a better understanding of the 3D fracture mechanics of HMA.

(a) (b)

Figure 1.2 – Climate variability in the southern plains region (a) high temperature low humidity (b) low temperature and high humidity [6]

1.2.2. **Boundary Conditions**

Weather/Climate extremes can significantly impact surface transportation infrastructure. Within the southern plains region, extreme climate across the spectrum from subzero to triple digit temperature and high-low humidity are observed as depicted in Figure 1.2 [6]. Mechanical loads due to traffic can be low-cycle high-impulse observed on remote roads to high-cycle low-impulse observed during traffic congestion in major metropolitan areas. The boundary conditions that HMAs are subject to enable a complex multifaceted microstructural degradation process to occur. There are several types of boundary conditions that can contribute to microstructural degradation. When subject to a constant uniaxial tensile load at temperature above the “limiting creep activation temperature,” HMAs exhibit creep deformation where irreversible plastic deformation accumulates with

primary, secondary, and tertiary creep regimes [3]. Creep cracks grow, where microcracks and voids form within the binder and along the aggregate-binder interfaces. When subject to constant uniaxial compressive load at elevated temperatures, HMAs exhibit a healing phenomenon where pre-existing microcracks and voids close (cohesion) and aggregate-binder interfaces heal (adhesion) due to Newtonian binder flow [7]. Healing of HMA is dependent on the activation energy of the binder, capillary flow through cracks, self-diffusion of molecules across the crack interface and duration and confinement [8]. When subject to a low temperature thermal load, fracture due to thermal stresses can occur at a critically low temperature called the “fracture temperature” [9]. When subject to elevated temperature for long duration, aging is enhanced where the oxidative and polarity state of the HMA evolves having a significant impact on chemical, mechanical, and physical properties; where HMA becomes more susceptible to fracture, fatigue, and moisture penetration [10].

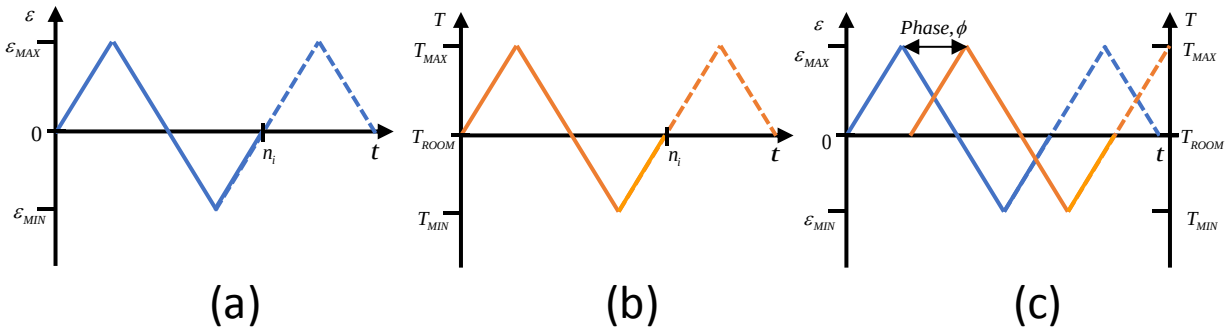

Figure 1.3 – Fatigue Cycling (a) Thermal (b) Mechanical and (c) Thermomechanical

Of particular interest is the mechanical response of HMAs subject to cycling boundary conditions as depicted in Figure 1.3. During thermal cycling with constrained displacement, degradation is driven by the debonding of aggregate-binder interfaces due to thermal contraction. During mechanical fatigue under isothermal room temperature conditions, degradation is driven by binder microcracking and aggregate-binder interface debonding. The application of both thermal and mechanical cycling called "thermomechanical fatigue" result in complex constitutive, microstructural degradation, and cracking phenomena [11]. The dominant damage mechanism during thermomechanical fatigue depends on load, frequency, temperature, dwell time, mean stress, stress ratio, geometry, etc. [12-17]. In-service, HMAs are subject to thermomechanical fatigue, where multiple microstructural degradation mechanisms contribute to the ***"Mechanical State"*** of the material. In HMAs, thermal and mechanical cycles are out of phase, where a high number of mechanical cycles will occur during one thermal cycle (24 hours). Methods are needed to evaluate the thermomechanical fatigue of HMAs towards a more reliable prediction of the weather/climate resistance of transportation materials. This effort would help to mitigating infrastructure maintenance costs.

1.2.3. **Summary**

The thermomechanical boundary conditions that HMAs are subjected to during service lead to complex mechanical histories. The constitutive models currently employed are based on low-fidelity characterization that precludes these models from properly

accommodating the mechanics observed during TMF. This research effort is a feasibility study for an advanced experimental, theoretical, and numerical paradigm to address the thermomechanical fracture and fatigue of HMAs It will generate new knowledge and produce two trained professionals prepared for a career in the pavement industry.

1.3. Objective and Scope of Study

The main goal of this project is to perform a feasibility study to assess the thermomechanical fatigue resistance of HMA. To achieve this goal, the following objectives must be addressed:

1. to identify existing fracture resistance test standards and compare the repeatability and reproducibility of these standard towards identify the best practices;
2. to evaluate the effect of specimen thickness on the fracture resistance of a single mix of HMA;
3. to develop a fatigue resistance standard to assess the fatigue resistance of an HMA at various temperatures;

1.4. Outline

The body of this report is separate into three distinct chapters that response to the three research objectives. The second chapter focuses on comparing existing fracture

resistance test standards at room temperature. The results of these experiments were published in the Journal of Engineering Fracture Mechanics [18]. The third chapter focuses on evaluating the effect of specimen thickness on fracture resistance. The results of these experiments were published in the Journal of Construction and Building Materials [19]. The four chapter focuses on developing a fatigue resistance standard for HMAs and evaluate the fatigue resistance of a single HMA at three temperatures. The results will be published in an academic journal to be determined after the submission of this report.

1.5. References

[1] Roque, R., Zou, J., and Hernando, D., 2015, “5 - Cracking mechanisms in asphalt mixtures”, Advances in Asphalt Materials, Woodhead Publishing, Oxford, pp. 135-167.

[2] Krishnan, J. M., and Rajagopal, K. R., 2005, “On the Mechanical Behavior of Asphalt,” Mechanics of Materials, 37(11), pp. 1085-1100.

[3] Tashman, L., 2003, Microstructural Viscoplastic Continuum Model for Asphalt Concrete, Dissertation, Texas A&M University, College Station, TX.

[4] Anderson, T. L., 2005, Fracture Mechanics: Fundamentals and Applications, Second Edition, CRC Press.

[5] Asi, I. M., 2005, “Laboratory Comparison Study for the Use of Stone Matrix Asphalt in Hot Weather Conditions,” Construction and Building Materials, 20(10), pp. 982-989.

[6] Southern Plain's Transportation Center Website, http://www.sptc.org/

[7] Dessouky, S. H., 2005, Multiscale Approach for Modeling Hot Mix Asphalt, Dissertation, Texas A&M University, College Station, TX.

[8] Dai, Q., Wang, Wang, Z., and Hasan, M.R.M., 2013, “Investigation of Induction Healing Effects on Electrically Conductive Asphalt Mastic and Asphalt Concrete Beams through Fracture-Healing,” Construction and Building Materials, 49, pp. 729-737.

[9] Das, P. K., Jelagin, D., and Birgission, B., 2013, “Evaluation of the Low Temperature Cracking Performance of Asphalt Mixtures Utilizing HMA Fracture Mechanics,” Construction and Building Materials, 47, pp. 594-600.

[10] Walubita, L. F., Florez, B. L., and Alvarez, A. E., 2012, “Evaluation of HMA Cracking Resistance As A Function of Laboratory Aging Based on the Direct-Tension Test,” Revista EIA, Escuela de Ingeniería de Antioquia, Medellín, 17, pp. 209-224.

[11] Lemaitre, J., and Desmorat, R., 2005, Engineering Damage Mechanics:Ductile, Creep, Fatigue, and Brittle Failures, Springer-Verlag, Berlin, German.

[12] Zhang, X., Tu, S. T., Xuan, F., 2014, “Creep-Fatigue Endurance of 304 Stainless Steel,” Theoretical and Applied Fracture Mechanics, 71, pp. 51-66.

[13] Manson, S. S., and Halford, G. R., 2009, Fatigue and Durability of Metals at High Temperatures, ASM International, Materials Park, OH.

[14] Evans, W. J., Jones, J. P., and Williams, S., 2005, “The Interactions Between Fatigue, Creep and Environmental Damage in Ti 6246 And Udimet 720Li,” International Journal of Fatigue, 27(10-12), pp.1473-1484.

[15] Grover, P.S. and Saxena, A., 1999, “Modeling the effect of creep-fatigue interaction on crack growth,” Fatigue and Fracture of Engineering Materials and Structures, 22(2). pp.111-122.

[16] Goswami, T., 1999, “Low Cycle Fatigue –Dwell Effects and Damage Mechanisms,” International Journal of Fatigue, 21(1), pp. 55-76.

[17] Plumtree. A., Tang, N. Y., 1989, “Effect of Hold-Time Damage on High Temperature Fatigue Behaviour,” Fatigue Fract. Engng Mater. Struct., 12(5), pp. 377-386.

[18] Stewart, C. M., Reyes, J.G., and Garcia, V. M., 2017, “Comparison of Fracture Test Standards for a Super Pave Dense-Graded Hot Mix Asphalt,” Engineering Fracture Mechanics, 169. doi:10.1016/j.engfracmech.2016.10.016

[19] Stewart, C. M., Oputa, C.W., and Garcia, E., 2018, “Effect of Specimen Thickness on Fracture Resistance of Hot Mix Asphalt in Disk-Shaped Compact Tension (DCT) Configuration,” Construction and Building Materials, 160, pp. 487-496. doi:10.1016/j.conbuildmat.2017.11.041

2. Comparison of Fracture Test Standards for a Super Pave Dense-Graded Hot Mix Asphalt

Calvin Maurice Stewart[1*], Jesús Gerardo Reyes[1], and Victor M. Garcia[2]
[1]Department of Mechanical Engineering, The University of Texas at El Paso
[2]Department of Civil Engineering, The University of Texas at El Paso

Published in the Journal of **Engineering Fracture Mechanics, Volume 169**

2.1. Abstract

The objective of this work is to compare the semi-circular bend (SCB) and disc-compact tension (DCT) fracture tests for asphalt-aggregate mixtures. Fracture tests are performed. Statistical analysis, digital image correlation, and 3D scans show that the SCB tests measure a low fracture resistance with a high coefficient of variation due to stress concentrations and plasticity developing at the anvil contact point. The DCT test is found to measure a high fracture resistance with a low coefficient of variation. The DCT tests is determined to provide a superior measurement of fracture resistance. Evidence concerning the physical problems with SCB is provided.

2.2. **Graphical Abstract**

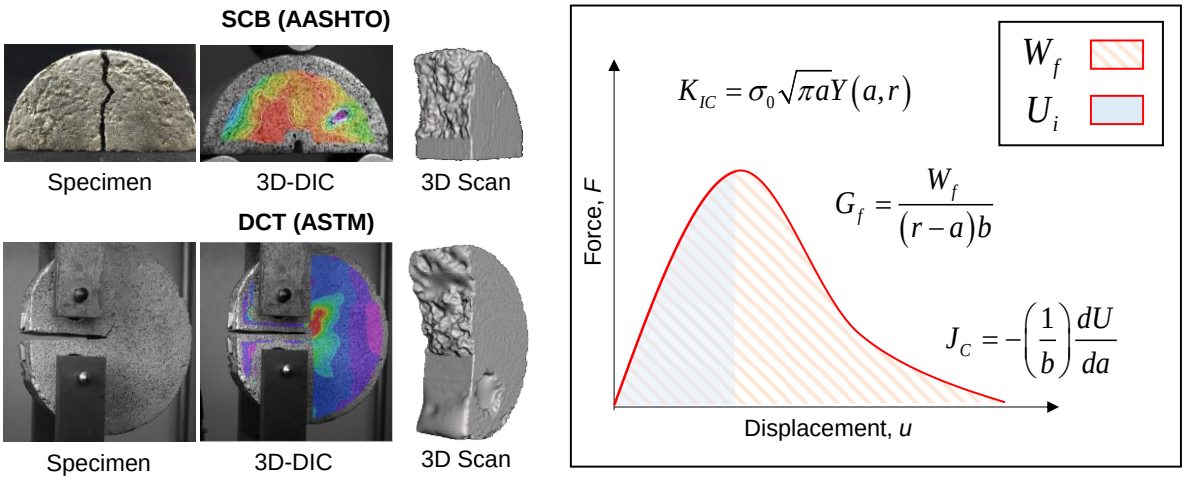

Figure 2.1 – Graphical Abstract

2.3. **Nomenclature**

Acryonm	**Description**
HMA	hot mix asphalt
DCT	disk-shaped compact tension
SCB	semi-circular bending
LEFM	linear elastic fracture mechanics
EPFM	elastic-plastic fracture mechanics
COV	coefficient of variation
SP-D	dense grade superpave
3D-DIC	three-dimensional digital image correlation
G_f	fracture energy
K_{IC}	fracture toughness
J_c	critical strain energy release rate
AV%	air void percentage
a	notch depth

Acryonm	Description
$P_{\max}$	peak load
W_f	work of fracture
A_{lig}	ligament area
$Y_{I(0.8)}$	dimensionless geometric factor
U	strain energy to failure
ε_{yy}	strain in the vertical direction
ε_{xx}	strain in the horizontal direction

2.4. Introduction

The accumulation of cracks in HMA layers is often due to damage induced by repeated traffic loading and climatic effects: defined as *fatigue cracking* [20]. The cracking of HMA layers is one of the predominate forms of distress observed in flexible pavements, that significantly reduce service life [21]. An HMA overlay must have a balance of both good rut and crack resistance properties, to perform well in the field [22-24]. Over the past decade, HMA's designed in Texas have been modified to minimize the deformation of roads and moisture susceptibility of new mixtures using the Hamburg rutting test. This test applies vertical deformation to a specimen simulating constant traffic loading. Less attention has been paid to the cracking resistance of the new HMA surfaces. Stiffer binders and good stone-to-stone contact may improve rut resistance but it may also reduce the mix flexibility and cracking resistance [22].

The pavement industry is moving towards physics-based computational models as opposed to data-founded models for life prediction. Experimental fracture mechanics has become the de facto choice of many scientists and researchers in this area to obtain physical measures of fracture resistance. Much effort has been directed towards the development of testing and analysis methods to study the cracking mechanisms of asphalt pavement [23-28]. To date, several performance tests have been proposed to determine the cracking resistance of HMAs such as the flexural fatigue, dissipated creep strain energy, indirect tension, Texas overlay, single-edge notch bend, disk-shaped compact tension (DCT), and semi-circular bend (SCB) tests [29]. So far, the definitive or

best fracture test method to determine the cracking resistance of asphaltic materials has yet to be determined.

Hot mix asphalts exhibit a viscoelastic plastic response, where cracks tend to grow through the asphalt binder and along the asphalt-aggregate interfaces. This tortuous cracking process creates a large plastic zone that exceeds the small-scale plasticity limitation of the linear elastic fracture mechanics (LEFM) approach. The fracture toughness K_{IC} has continued to be used to analyze the fracture resistance of HMAs despite the deficits of LEFM [30-34]. The LEFM approach is assumed reasonable if the test temperature is 10°C below the performance grade lower limit of the asphalt binder and the modulus changes less than 5% for the duration of the test. These conditions are rarely met. In practice HMAs are subjected to a wider temperature range. As an alternative, elastic-plastic fracture mechanics (EPFM) has been introduced to measure the fracture resistance of HMAs. In EPFM, fracture resistance is measured using the energy of fracture (i.e. the energy required to open a crack).

The EPFM-based DCT and SCB tests have been identified as two of the most popular approaches to fracture resistance measurement of HMAs [35]. The prevalence of SCB testing stems from its simplicity, repeatability, and consistency [28]. Recent studies by the Louisiana Transportation Research Center have shown that the SCB test is promising in evaluating the cracking resistance of HMAs [26]. They concluded that specimens with a pre-fabricated notch are more suitable at measuring the cracking

properties of asphalt mixtures. The SCB test exhibits certain advantages as a cracking resistance predictor:

a) different notch depths, notch orientations, and specimen positioning can be introduced; hence, mixed-mode fracture properties can be evaluated directly;
b) the test setup and procedure are fairly simple and rapid;
c) the SCB specimens can be prepared directly from cylindrical samples obtained from standard cores prepared in a super pave gyratory compactor or can be taken from field cores; and
d) multiple specimens can be obtained from one field core, reducing the error caused by the heterogeneity among cores [36].

The main disadvantages of the SCB test is that it is susceptible to operator error where a small misalignment of the specimen will lead to mixed-mode fracture and fracture resistance measurements can exhibit low repeatability. The DCT test exhibits certain advantages as a cracking resistance predictor:

a) according to the National Cooperative Highway Research Program, the DCT test often produces the lowest coefficient of variation (COV) of all HMA fracture tests with a COV in the 10-15% range [37];
b) the DCT test provides a larger fracture area which is important because it reduces the impact that a single large aggregate or zone of weakness might have on the overall fracture resistance of the HMA [38];

c) a specimen can be prepared directly from a cylindrical sample obtained from standard cores prepared in a super pave gyratory compactor or can be taken from field cores.

The main disadvantage of the DCT test is that it is more laborious to machine DCT specimen in comparison to other standard geometry.

Dense grade super-paves (SP-Ds) have aggregate size distributions that provide a high degree of compaction resulting in higher fatigue and fracture strength [39]. Chen and Huang conducted indirect tension tests on a SP-D mixture and observed that the average tensile strength is 1.08 MPa with variability of 0.1 MPa. Increasing the coarse aggregate angularity from zero to one hundred percent reduced the tensile strength of SP-D [40]. Wu and colleagues conducted SCB tests on thirteen SP-D mixtures at room temperature (25°C). The SP-Ds with lower tensile strength offer higher fracture resistance and vice versa (from 0.57 to 1.53 $\mathrm{kJ \cdot m^{-2}}$). Kim and colleagues conducted several DCT tests on dense grade HMA and recorded an average 3 kN peak load, .344 $\mathrm{kJ \cdot m^{-2}}$ fracture energy, and young's modulus of 14.2 GPa at -10°C [30]. Braham et al. conducted a DCT-based study on the effect of the constituents on the fracture energy of twenty-eight HMAs at 2°C below, 10°C above, and 22°C above the lower temperature grade. It was concluded that the binder, air void content, and dominant aggregate type have a large influence on the fracture energy values calculated at high temperature, but not at mid or low temperature [31]. A review of literature finds that few studies that

compare and contrast the accuracy and repeatability of SCB and DCT test standards for HMAs have been performed.

In this study, the room temperature fracture resistance of a SP-D HMA is evaluated using two competing SCB test standards and a DCT test standard. The AASHTO TP105 standard for SCB is performed using ten specimens with the standard notch depth (24 ± 1.5 mm) to calculate the fracture energy, G_f, and fracture toughness, K_{IC} [41]. The provisional AASHTO TPXXX standard for SCB is performed using five repetitions of three specimens with different notch depths (24, 30, 36 ± 1.5 mm) to calculate the critical energy release rate, J_c [42]. The ASTM D7313 standard for DCT is performed using four specimens with a standard notch depth (62.5 ± 2.5 mm) to calculate the fracture energy, G_f [43]. The fracture resistance parameters of SCB and DCT standards are compared. The digital image correlation (DIC) technique is employed to analyze the strain field near the crack tip. Fracture area analysis using a 3D scanner is performed to compare the fracture area resulting from SCB and DCT tests.

Table 2.1. Summary of SP-D HMA properties

Location	Abilene, TX
Asphalt Source	Alon
Asphalt Performance Grade	70-22
Binder Substitution	64-22
Binder Percent, %	5.3
Asphalt Specific Gravity	1.051
%Reclaimed Asphalt Pavement	8
%Reclaimed Asphalt Shingles	2

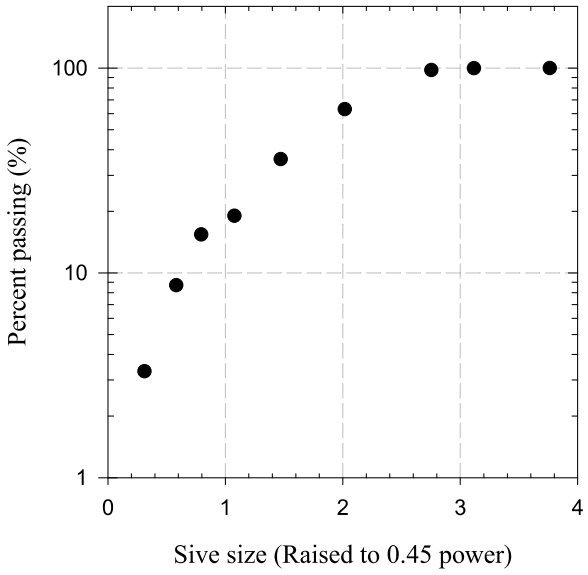

Figure 2.2. Gradation of aggregates in SP-D HMA

2.5. Materials And Test Methods

2.5.1. Material

A dense-grade superpave (SP-D) hot mix asphalt (HMA) is the subject material. The material was sourced in Abilene, TX and transported to the UTEP Center for Transportation Infrastructure Systems for specimen preparation. The properties of the SP-D are summarized in Table 2.1. The gradation of the SP-D mix is depicted in Figure 2.2. The typical distribution of the aggregates, mastic, and binder in the SP-D mix is shown in Figure 2.3.

Figure 2.3. SP-D HMA specimen (a) disk, (b) SCB, and (c) DCT

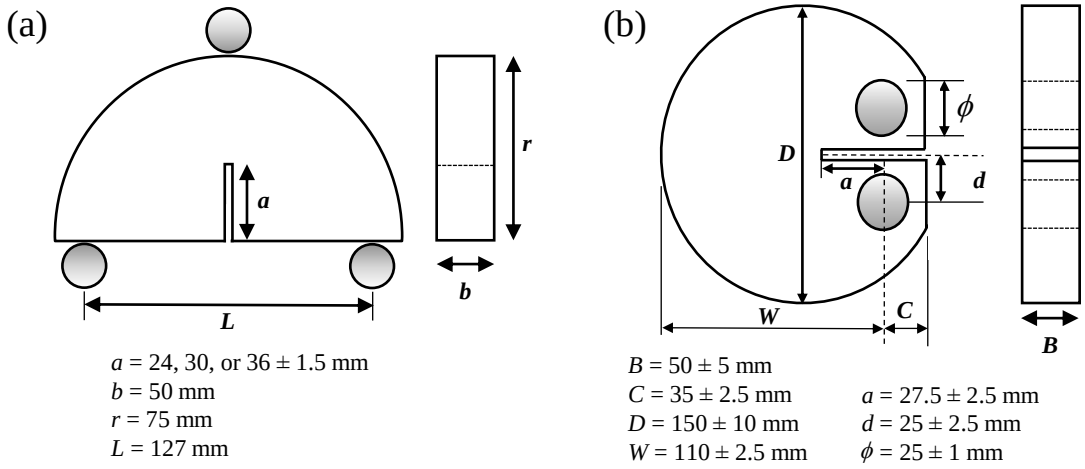

a = 24, 30, or 36 ± 1.5 mm
b = 50 mm
r = 75 mm
L = 127 mm

B = 50 ± 5 mm
C = 35 ± 2.5 mm
D = 150 ± 10 mm
W = 110 ± 2.5 mm
a = 27.5 ± 2.5 mm
d = 25 ± 2.5 mm
ϕ = 25 ± 1 mm

Figure 2.4. Schematic and dimensions of (a) SCB and (b) DCT specimen

2.5.2. **Specimen Preparation**

The SCB and DCT specimens are trimmed from standard 150 mm diameter by 114 mm thick briquettes compacted with a superpave gyratory compactor in accordance with AASHTO T312 (ASTM D6925) [32,33]. After the briquette reaches room temperature, a disk shape specimen is trimmed from the middle of the briquette and the disk is quality checked for an air-void percentage (AV%) target of 7±1.0%. A typical disk specimen is shown in Figure 2.3a. Two SCB specimens as depicted in Figure 2.3b can be extracted

from a disk. One DCT specimen as depicted in Figure 2.3c can be extracted from a disk. A schematic and dimensions of the SCB and DCT specimens is provided in Figure 2.4a and b respectively.

2.5.3. Mechanical Test Equipment

The SCB and DCT tests were conducted using an INSTRON 5969 Table-Top Universal Test System. This electromechanical frame is capable of 0.001 to 600 mm/min displacement rates and equipped with a 50kN load cell. The data captured from the INSTRON machine during tests included time, load, and load-line displacement. Specimens were exposed to the laboratory room temperature of 27°C during testing.

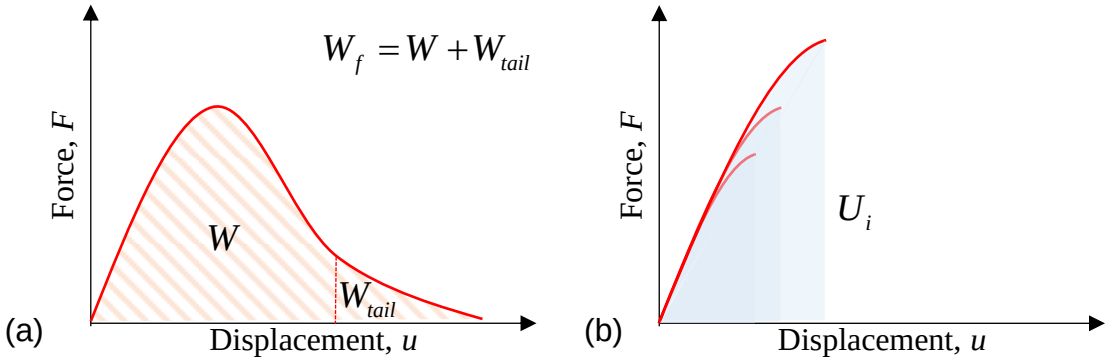

Figure 2.5. Strain energy measurement for SCB and DCT (a) G_f and SCB (b) J_c

2.6. Semi-Circular Bend (SCB) Test

The AAHSTO TP105 and provisional AAHSTO TPXXX test standards for SCB specimen are based on the calculation of the fracture energy, G_f and critical strain energy release rate, J_c respectively [41,42]. It is important to note that both quantities G_f and J_c are

equal representations of the critical *J*-integral. The G_f represents the single specimen method proposed by Rice [44] while J_c represents the multiple specimen method proposed by Begley and Landes [45]. The different nomenclature is due to inconsistency in the test standards.

A schematic of the test setup for SCB testing is shown in Figure 2.4a. For both SCB standards, the specimen is mounted into a three-point bending fixture and subjected to compressive displacement. The three-point bend fixture consists of a top loading anvil and two support anvils under the specimen with a diameter of 5 mm. No seating load is applied to the specimen; however, the anvil is placed into neutral contact with the specimen just before testing. Tests are performed with a constant displacement rate of 5mm/min at a room temperature of 27°C. The test is stopped once the specimen has completely fractured.

2.6.1. **AASHTO TP105**

The AASHTO TP105 SCB standard calculates the fracture energy, G_f using the single-specimen geometry-specific solution for the J_c of a three-point bending specimen originally proposed by Rice and adopted by RILEM TC 50-FMC [41,44,46]. The fracture energy, G_f is a fracture mechanics concept that represents the amount of energy required to create a unit surface area of a crack. The fracture energy is obtained using the work of fracture, W_f (total area under the load versus load-line displacement curve) depicted in Figure 2.5a. The fracture energy, G_f is computed as follows

(1) $$G_f = \frac{W_f}{A_{lig}}, \quad A_{lig} = (r-a)b;$$

where G_f is the fracture energy ($\mathrm{kJ \cdot m^{-2}}$), W_f is the work of fracture (J), A_{lig} is the ligament area (mm^2), r is the specimen's radius (mm), a is the notch depth (mm), and b is the specimen thickness (mm). It should be noted that a unit conversion is needed to calculate G_f using the given units.

The AASHTO TP105 standard also provides a procedure for calculating the fracture toughness, K_{IC} ($\mathrm{MPa \cdot m^{0.5}}$) [41]. The fracture toughness, K_{IC} is defined as the stress intensity factor corresponding to the initiation of the crack. Fracture toughness, K_{IC} is computed as follows

(2) $$K_{IC} = Y_{I(0.8)}\sigma_0\sqrt{\pi a}$$

where $Y_{I(0.8)}$ is the dimensionless geometric factor, σ_0 is the applied stress, and a is the notch depth. The applied stress is calculated as $\sigma_0 = P_{\max}/2rt$ where $P_{\max}$ is the peak load, and r and t are the specimen radius and thickness respectively. The dimensionless geometric factor, $Y_{I(0.8)}$ is calculated using the following

(3) $$Y_{I(0.8)} = 4.782 + 1.219\left(\frac{a}{r}\right) + 0.063\exp\left[7.045\left(\frac{a}{r}\right)\right]$$

where a is the notch depth (mm) and r is the specimen's radius (mm) [47,48].

2.6.2. **AASHTO TPXXX**

The provisional AASHTO TPXXX SCB standard calculates the critical strain energy release rate, J_c, using the non-geometry specific solution to determine J_c [45,51]. This method requires multiple specimens to calculate J_c as proposed by Begley and Landes [45]. The critical strain energy release rate is obtained by determining the change in strain energy to failure, U with respect to notch depth, a. The strain energy to failure, U is calculated as the strain energy up to the peak load as depicted in Figure 2.5b. The critical strain energy release rate, J_c is computed as follows

$$J_c = -\left(\frac{1}{b}\right)\frac{dU}{da} \tag{4}$$

where b is the thickness (mm), a is the notch depth (mm), U is the strain energy to failure (J), and dU/da is the change of strain energy with notch depth (kN). It should be noted that a unit conversion is needed to calculate J_c using the given units.

2.7. **Disk-Shaped Compact Tension (DCT) Test**

The ASTM D7313 DCT standard calculates the fracture energy, G_f using a single-specimen geometry-specific solution [43]. A schematic and dimensions of a DCT specimen is shown in Figure 2.4b. A seating load of 0.2 kN (45 lbf) is applied. Tests are performed with a constant crack mouth opening displacement of 0.017 mm/s at a room temperature of 27°C. The test is stopped when the post-peak load drops by 22 lbf. The fracture energy, G_f for DCT is calculated similar to [Eq. (1)] for SCB as follows

(5) $$G_f = \frac{W_f}{B \cdot (W - a)}$$

where W_f is the work of fracture (J) depicted in Figure 2.5a, B is the thickness (mm), and $(W - a)$ is the initial ligament length (mm).

2.8. 3D Digital Image Correlation

Three-dimensional digital image correlation (3D DIC) is performed using a Correlated Solutions VIC-3D DIC system. Using the VIC-3D software, the surface displacements (*u*, *v*, and *w*) can be captured. These displacements are then processed to calculate the strain vector and principal strain. Before correlation, photos of a calibration square are taken to provide a physical reference of pixel distances. Next, specimens are primed with a randomly applied speckle pattern and inserted into the test frame. The speckles act as reference points. Tunable LED lights are focused on the specimen to increase the contrast of captured photographs and subsequently increase the accuracy of digital image correlation.

2.9. 3D Surface Scanning

The fractured specimen are 3D scanned to produce a 3D CAD replication of the fracture surface using a Makerbot Digitizer 3D Scanner. The scanner has a nominal dimensional accuracy of ±2 mm and detail resolution of 0.5 mm. This device uses two lasers and a rotating platform to generate a 3D dimensional replication of the surface of 3D objects. The Makerware software, exports a stereo lithography format file (.STL). The AutoDesk

MeshMixer software is employed to analyze the physical features of the 3-D .STL files. The 3D scanner and software introduce error into the fracture area measurement; however, considering the size of the available fracture area (in all cases >2500mm^2) and resolution of the 3D scanner (0.5 mm) it is determined that this error will not have a significant impact on the fracture area recorded.

2.10. **Results And Discussion**

2.10.1. **SCB - AASHTO TP105**

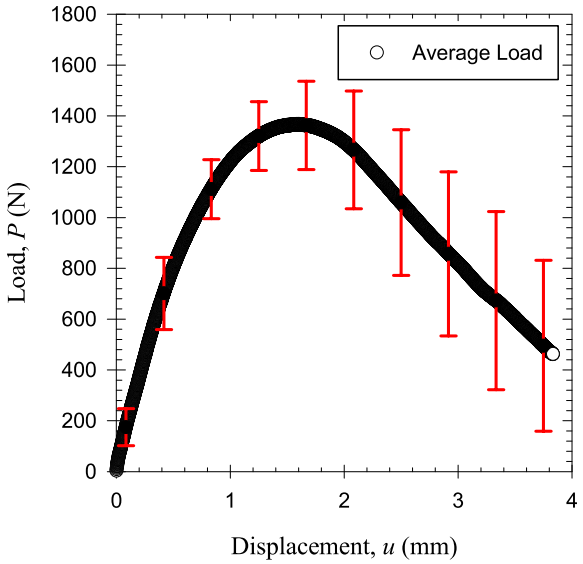

Figure 2.6. Average load-displacement curve for 24±1.5mm SCB specimens according to AASHTO TP105

The AASHTO TP105 SCB test method was performed on ten 24 mm specimens to measure the fracture energy, G_f and fracture toughness, K_{IC}. The average load versus load-line displacement curve of the ten SCB specimens is depicted in Figure 2.6. Error bars of one standard deviation were added to illustrate the repeatability of the tests. The error bars increase with strain after the peak load has been reached. This indicates decrease repeatability post the peak load.

The resulting fracture energy and toughness calculated using AASHTO TP105 are summarized in Table 2.2. The average peak load, work of fracture, fracture energy, and fracture toughness were calculated as 1400 N, 1.57 J, 0.595 $\mathrm{kJ \cdot m^{-2}}$, and 0.287 $\mathrm{MPa \cdot m^{0.5}}$ respectively. Fracture toughness, K_{IC} presented the lowest COV value at 12.7% while the COV of fracture energy, G_f is relatively high at 26.9%. Applying one standard deviation, the fracture energy, G_f should vary between 0.435-0.755 $\mathrm{kJ \cdot m^{-2}}$. These results are comparable to those established by Wu and colleagues for thirteen superpave mixtures, with the room temperature SCB-calculated fracture energy, G_f ranging from 0.57 to 1.53 $\mathrm{kJ \cdot m^{-2}}$ [9].

Table 2.2. Fracture energy G_f measured for SCB specimen according to AASHTO TP105

Specimen Name	AV%	Notch Depth, a (mm)	Peak Load, $P_{\max}$ (N)	Work of Fracture, W_f (J)	Fracture Energy, G_f $(\mathrm{kJ \cdot m^{-2}})$	Fracture Toughness, K_{IC} $(\mathrm{MPa \cdot m^{0.5}})$
11A	6.5	24	1259	1.32	0.499	0.257
11B	7.0	24	1572	1.90	0.717	0.320
12A	7.1	24.4	1184	1.05	0.398	0.244
12B	7.2	22.9	1308	1.36	0.502	0.257
13A	7.3	25.4	1394	1.28	0.497	0.297
13B	7.3	24.1	1488	1.62	0.614	0.304
14A	7.5	24.1	1516	1.56	0.591	0.310
14B	7.5	24.1	1716	2.38	0.898	0.351
15A	8.0	24.5	1157	1.18	0.451	0.240
15B	7.8	24	1408	2.09	0.786	0.287
Average	7.3	24	1400	1.57	0.595	0.287
St. Dev.	0.4	1	178	0.43	0.160	0.037
COV %	5.8%	2.5%	12.7%	26.9%	26.9%	12.7%

2.10.2. SCB - AASHTO TPXXX

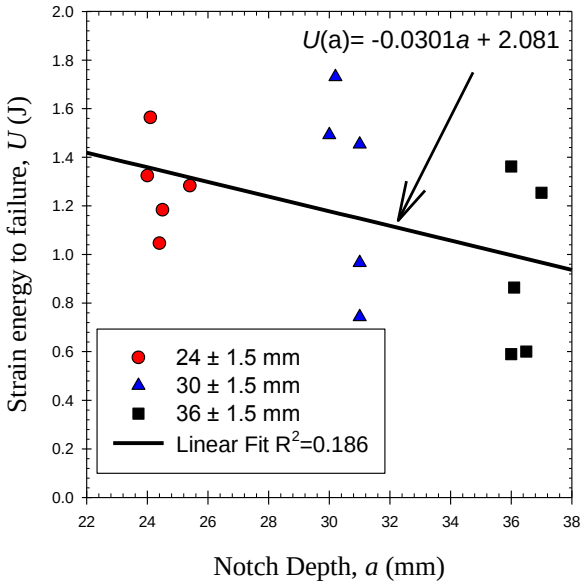

6

Figure 2.7. Strain energy to failure vs notch depth plot according to provisional AASHTO TPXXX

The provisional AASHTO TPXXX SCB test method was performed using three notch depths (24, 30, 36 ± 1.5 mm). The test for each notch depth was repeated five times to assess repeatability. The strain energy to failure, U was calculated for all specimen (see Figure 2.5b) and plotted against the notch depth to compute the change of strain energy, dU/da. The resulting plot is depicted in Figure 2.7. A linear function used to determine the change of strain energy, produced a low coefficient of determination, R^2 of 0.186. This low value indicates significant scatter in the experiments. The supporting

parameters to determine the critical strain energy release rate, J_c are summarized in Table 2.3. The J_c was calculated as 0.593 $\mathrm{kJ \cdot m^{-2}}$. This value compares well to the room temperature SCB-calculated J_c of a control superpave obtained by Mull and colleagues at 0.540 $\mathrm{kJ \cdot m^{-2}}$ [33].

Table 2.3. Critical strain energy release rate, J_c measured for SCB specimen according to provisional AASHTO TPXXX

Specimen Name	AV%	Notch Depth, a (mm)	Peak Load, $P_{\max}$ (N)	Strain Energy to Failure, U (J)	Change of Strain energy, dU/da (kN)	Critical Strain Energy Release Rate, J_c ($\mathrm{kJ \cdot m^{-2}}$)
11A	6.5	24.00	1259	1.324	-0.0301	0.593
12A	7.1	24.40	1184	1.046	-0.0301	0.593
13A	7.3	25.40	1394	1.283	-0.0301	0.593
14A	7.5	24.10	1516	1.564	-0.0301	0.593
15A	8.0	24.50	1157	1.183	-0.0301	0.593
18A	7.5	30.20	1624	1.731	-0.0301	0.593
18B	7.6	31.00	1499	1.453	-0.0301	0.593
20A	7.4	30.00	1571	1.493	-0.0301	0.593
22B	7.8	31.00	1029	0.966	-0.0301	0.593
25A	7.5	31.00	1018	0.744	-0.0301	0.593
25B	7.2	37.00	1475	1.254	-0.0301	0.593
26A	7.6	36.10	1047	0.864	-0.0301	0.593
26B	6.2	36.00	1315	1.362	-0.0301	0.593
27A	7.2	36.50	771	0.600	-0.0301	0.593
27B	7.4	36.00	731	0.589	-0.0301	0.593

2.10.3. **DCT - ASTM D7313**

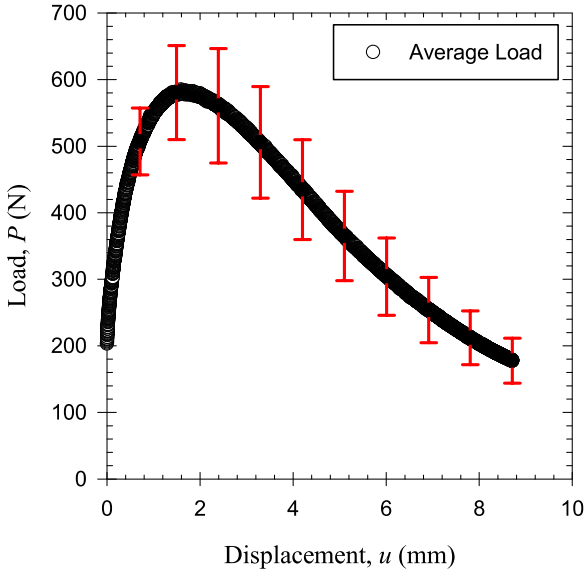

Figure 2.8. Average load-displacement curve for the DCT specimens according to ASTM D7313

The ASTM D7313 DCT test method was performed on four 62.5 mm notched specimens to measure the fracture energy, G_f. The average load versus load-line displacement curve of the four SCB specimens is depicted in Figure 2.8. Error bars of one standard deviation were added to illustrate the repeatability of the tests. The error bars decrease after the peak load has been reached suggesting good repeatability.

The resulting fracture energy, G_f calculated using ASTM D7313 are summarized in Table 2.4. The average peak load, work of fracture, and fracture energy are 632 N, 3.37 J, and 0.805 $\mathrm{kJ \cdot m^{-2}}$ respectively. The fracture energy, G_f has a low COV of 13.3%.

Applying one standard deviation, the fracture energy, G_f should vary between 0.698-0.912 $\mathrm{kJ \cdot m^{-2}}$.

Table 2.4. Fracture energy, G_f measured for DCT specimens according to ASTM D7313

Specimen Name	AV%	Peak Load, P_{max} (N)	Work of Fracture, W_f (J)	Fracture Energy, G_f ($\mathrm{kJ \cdot m^{-2}}$)
4D	6.2	691.06	2.923	0.698
5D	6.5	653.46	3.984	0.951
7D	6.7	643.30	3.359	0.802
10D	6.1	541.08	3.213	0.767
Average	6.38	632.22	3.370	0.805
STD	0.28	64.14	0.448	0.107
COV %	4.3%	10.1%	13.3%	13.3%

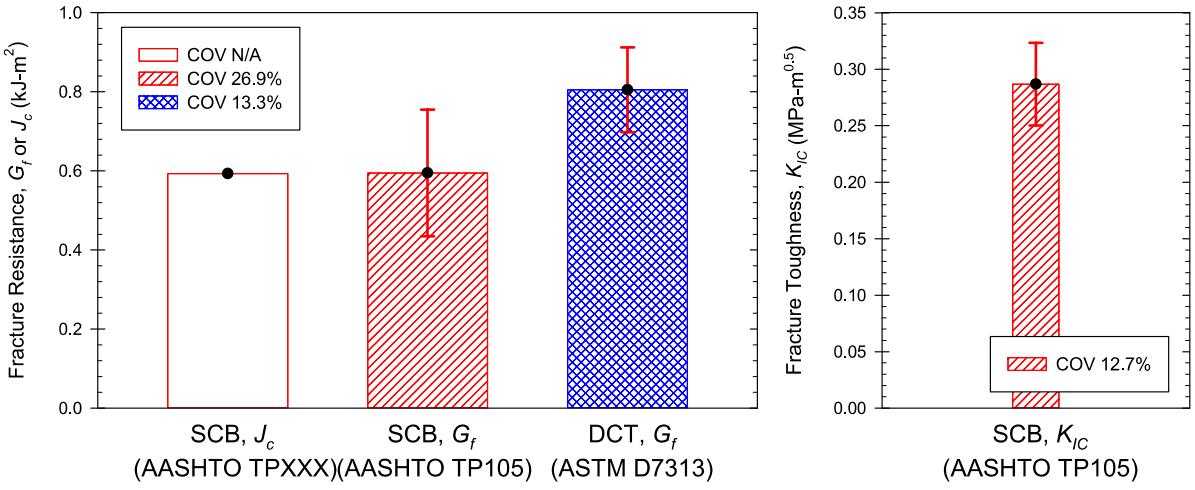

Figure 2.9. Comparison of fracture resistance properties of SCB and DCT test standards

2.10.4. SCB (AASHTO TP105) versus SCB (AASHTO TPXXX)

A comparison of the fracture resistance parameters of the two SCB standards is provided in Figure 2.9. The average fracture energy, G_f using AAHSTO TP105 and the critical strain energy release rate J_c using AAHSTO TPXXX are almost identical at 0.595 and 0.593 $\mathrm{kJ \cdot m^{-2}}$ respectively; an absolute difference of only 0.34%. The TP105 calculated fracture toughness, K_{IC} yields the lowest COV at 13% while G_f is much higher at 26.9%. A COV cannot be assigned to the TPXXX calculated J_c due to the way that J_c is measured; however, the COV of the strain energy to failure, U for the 24, 30, and 36 mm notched specimens are 14.9%, 31.9%, and 38.6% respectively. This expanding COV indicates decreasing repeatability as the available fracture area decreases. The average COV of strain energy to failure. 28.5%, is only slightly larger than the COV of G_f at 26.9%. Overall, the standards present high accuracy (relative to each other) but low precision, high COV, measures of fracture resistance. A large population of specimens is required to arrive at a statistically significant measure of fracture resistance. While TP105 offers a method to calculate K_{IC}, and K_{IC} exhibits a low COV, the use of K_{IC} is not reasonable for most service temperatures (above 10°C of the performance grade lower limit) [41].

The established TP105 test method appears to be the more promising SCB standard when the following advantages are considered.

- The fracture toughness, K_{IC} and energy, G_f are calculated for each specimen and thus less tests are required to produce a statistically significant measure of fracture resistance;
- A single notch depth is required for the fracture toughness K_{IC} and energy G_f calculations.

2.10.5. SCB (AASHTO TP105) versus DCT (ASTM D7313)

A comparison of the fracture energy, G_f calculated using SCB and DCT is provided in Figure 2.9. The SCB approach produced an average G_f of 0.595 $\mathrm{kJ \cdot m^{-2}}$ with a COV of 27% while the DCT approach produced an average G_f of 0.805 $\mathrm{kJ \cdot m^{-2}}$ with a COV of 13.3%. Comparing the load versus displacement curves for each standard (Figure 2.6 and Figure 2.8) it is observed that the peak load experienced in SCB is more than double that of DCT while DCT experienced more than double the elongation of SCB. Examining the tabular value for the work of fracture, W_f (Table 2.2 and Table 2.4), it is observed that the W_f of DCT is 114% larger and carries half the COV of SCB. Possible sources for the large COV of SCB are:

- stress concentrations and plasticity developing at the anvil contact points;
- miss alignment of the specimen, resulting in an otherwise asymmetrical loading setup;

- aggregates (of varying shape and size) along the fracture area acting as obstacles or accelerants to fracture, increasing or decreasing the fracture resistance;

It is hypothesized that the former and later are the primary cause of variation and these variations decrease as the available fracture area increases. Hot mix asphalts are an inherently heterogonous and uncertain material. A rule of thumb for transportation materials is that the coefficient of variation of mechanical properties must be below 15%; however, some researchers have stated up to 25% is acceptable [49]. The ASTM D7313 DCT tests standard defines the COV limit for fracture energy at 15.7%. The two AASHTO standards do not provide any information concerning COV limits. In literature, COVs much larger than 15.7% are routinely reported [49,50]. Composition (particle size, particle properties, air void content, etc.), moisture, and test temperature can have a significant impact on the repeatability of measurements. For the given test conditions, the ASTM D7313 DCT test method is the most reliable approach to measure fracture resistance. The DCT approach exhibits a low COV such that a smaller test matrix can be used to obtain statistically significant fracture resistance measures.

2.10.6. **Digital Image Correlation**

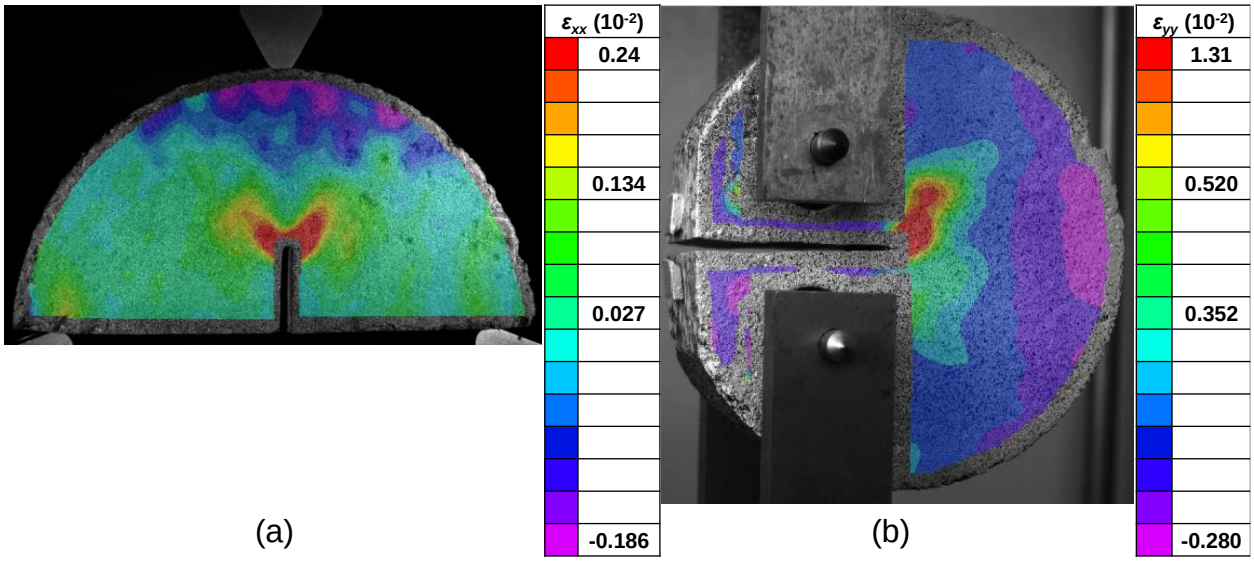

(a) (b)

Figure 2.10. Opening strain of the (a) 24 mm SCB ε_{xx} and (b) 62.5mm DCT ε_{yy} specimens

Three-dimensional DIC was performed on a 24 mm SCB and 62.5mm DCT specimen respectively. Contours of the opening strain are provided in Figure 2.10. The opening strain contours where collected near 80% of the peak load before crack initiation was observed. In both specimen, strain concentrations are observed. Strain concentrations correlate to the presence of stress concentrations. These concentrations indicate the possible crack initiation sites as well as identify the state of tension or compression in the specimen.

For the SCB specimen, strain concentrations are observed at both the notch tip as well as the loading anvil with the magnitude at the notch tip being only 29% larger than that at the loading anvil. This suggests that plasticity could develop at the anvil contact point

during cracking. As the crack propagates, the compressive field at the anvil will interact with the tensile field at the crack tip and negatively impact the work of fracture, W_f in the cracking zone. Due to the size of the SCB specimen, the intensity of the strain concentration is highly dependent on the aggregates near the notch tip and anvil contact point. The strain concentration variation contributes to the high coefficient of variation observed in the calculated fracture energy, G_f .

For the DCT specimen, strain concentrations are observed at the notch tip as well as the back edge of the specimen with the magnitude at the notch tip being 350% larger than that on the back edge of the specimen. The concentration at the notch tip will dominate the cracking response of the specimen. The concentration at the back edge of the specimen is not expected to negatively impact fracture energy calculations.

Overall, it is determined that the SCB specimens are susceptible to a large strain concentration at the anvil contact point.

2.10.7. Three-Dimensional Fracture Area Analysis

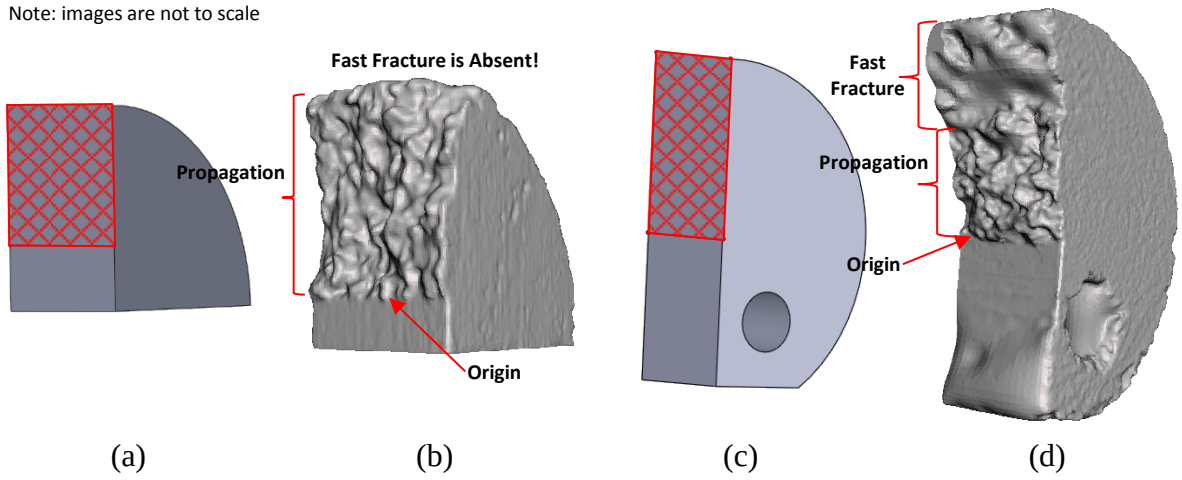

Figure 2.11. Ideal versus actual fracture surface of male (a-b) 24.5 mm SCB and (c-d) 62.5mm DCT specimen

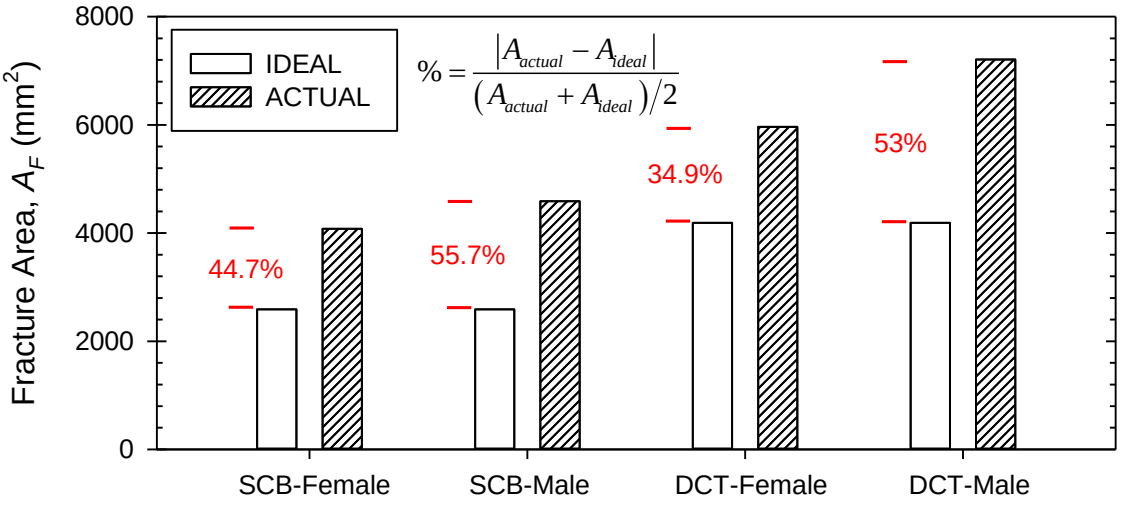

Figure 2.12. Fracture area of SCB and DCT specimen

Three-dimensional scans of a 24mm SCB and 62.5mm DCT specimen were performed. Measurements of both the male and female fracture areas for each specimen were recorded. Only the 24mm SCB specimen was scanned because it represents the best-case scenario with the largest fracture area of the three available SCB specimen notch depths.

A graphical depiction of the ideal versus actual fracture surface of male SCB and DCT specimen are provided in Figure 2.11. The ideal fracture area is considered the area available for fracture if a planar crack is formed along the ligament. The ideal fracture area is equal to the distance from the crack tip to the edge of the specimen multiplied by specimen thickness. For the 24mm SCB and 62.5mm DCT specimen, the ideal fracture area is equal to 2590.8 and 4191 mm^2 respectively such that the ideal fracture area of the DCT specimen is 61.8% larger than the SCB specimen.

The actual fracture area of the SCB and DCT specimen are depicted as 3D scans in Figure 2.11b and d. In both specimen, crack initiation occurs at the notch tip and propagates towards the far edge of the specimen. During propagation, the crack grows through the binder around the heterogeneously disturbed aggregates leading to a rough fracture surface. A fast fracture region is absent in the SCB specimen while for the DCT specimen it is almost equivalent in ligament length to the propagation region. The presence of the fast fracture region is important in fracture testing. The fast fracture region indicates that the fracture energy, G_f or critical strain energy release rate, J_c has truly been exceeded in the specimen and the remaining area available for fracture offers

little resistance to rupture. A lack of the fast fracture region means that plasticity (or general yielding) is the main driving forces behind crack propagation and the specimen continues to offer resistance to fracture up to cleavage.

Slight non-planar cracking is observed in the fast fracture region of the DCT specimen shown in Figure 2.11d. Non-planar cracking is often reported in bituminous mixtures. While the ASTM D7313 for DCT does not mention the limits for non-planar cracking, the European Standard EN 12697-44 for SCB states that a test is valid as long as the crack ends in a zone 10% of the diameter from the center of the load line [52]. This forms a 13° right triangle along the ligament length. For the DCT geometry, this would allow a 19mm crack offset before the test is declared invalid. The definition of the valid zone is necessary to mitigate high COVs. The number of invalid tests increases with nominal aggregate size. A cause of these variations are instances where the notch is cut into large hard aggregate particles. The notch embedded in a particle will alter the overall fracture resistance of the specimen. The DCT specimen depicted in Figure 2.11d is valid.

Measurements of the actual fracture area for male and female pieces are provided in Figure 2.12. Overall, the actual fracture area is much larger than the idea as indicated by the absolute differences in Figure 2.12. The actual fracture area of male and female pieces for both the SCB and DCT specimen are not equal. The difference in fracture area of male and female pieces could be due to different magnitudes of elastic recovery, plastic deformation, and aggregate spallation.

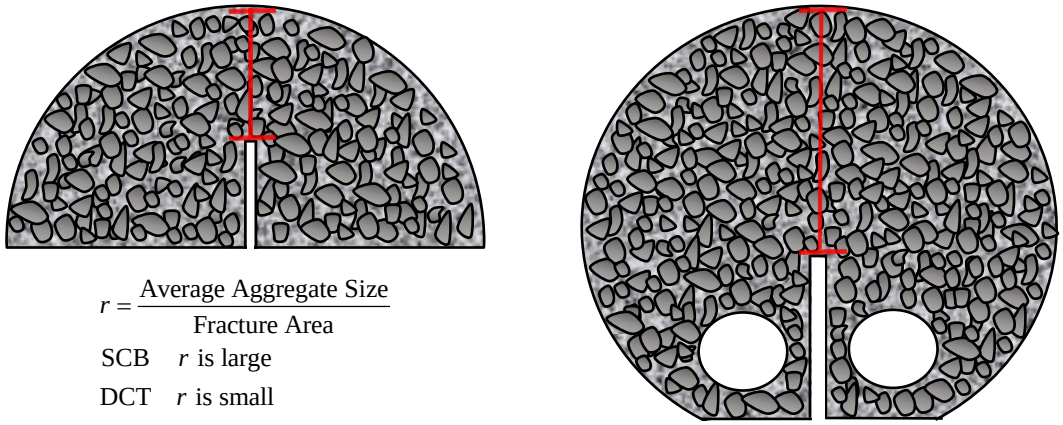

Figure 2.13. Schematic of (a) SCB and (b) DCT specimen with representative aggregates

It is hypothesized that the number and size of individual aggregates can have a significant impact on the average fracture resistance and COV measured in fracture tests. This can be illustrated using a schematic of the SCB and DCT specimen with representative aggregates as shown in Figure 2.13. For SCB specimens as shown in Figure 2.13a, the ratio between the average aggregate size and fracture area is high such that the number of aggregates acting as obstacles to crack propagation is low. For DCT specimens as shown in Figure 2.13b, the ratio between the average aggregate size and the fracture area is low such that the number of aggregates acting as obstacles to crack propagation is high. By lowering the ratio between average aggregate size and fracture area, the influence of individual aggregates is minimized. Essentially, a higher fracture area will improve the average fracture resistance and COV since the fracture

resistance measured will come closer to that of a homogenous representative volume element (RVE). Currently, the fracture area available in the SCB specimen is inadequate. Nondestructive measurement of the average aggregate size of each SCB and DCT specimen followed by fracture testing could provide the preponderance of evidence necessary to prove this hypothesis. For asphaltic materials there are no established specimen size empirical equations for fracture testing similar to those for metallic materials as described in ASTM E399 [53]. An empirical study to determine these equations would increase the scientific rigor of the established testing methods.

2.11. **Conclusions**

During this study, the room temperature fracture resistance of a dense-grade superpave HMA material was evaluated using two SCB test standards and a DCT test standard. A comparative analysis of the statistics of fracture resistance parameters, 3D-DIC strain field at the crack tip, and fracture surface using a 3D scanner was performed to determine the most physically realistic and repeatable test standard. The following can be concluded.

Regarding SCB:

- The SCB fracture energy standard (AASHTO TP105) is found to be superior to the provisional critical strain energy release rate standard (AASHTO TPXXX-15) with the former requiring less specimen and providing a COV for repeatability analysis.

- Overall, the SCB tests produced a low average fracture energy with a high COV when compared to DCT.
- The SCB specimen geometry offers a small fracture area. The work of fracture COV increases as the available fracture area decreases. It is hypothesized that the average aggregate size relative to the available fracture area is not ideal in SCB specimen. The fracture area enlarged if the influence of individual aggregates is to minimized.
- The 3D-DIC strain contours of SCB show that the strain concentration at the crack tip is not dominant and the concentration at the anvil contact points can have a large influence on crack propagation.
- The fractography of SCB does not show a fast fracture region, indicating plasticity (or general yielding) is the dominant mechanism contributing to cleavage.

Regarding DCT:

- The DCT test produces a high average fracture energy with a low COV when compared to SCB.
- The DCT specimen geometry offers a large fracture area such that individual aggregates do not play a significant role in crack propagation.
- The 3D-DIC strain contours of DCT show that the strain concentration at the crack tip is dominant and concentrations at the load points and/or on the back edge do not interfere with crack propagation.

- The fractography of DCT shows a fast fracture region, indicating that the fracture energy or critical strain energy release rate has been reached.

It is concluded that the DCT standard is superior to both SCB standards. Further work is needed fully validate this claim. A larger test matrix including more repeat tests would improve the statistical significance of the fracture resistance measurements. Additional HMA mixtures should be evaluate to determine the extent that average aggregate size influences variability. An analysis of the strain and displacement fields during crack initiation, propagation, and fracture should be performed using 3D-DIC to obtain a clearer picture concerning the onset of fast fracture and the influence of strain concentrations away from the crack tip. In addition, 3D-DIC can be applied to measure a full traction-opening displacement relationship for the ligament and measure the crack advancement towards a length scale parameter to characterize the fracture phenomenon, see e.g. [54]. In-situ volumetric scans using X-ray microtomography could also be conducted to characterize the evolution of the 3D crack during fracture, see e.g. [55].

2.12. **References**

[20] Germann F, Lytton R. Methodology for predicting the reflection cracking life of asphalt concrete overlays. Interim Report, Sep 1974-Mar 1979 1979.

[21] Mechanistic–Empirical Pavement Design Guide: A Manual of Practice, interim edition. Washington, DC: AASHTO; 2008.

[22] Zhou F, Hu S, Scullion T, Mikhail M, Walubita LF. A balanced hma mix design procedure for overlays (with discussion). J Assoc Asph Paving Technol 2007;76:823–50.

[23] Zhou F, Scullion T. Upgraded overlay tester and its application to characterize reflection cracking resistance of asphalt mixtures. College Station, TX: 2003.

[24] Zhou F, Scullion T. Overlay tester: a rapid performance related crack resistance test. College Station, TX: 2005.

[25] Wagoner M, Buttlar W, Paulino G, Blankenship P. Investigation of the fracture resistance of hot-mix asphalt concrete using a disk-shaped compact tension test. Transp Res Rec 2005;1929:183–92. doi:10.3141/1929-22.

[26] Kim M, Mohammad L, Elseifi M. Characterization of fracture properties of asphalt mixtures as measured by semicircular bend test and indirect tension test. J Transp Res Board 2012;2296:115–24. doi:103141/2296-12.

[27] Huang L, Cao K, Zeng M. Evaluation of semicircular bending test for determining tensile strength and stiffness modulus of asphalt mixtures. J Test Eval 2009;37:122–8.

[28] Molenaar A A A, Scarpas A, Liu X, Erkens M J G S. Semi-circular bending test; simple but useful? J Assoc Asph Paving Technol 2002;71:794–815.

[29] Bashin A, Masad E, Kutay ME, Buttlar W, Kim Y-R, Marasteanu M, et al. Applications of advanced models to understand behavior and performance of asphalt mixtures. Transp Res Board 2012:14.

[30] Kim H, Wagoner MP, Buttlar WG. Simulation of fracture behavior in asphalt concrete using a heterogeneous cohesive zone discrete element model. J Mater Civ Eng 2008;20:552–63. doi:10.1061/(ASCE)0899-1561(2008)20:8(552).

[31] Braham A, Buttlar W, Marasteanu M. Effect of binder type, aggregate, and mixture composition on fracture energy of hot-mix asphalt in cold climates. J Transp Res Board 2007;2001:102–9. doi:10.3141/2001-12.

[32] AASHTO. T312-15 Preparing and determining density of hot mix asphalt (hma) specimens by means of the superpave gyratory compactor 2015:1–6.

[33] Mull MA, Stuart K. Fracture resistance characterization of chemically modified crumb rubber asphalt pavement. J Mater Sci 2002;37:557–66.

[34] Saha G, Biligiri KP. Fracture damage evaluation of asphalt mixtures using Semi-Circular Bending test based on fracture energy approach. Eng Fract Mech 2015;142:154–69. doi:10.1016/j.engfracmech.2015.06.009.

[35] Romeo E, Birgisson B, Montepara A, Tebaldi G. The effect of polymer modification on hot mix asphalt fracture at tensile loading conditions. Int J Pavement Eng 2010;11:403–13. doi:10.1080/10298436.2010.488735.

[36] Wu Z, Mohammad L, Wang L, Mull M. Fracture resistance characterization of superpave mixtures using the semi-circular bending test. J ASTM Int 2005;2:1–15. doi:10.1520/JAI12264.

[37] Zhou F, Newcomb D, Gurganus C, Banihashemrad S, Park ES, Sakhaeifar M, Lytton, RL. Experimental design for field validation of laboratory tests to assess cracking resistance of asphalt mixtures. National Cooperative Highway Research Program Transportation Research Board of The National Academies, 2016;No 9-57:1-104.

[38] Wagoner M, Buttlar W, Paulino G, Blankenship P. Investigation of the fracture resistance of hot-mix asphalt concrete using a disk-shaped compact tension test. doi:103141/1929-22 2006.

[39] Roberts FL, Kandhal PS, Brown ER, Lee D-Y, Kennedy TW. Hot mix asphalt materials, mixture design and construction. Lanham, MD: 1991.

[40] Chen X, Huang B. Evaluation of moisture damage in hot mix asphalt using simple performance and superpave indirect tensile tests. Constr Build Mater 2008;22:1950–62. doi:10.1016/j.conbuildmat.2007.07.014.

[41] AASHTO. TP105-13 Standard method of test for determining the fracture energy of asphalt mixtures using the semi circular bend geometry (SCB) 2013:1-14.

[42] AASHTO. TPXXX-15 Provisional standard method of test for determining the fracture energy of asphalt mixtures using the semicircular bend geometry (SCB) at intermediate temperature 2015:1-7.

[43] ASTM. D7313-13 Standard test method for determining fracture energy of asphalt-aggregate mixtures using the disk-shaped compact tension geometry. 2013:1–9. doi:10.1520/D7313.

[44] Rice J, Paris P, Merkle J. Some further results of J-integral analysis and estimates. STP536 Prog. Flaw Growth Fract. Toughness Test., West Conshohocken, PA: ASTM International; 1973, p. 231–45. doi:10.1520/STP49643S.

[45] Begley J, Landes J. The J integral as a fracture criterion. STP514 Fract. Toughness Part II, West Conshohocken, PA: ASTM International; 1972, p. 1–20. doi:10.1520/STP38816S.

[46] RILEM TCS. Determination of the fracture energy of mortar and concrete by means of three-point bend tests on notched beams. Mater Struct 1985;18:285–90. doi:10.1007/BF02472918.

[47] Li X, Marasteanu M. Evaluation of the Low Temperature Fracture Resistance of Asphalt Mixtures using the Semi Circular Bend Test (With Discussion). Assoc Asph Paving Technol 2004;73:401–26.

[48] Li X, Marasteanu M. Investigation of Low Temperature Cracking in Asphalt Mixtures by Acoustic Emission. Road Mater Pavement Des 2006;7:491-512.

[49] Li X, Marasteanu M. Using Semi Circular Bending Test to Evaluate Low Temperature Fracture Resistance for Asphalt Concrete. Exp Mech 2010;50:867-76.

[50] Wagoner, MP, Buttlar, WG, Paulino GH. Disk-Shaped Compact Tension Test for Asphalt Concrete Fracture. Exp Mech 2005:45;270-7.

[51] Landes D, Begley J. The effect of specimen geometry on Jic. STP514 Fract. Toughness Part II, West Conshohocken, PA: ASTM International; 1972, p. 24–9. doi:10.1520/STP38817S.

[52] European Committee for Standardization. Bituminous Mixtures - Test Methods For Hot Mix Asphalt - Part 44: Crack Propagation By Semi-Circular Bending Test. 2010;EN 12697-44.

[53] ASTM. E399-12E3 standard test method for linear-elastic plane-strain fracture toughness Kic of metallic materials. 2013:1–33. doi:10.1520/E0399-09E02.2.

[54] Valoroso N, Sessa S, Lepore M, Cricrì G. Identification of mode-I cohesive parameters for bonded interfaces based on DCB test. Eng Fract Mech 2013;104:56–79. doi:10.1016/j.engfracmech.2013.02.008.

[55] Skarzyński, Nitka M, Tejchman J. Modelling of concrete fracture at aggregate level using FEM and DEM based on X-ray μCT images of internal structure. Eng Fract Mech 2015;147:13–35. doi:10.1016/j.engfracmech.2015.08.010.

3. Effect of Specimen Thickness on the Fracture Resistance of Hot Mix Asphalt in the Disk-Shaped Compact Tension (DCT) Configuration

Calvin M. Stewart, Chinedu W. Oputa, and Eduardo Garcia
Department of Mechanical Engineering
The University of Texas at El Paso
500 West University Avenue
Suite A126
El Paso, TX 79968-0521

Published in the Journal of Construction and Building Materials, Volume 160

3.1. Abstract

In this study, the effect of specimen thickness on the fracture resistance of a dense-graded hot mix asphalt (HMA) is investigated. The fracture toughness, K_c and fracture energy, G_f in triplicate DCT specimens with width-to-thickness ratios ranging from 1.46 to 4.4 is measured at 27°C. The coefficient of variation (COV) of K_c and G_f is calculated to determine reliability as a function of thickness. Photos of cracked specimens and 3D surface scans are employed to study how the crack path and fracture surface changed

with thickness. The ASTM specifications and linear-elastic fracture mechanics theory are applied to show that K_c does not reach a plane-strain condition, $K_c \neq K_{Ic}$, for the given ratios. The average K_c increases with thickness while the COV is inconsistent with thickness. The average G_f is independent of thickness but the COV decreases with thickness; thus, G_f is thickness-dependent. The crack path and fracture surface cannot be used to identify the plane-stress or plane-strain condition due to large aggregates dominating the fracture process. A method for estimating the specimen thickness required for the plane-strain condition and a method to estimate the thickness at which fracture toughness is maximized is demonstrated.

3.2. **Highlights**

- Plane-strain fracture toughness cannot be achieved in 50 mm DCT specimen of dense-graded HMA at 27°C.
- The linear elastic fracture mechanics theory can be applied to determine the optimal layering thickness of HMA where fracture toughness is maximized.
- The fracture surface cannot be applied to determine the plane stress or plane-strain condition of dense-graded HMA at 27°C.

3.3. **Graphical Abstract**

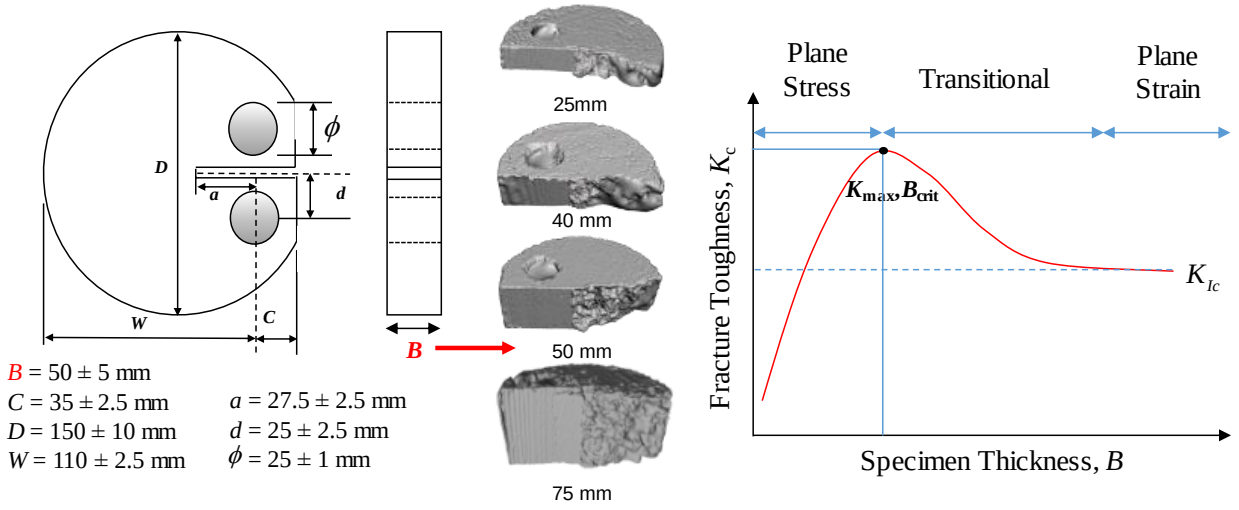

Figure 3.1 – Graphical Abstract

3.4. **Introduction**

Cracking is the most common mode of degradation contributing to failure in flexible pavements. The rapid initiation of cracks shortens the service life of pavement and increases maintenance costs. Hot mix asphalts (HMAs) offer low construction and maintenance costs when compared to concrete yet the problem of cracking persists. There is a need to elucidate the cracking behavior of HMAs to enable proactive maintenance management of transportation infrastructure. HMA layers are subjected to out-of-phase thermo-mechano-chemical fatigue due to the varying types of roads, traffic patterns, and climate across the world. Due to the complex nature of HMA's (an irregular distribution of aggregates in a bitumen matrix) fracture tests exhibit low repeatability. A

systematic investigation into the factors that contribute to this problem is needed. Previous work has shown that specimen geometry plays a key role in repeatability [56]. The current paper investigates specimen thickness as a factor of interest.

Hot mix asphalts are heterogeneous composites consisting of brittle aggregates held within a viscoelastic-plastic bitumen matrix. The aggregates include crushed stone (large), sand (fine), and mineral (filler) at varied sizes and spatial distributions. Fracture is driven by the friction between interlocked aggregates coated with binder that are responsible for the material dilation and nucleation of micro-cracks. The micro-cracks propagate into major cracks due to overload, repeated mechanical loading, thermal cycling, and synergistic effects. At low temperature, the probability of crack initiation is increased due to the quasi-brittle response of the binder and thermal-expansion mismatch with the aggregate as opposed to the ductile response observed at elevated temperature [57,58]. Composition and aggregate gradation play an integral role in the repeatability of fracture tests where large aggregates lead to a high coefficient of variation (COV) in experiments [59].

Several researchers have investigated the fracture resistance of asphalt mixtures [56-73]. The semi-circular bending (SCB) test is a common fracture test for HMAs due to the simplicity of specimen preparation and testing [60]. Saha and Biligiri conducted a review of the state-of-the-art concerning SCB testing of asphalt mixtures [61]. Current standards recommend a specimen thickness of 50 mm [62,63]. Both the fracture toughness, K_c and fracture energy, G_f parameters were evaluated. Fracture toughness, K_c was found

to be independent of thickness between 25 to 75 mm at temperatures below 15°C; however, as temperature increases the magnitude of K_c decreases and the COV increases. Fracture energy, G_f was determined to be dependent on asphalt grade and temperature; however, the effect of thickness was not discussed. In theory, G_f of homogenous linear-elastic materials is insensitive to size; however, since HMAs are heterogeneous viscoelastic-plastic materials this may not hold true. In a follow-on study, Saha and Biligiri [64] evaluated the homothetic fracture resistance behavior of dense grade HMA materials (i.e. the dependence on asphalt content, air voids, temperature, and thickness) using the SCB test. Tests were performed at temperatures of 5 to 25°C with thicknesses from 30 to 50 mm. Increasing the thickness from 30 to 40 mm increased the K_c; however, thicknesses from 40 to 50 mm exhibit no change in K_c. A major advantage of the SCB configuration is the ability to measure the mixed-mode fracture resistance of HMAs [65,66]. Aliha and colleagues performed a series of experiments on the mode I, II, III and mixed cracking of HMAs in the SCB configuration [66-70]. It was determined that SCB is an extremely versatile configuration for examining the mixed-mode cracking observed in transportation materials under multiaxial states of stress.

Specimen geometry plays a key role in the average K_c and COV. The Texas A&M Transportation Institute evaluated the performance of several fracture test configurations including the disk-shaped compact tension (DCT), semi-circular bending (SCB), indirect tension (IDT), thermal stress-restrained specimen test or uniaxial thermal stress and

strain test (TRSST/UTSST), texas overlay (Texas OT), bend beam fatigue (BBFT), simplified viscoelastic continuum damage (S-VCD), and the repeated direct tension (DT) test [71]. The tests were compared with regards to test complexity, correlation to field performance, test variability, test sensitive to mix design parameters, and cost. The DCT, SCB, and Texas OT were found to have the lowest cost and exhibit good correlation to field performance; however, DCT was observed to produce the lowest COV. To further examine these conclusions, Stewart et al. [56] performed a comparative analysis of the SCB and DCT mode I fracture energy test standards on a dense-graded Superpave HMA. The SCB and DCT tests were conducted according to AASHTO TP105-13 and ASTM D7313-13 at the thickness of 50 mm (recommended in ASTM D7313) and a temperature of 27°C [62,63]. The SCB tests produced a low G_f with a high COV when compared to DCT. The DCT geometry offers more fracture area for cracking propagation making it a more repeatable test.

Wagoner et al. [72] performed DCT fracture energy tests on four asphalt mixtures ranging from typical Illinois to polymer-modified interlayer mixtures. For a single mixture at -10°C, the thickness was profiled from 25 to 75 mm. Fracture energy, G_f was found to increase with thickness while the COV also increased from 13 to 19%. Kim et al. [73] found that increasing the diameter of a specimen from 100 to 450 mm led to an increase in G_f while the COV remained relatively constant near 15%.

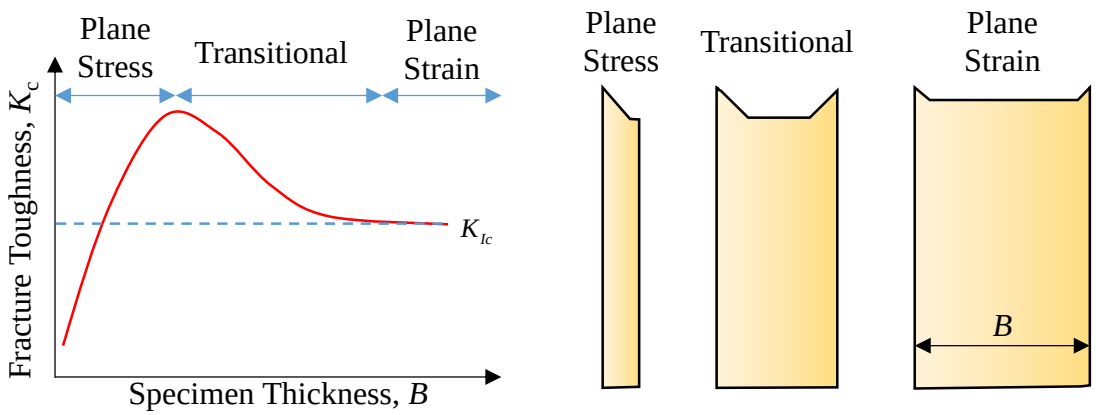

Figure 3.2 - Fracture toughness and fracture surface versus thickness in homogeneous linear-elastic materials

According to linear-elastic fracture mechanics (LEFM) theory, the fracture toughness of a homogeneous material is thickness dependent up to the plane-strain condition where the value becomes a constant material property [74-76]. The size or thickness dependence is associated with the transition from plane-stress to plane strain as illustrated in Figure 3.2. The fracture toughness, K_c is called the “apparent” fracture toughness when it is thickness-dependent and is called the “plane-strain” fracture toughness, K_{Ic} when it becomes an intrinsic material property that is not thickness-dependent. In plane-stress, the direction of maximum shear stress is in the anti-plane direction (±45°) leading to the formation of a slant crack or shear lips. Under plane-stress, microstructural defects play a significant role in fracture toughness resulting in a high COV. As thickness increases, the specimen transitions from plane-stress to a plane-strain condition. In plane-strain, the direction of the maximum shear stress is in-

plane leading to a flat fracture surface. The field of defects in the material homogenize such that the fracture toughness resolves to a horizontal asymptote with a low COV. By reviewing LEFM theory, it can be concluded that

- the plane-strain fracture toughness, K_{Ic} is a conservative measure of fracture resistance.
- for design it would be advantageous to determine the thickness where the apparent fracture toughness, K_c is maximized and the COV is reasonable [74-76].

Since HMAs are heterogeneous composites, and the theory described above may not hold true, there is a need to investigate the thickness-dependence of the fracture resistance of HMAs.

It is important to check the ASTM requirements for the plane-strain condition. ASTM developed two standards to support the measurement of the K_{Ic} in metallic and homogenous materials: ASTM E399-12e3 [77] and ASTM E1820-16 [78], respectively. A key requirement of these two standards is that the width-to-thickness ratio, W/B, shall remain between 2 and 4. The standard ratio is $W/B = 2$. Another requirement is that the following inequality be enforced

(1) $$a, B \geq 2.5\left(\frac{K_{Ic}}{\sigma_{YS}}\right)^2$$

where K_{Ic} is the approximate plane-strain fracture toughness, σ_{YS} is the yield strength, a is the crack length, and B is the thickness. The fracture toughness cannot be considered plane-strain, K_{Ic}, when this condition is violated, and it must be defined as the apparent fracture toughness, K_c, reported everywhere with respect to thickness [61].

In this study, the effect of specimen thickness on the K_c and G_f of a dense-graded HMA is investigated using DCT specimens at a temperature of 27°C. The DCT configuration was selected due to the availability of an ASTM test standard [62] and the low COV expected in this configuration [56,71]. The tests are performed at width-to-thickness ratios ranging from 1.46 to 4.4. Statistical analysis is performed to investigate how K_c and G_f evolve as a function of thickness. Photos of cracked specimens and 3D surface scans are employed to determine how the crack path and fracture surface change with thickness.

3.5. Material And Test Methods

3.5.1. Hot Mix Asphalt

The material in this study is a dense-graded HMA (designated as Type-C by Texas Department of Transportation) used in West Texas. The properties of the mix are summarized in Table 3.1. The gradation is listed in Table 3.2. The relevant aggregates and binder were sampled and transported to the Center for Transportation Infrastructure Systems at The University of Texas at El Paso (UTEP) where specimens were prepared and tested.

Table 3.1 - Summary of HMA properties

NMAS (mm)	19
Asphalt Performance Grade	PG 70-22
Binder Substitution	PG 64-22
Optimal Asphalt Content (%)	4.6
Specific Gravity	1.001
Binder Percent (%)	4.6
VMA (%) at optimum AC	15.2

Table 3.2 - Gradation chart of Type-C mix

Sieve Size	**Percentage**
1''	100.0
3/4"	99.3
3/8"	82.4
No.4	52.7
No. 8	36.9
No. 30	18.6
No. 50	14.0
No. 200	5.6

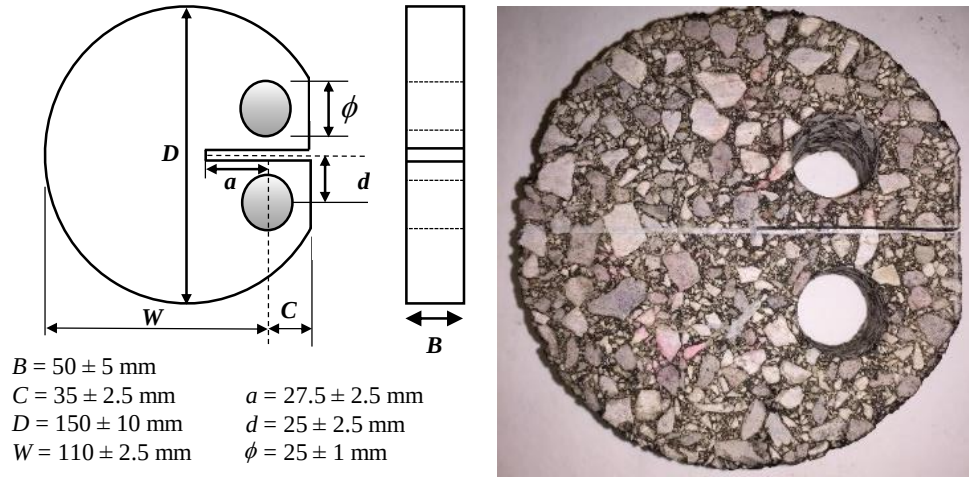

(a) (b)

Figure 3.3 – Disk-shaped compact tension (a) dimensions and (b) specimen

3.5.2. **Specimen Preparation**

The HMA mixture is heated to 132 ± 3º C to liquefy the binder and improve mold-ability. Standard 150 mm diameter by 114 mm thick briquettes are compacted with a superpave gyratory compactor according to AASHTO T312-15 and ASTM D6925-15 [79,80]. After the briquette reaches room temperature, a disk shape specimen is excised from the middle using a masonry saw to the desired thickness. The disk is quality checked for an air-void percentage (AV%) target of 7±1.0%. Disks with the proper AV% are machined into DCT specimen according to ATSM D7313-13 [62]. One DCT specimen can be extracted from each disk with the dimensions illustrated in Figure 3.3. Specimen were prepared with thicknesses of 25, 40, 50, and 75 mm. The width-to-thickness range is $1.46 \leq W/B \leq 4.4$.

3.5.3. **Mechanical Test Equipment**

The mechanical tests were conducted using an INSTRON 5969 Table-Top Universal Test System. The test frame is equipped with an Instron 3119-609 Environmental Chamber capable of regulating temperature from -100 to +350°C. Load and displacement limits were set for the load cell, crosshead displacement, and extensometers to avoid equipment damage. The specimens were set to an isothermal temperature of 27°C for the duration of each test. The data captured during each test includes time, load, and line displacement.

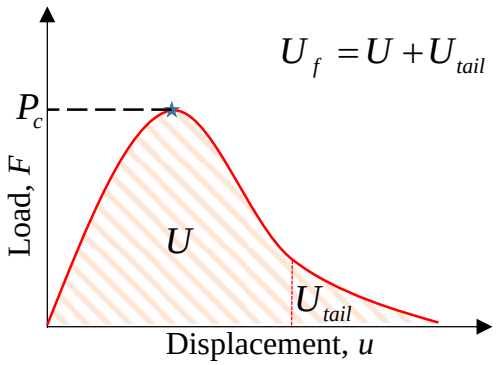

Figure 3.4 – Load versus load-line displacement [56]

3.5.4. DCT Fracture Toughness (Modified from ASTM E1820-16)

Fracture toughness tests are performed according to ASTM E1820-16 the "Standard Test Method for Measurement of Fracture Toughness" [78]. In Appendix A3, the standard provides a procedure for calculating the fracture toughness, K_c ($\mathrm{MPa} \cdot \mathrm{m}^{0.5}$) of DCT specimens. The fracture toughness K_c is defined as the stress intensity factor, K_i corresponding to the initiation of a crack in a homogenous, linear-elastic body. Fracture toughness, K_c, is typically measured at the peak load, P_c depicted in Figure 3.4 [56]. For the DCT geometry, the stress intensity factor, K_i is computed as follows

(1) $$K_i = \frac{P_i}{(BB_N W)^{1/2}} f(a_i / W)$$

where i is the data point, P_i is the load at the ith data point (N), W is the width (mm), f is the dimensionless geometry factor, a_i is the crack length at the ith data point (mm), B_N is the net thickness (mm), and $B = B_N$ if no side grooves are present.

The dimensionless geometry factor, f for the DCT geometry is calculated as

$$f(a_i/W) = \frac{\{(2-a_i/W)[(0.76+4.8(a_i/W)-11.58(a_i/W)^2 + 11.43(a_i/W)^3 - 4.08(a_i/W)^4]\}}{(1+a_i/W)^{3/2}} \quad (2)$$

The plane-strain fracture toughness, K_{Ic} is obtained by profiling the apparent fracture toughness, K_c as a function of thickness and finding the horizontal asymptote where $K_c = K_{Ic}$ is insensitive to thickness.

Before testing, the specimens were fatigue pre-cracked until the notch grew by $\Delta a > 0.2B$ beyond the initial notch length. The maximum stress intensity factor, $K_{\max}$ during pre-cracking did not exceed 60% of the estimated plane-strain fracture toughness K_{Ic}.

3.5.5. DCT Fracture Energy (According to ASTM D7313-13)

Fracture energy tests are performed according to ASTM D7313-13 the “Standard for determining the fracture energy of asphalt-aggregate mixtures” [62]. The standard calculates the fracture energy, G_f using a single-specimen solution. Tests are performed with a constant crack mouth opening displacement, CMOD of 0.017 mm/s.

The standard does not call for pre-cracking so it was not preformed. The fracture energy, G_f is calculated as follows

(3) $$G_f = \frac{U_f}{B \cdot (W - a)}$$

where U_f is the work of fracture (J), *B* is the thickness (mm), and $(W - a)$ is the initial ligament length (mm). The work of fracture, U_f is calculated as the area under the load-CMOD curve depicted in Figure 3.4 using the quadrangle rule as follows

(4) $$U_f = \sum_{i=1}^{n} (u_{i+1} - u_i) \cdot (P_i) + 0.5 \cdot (u_{i+1} - u_i) \cdot (P_{i+1} - P_i)$$

where *n* is the number of data points, *u* is the CMOD, and *P* is the load.

3.5.6. **3D Surface Scanning**

The fractured specimens are 3D scanned to produce a 3D CAD replication of the fracture surface using a MakerBot Digitizer 3D Scanner. The scanner has a nominal dimensional accuracy of ±2 mm and detail resolution of 0.5 mm. The device uses two lasers and a rotating platform to generate a 3D dimensional replication of the surface of 3D objects. The Makerware software, exports a stereo lithography format file (.STL). The AutoDesk MeshMixer software is employed to analyze the physical features of the 3-D .STL files.

3.6. Results And Discussion

3.6.1. ASTM Requirements

Preliminary experiments were performed to check the ASTM plane-strain condition [Eq. (1)]. The AASHTO TP 105, ASTM E399, and ASTM E1820 standards recommend at least triplicate tests for each material condition [63,77,78]. Three indirect tensile tests (IDT) were performed recording an average yield strength, σ_{YS} of 849 kPa. Three DCT tests were performed at a specimen thickness of 50 mm measuring an average fracture toughness of 0.265 $\mathrm{MPa}\sqrt{\mathrm{m}}$. Taking these properties and evaluating [Eq. (1)], it is estimated that a specimen thickness of 244 mm or greater is required to achieve the plane-strain condition. To maintain a width-to-thickness ratio within the recommended range of $2 \le W/B \le 4$; the specimen width must be between $488\ \mathrm{mm} \le W \le 976\ \mathrm{mm}$. A specimen with the above dimensions is not practical to test and exceeds the typical thickness of laid HMA. In summary, for dense-graded HMA at 27°C, the fracture toughness measured using the standard DCT dimensions is the “apparent” fracture toughness, K_c and must be reported with specimen thickness.

Table 3.3 – Fracture toughness of dense-graded HMA

Specimen Name*	Thickness, B (mm)	Air Voids, AV (%)	Critical Crack Length, a_c (mm)	Peak Load, P_c (N)	Apparent Fracture Toughness, K_c ($MPa\sqrt{m}$)	Apparent Fracture Toughness, K_c Avg.($MPa\sqrt{m}$)	Apparent Fracture Toughness, K_c Std. Dev.($MPa\sqrt{m}$)	Apparent Fracture Toughness, K_c COV(%)
K25-1	265	6.9	37.1	236.5	0.171	0.197	±0.035	17.5
K25-2	27.0	6.3	43.0	223.6	0.184	0.197	±0.035	17.5
K25-3	25.1	6.4	54.5	190.4	0.236	0.197	±0.035	17.5
K40-1	41.4	7.1	39.2	463.7	0.228	0.235	±0.014	6.0
K40-2	39.9	7.1	44.0	377.7	0.227	0.235	±0.014	6.0
K40-3	41.2	7.1	54.9	332.5	0.252	0.235	±0.014	6.0
K50-1	50.4	6.8	38.5	678.3	0.277	0.265	±0.029	11.1
K50-2	57.8	6.3	40.3	645.5	0.232	0.265	±0.029	11.1
K50-3	48.9	7.5	47.8	548.4	0.288	0.265	±0.029	11.1
K75-1	73.2	7.3	47.8	695.8	0.248	0.289	±0.035	12.2
K75-2	73.4	6.6	59.2	625.3	0.307	0.289	±0.035	12.2
K75-3	73.6	6.8	71.1	393.7	0.311	0.289	±0.035	12.2

*KXX-Y: K-fracture toughness test, XX- specimen thickness in mm, Y- test number at XX

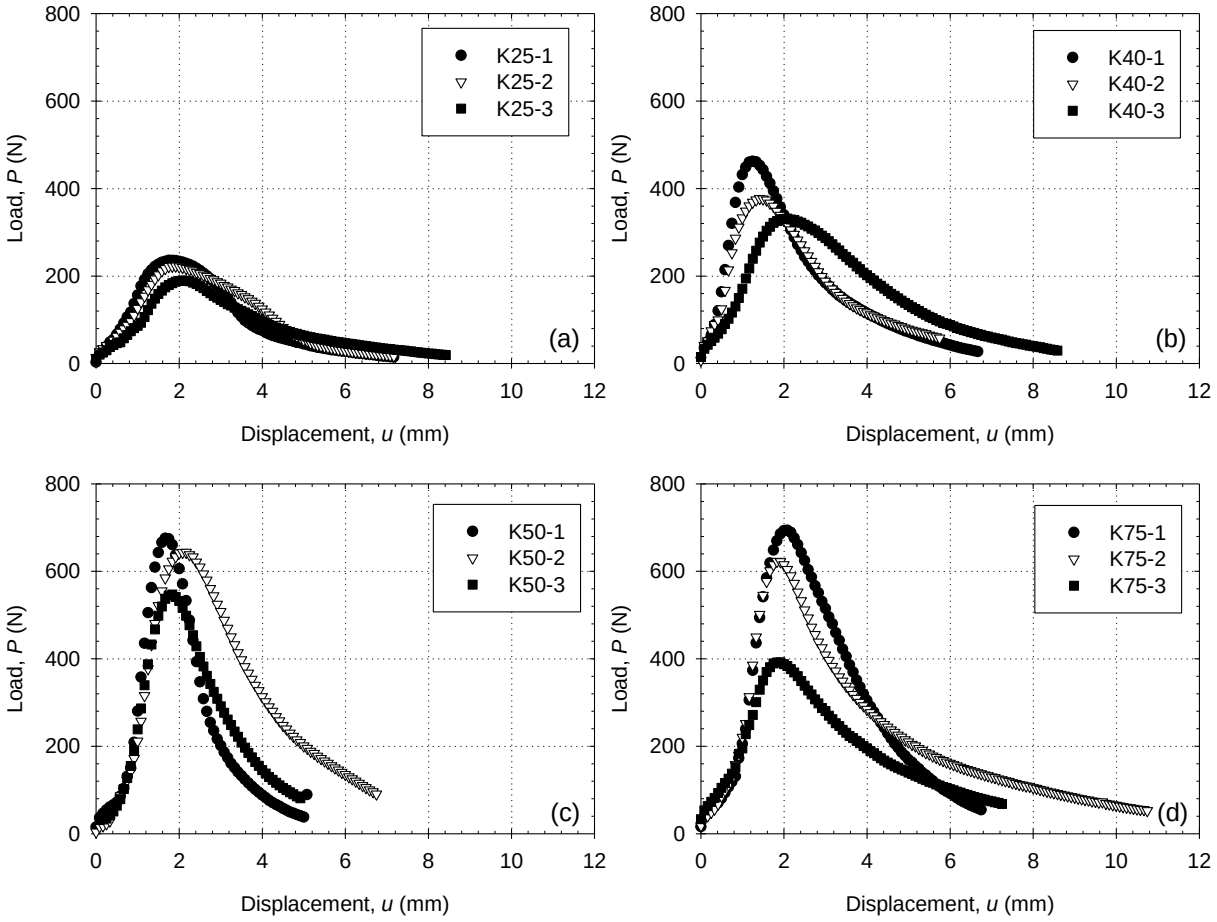

Figure 3.5 – Load-displacement of fracture toughness tests at thicknesses (a) 25 to (d) 75 mm

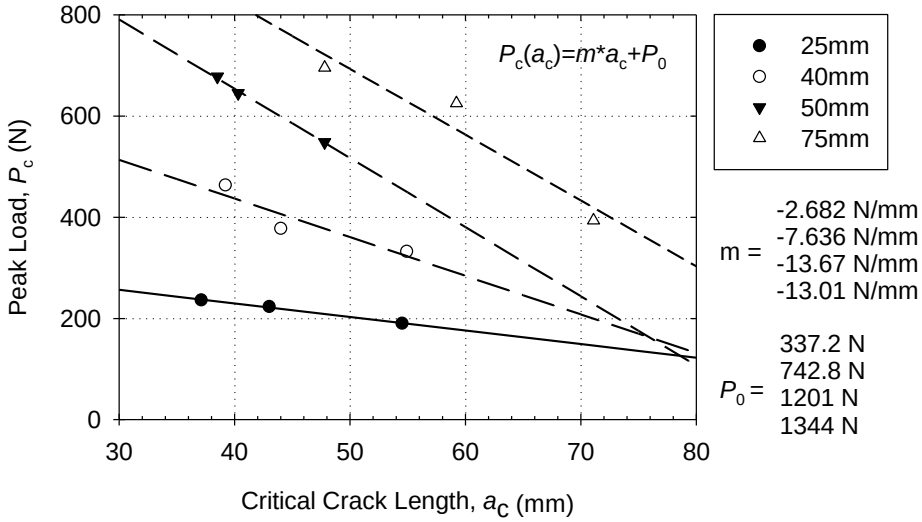

Figure 3.6 – Peak load versus critical crack length

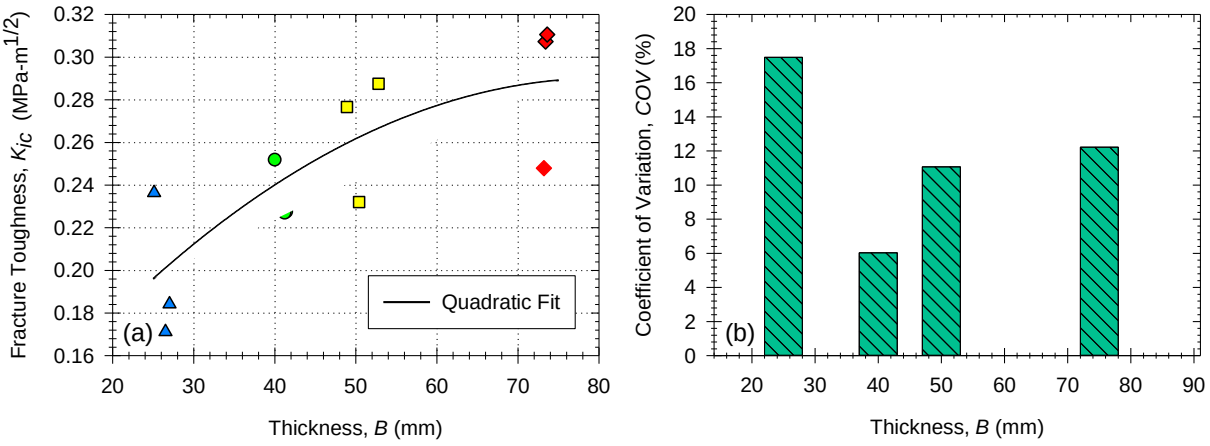

Figure 3.7 – Fracture toughness versus thickness: (a) magnitude and (b) coefficient of variation

3.6.2. **Fracture Toughness**

Fracture toughness tests were performed on triplicate specimens prepared at four thicknesses. The test results are presented in Table 3.3 with the load-displacement curves shown in Figure 3.5. On average, the peak load increases with thickness. At a given thickness, the peak load varies. The peak load variation is linked to the different initial notch length measured for each specimen after pre-cracking. The critical crack length was optically measured (at the instant of fracture) using a three-dimensional digital image corellation (3D-DIC) system. The 3D-DIC system consists of a set of cameras that capture images of the surface of the specimen. These images are syronchronized with load cell data and the image correspond to the peak load is used to measure the critical crack length. The critical crack length is plotted with respect to peak load in Figure 3.6. Peak load versus critical crack length exhibits a linear relationship with a negative-slope. As the critical crack length increases the peak load decreases. The trend follows LEFM theory where when the fracture area decreases the force needed for fracture decreases. The dimensions, peak load, and critical crack length are applied to calculate the fracture toughness, K_c. Fracture toughness is plotted against thickness in Figure 3.7a. When compared to the LEFM theory in Figure 3.2, the HMA is under plane-stress at the given thicknesses. Theory states there exists a maximum fracture toughness in the transition from plane-stress to plane-strain. A quadratic function is fitted to the fracture toughness versus thickness data as follows $K_c(B) = -2.547\text{E-}05 \cdot B^2 + 4.485\text{E-}03 \cdot B + 9.807\text{E-}02$. Taking the derivative of the function

and setting it equal to zero, the maximum fracture toughness is approximately 0.295 $\mathrm{MPa}\sqrt{\mathrm{m}}$ at a thickness of 88 mm. It is important to note that the thickness where fracture toughness is maximized is specific to the cracking mode (mode I), composition (dense-grade HMA used in West Texas), temperature, and geometry (DCT). The COV of K_c is plotted versus thickness in Figure 3.7b. The COV is of acceptable magnitude for HMAs (below 15% acceptable, below 5% excellent) but is inconsistent at the given thicknesses with an unexplained drop at 40 mm. A high COV is expected in plane-stress since microstructural features become dominant at small thicknesses, particularly in heterogeneous materials.

In summary, for dense-graded HMA at 27°C, K_c depends on specimen thickness between 25 and 75 mm. It is estimated that the specimen is under plane-stress at $B \leq 88\ \mathrm{mm}$ and plane-strain at $B \geq 244\ \mathrm{mm}$. These findings are dependent on composition, temperature, and specimen. Different HMA compositions and gradations will have different mechanical properties. The deformation and fracture mechanisms of HMAs change with temperature. Specimen that offer large fracture areas will produce lower COVs. The mode I DCT configuration does not reflect the actual multiaxial state of stress induced in the surface of flexible pavement layers during traffic loads; however, it is a useful configuration to consistently evaluate the basic fracture resistance of these materials. If a fracture toughness test can be configured to perfectly replicate the cracking mode, composition, temperature, and geometry of flexible pavement layers in-service, a design engineer can apply the LEFM theory demonstrated here to maximize

the fracture resistance of flexible pavement layers by deriving the optimal thickness. The COV must be involved in the design process such that the decision is based not only on performance but reliability.

Table 3.4 – Fracture Energy of Dense-Graded HMA

Specimen Name*	Thickness, B (mm)	Air Voids, AV (%)	Ligament Length, $W-a$ (mm)	Work of Fracture, U_f (J)	Fracture Energy, G_f (J·m^{-2})	Avg Fracture Energy, G_f (J·m^{-2})	Std. Dev of Fracture Energy, G_f (J·m^{-2})	COV of Fracture Energy, G_f (%)
G25-1	26.9	6.8	83.9	1.265	560.7	714.7	±167.1	23.38
G25-2	27.1	6.1	77.8	1.457	691.2	714.7	±167.1	23.38
G25-3	25.2	6.3	81.6	1.835	892.4	714.7	±167.1	23.38
G40-1	41.5	7.5	81.3	2.634	780.6	718.2	±70.32	9.791
G40-2	41.8	7.0	79.8	2.141	642.0	718.2	±70.32	9.791
G40-3	42.3	7.3	82.5	2.555	732.0	718.2	±70.32	9.791
G50-1	53.1	6.4	82.3	2.915	667.2	645.6	±19.98	3.095
G50-2	53.0	6.9	79.4	2.700	641.8	645.6	±19.98	3.095
G50-3	54.7	6.8	82.4	2.830	627.8	645.6	±19.98	3.095
G75-1	74.7	7.5	81.5	4.153	682.1	700.8	±23.44	3.345
G75-2	75.0	7.5	80.5	4.186	693.1	700.8	±23.44	3.345
G75-3	76.0	7.9	82.3	4.548	727.1	700.8	±23.44	3.345

*GXX-Y: G-fracture energy test, XX- specimen thickness in mm, Y- test number at XX

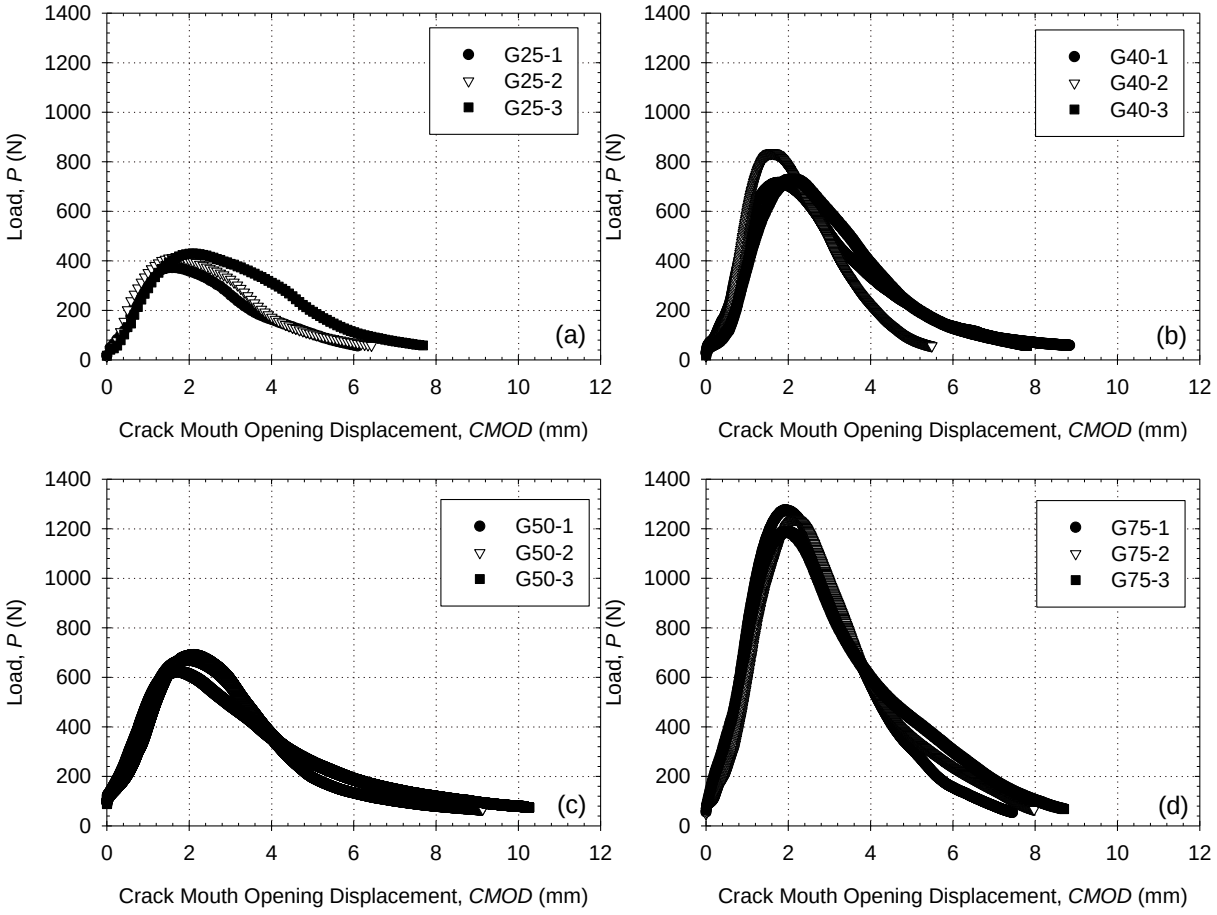

Figure 3.8 – Load-CMOD curves of fracture energy tests at thicknesses (a) 25 to (d) 75 mm

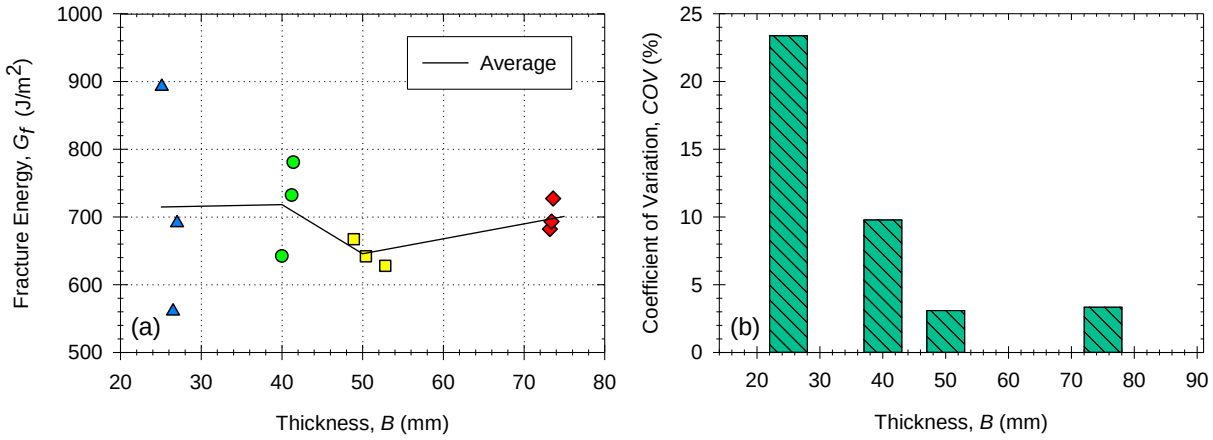

Figure 3.9 – Fracture energy versus thickness: (a) magnitude and (b) coefficient of variation

3.6.3. **Fracture Energy**

Fracture energy tests were performed on triplicate specimens at four different thicknesses. The test results are presented in Table 3.4 with the load-displacement curves shown in Figure 3.8. The fracture energy load-displacement curves have a tight grouping when compared to the fracture toughness tests in Figure 3.5. At a given thickness, the peak load remains relatively constant. This trend relates to the absence of pre-cracking. On average, the peak load and work of fracture increase with thickness. The initial dimensions and work of fracture are applied to calculate the fracture energy, G_f. Fracture energy and the COV is plotted against thickness in Figure 3.9a and b respectively. On average, fracture energy remains approximately $700\ \mathrm{J/m^2}$ at thicknesses between 25 to 75 mm; however, this statistic is misleading when the COV is

considered. The COV of G_f is thickness-dependent and decreases as the thickness increases from 23.4% at 25 mm to 3.3% at 75 mm. Statistically, the likelihood of achieving a consistent fracture energy in replicate tests decreases as thickness decreases. Thus, fracture energy is thickness dependent. The standard 50 mm thickness (recommended by ASTM D7313-13) is sufficient to obtain consistent fracture energy measurements at a COV of 3.1%.

In summary, for dense-graded HMA at 27°C, the COV of G_f is dependent on specimen thickness between 25 and 50 mm. At thickness >50 mm, the COV of G_f becomes independent of thickness. Similar to fracture toughness, these findings are dependent on material, temperature, and specimen. For example, Wagoner et al. [72] found specimen size has a significant impact on the fracture energy of an HMA at -10°C. Overall, the fracture toughness and energy of a given HMA mixture must be evaluated experimentally at the expected service conditions (layer thicknesses, temperature range, strain rates) before any conclusions concerning the dependencies of a given mixture can be made.

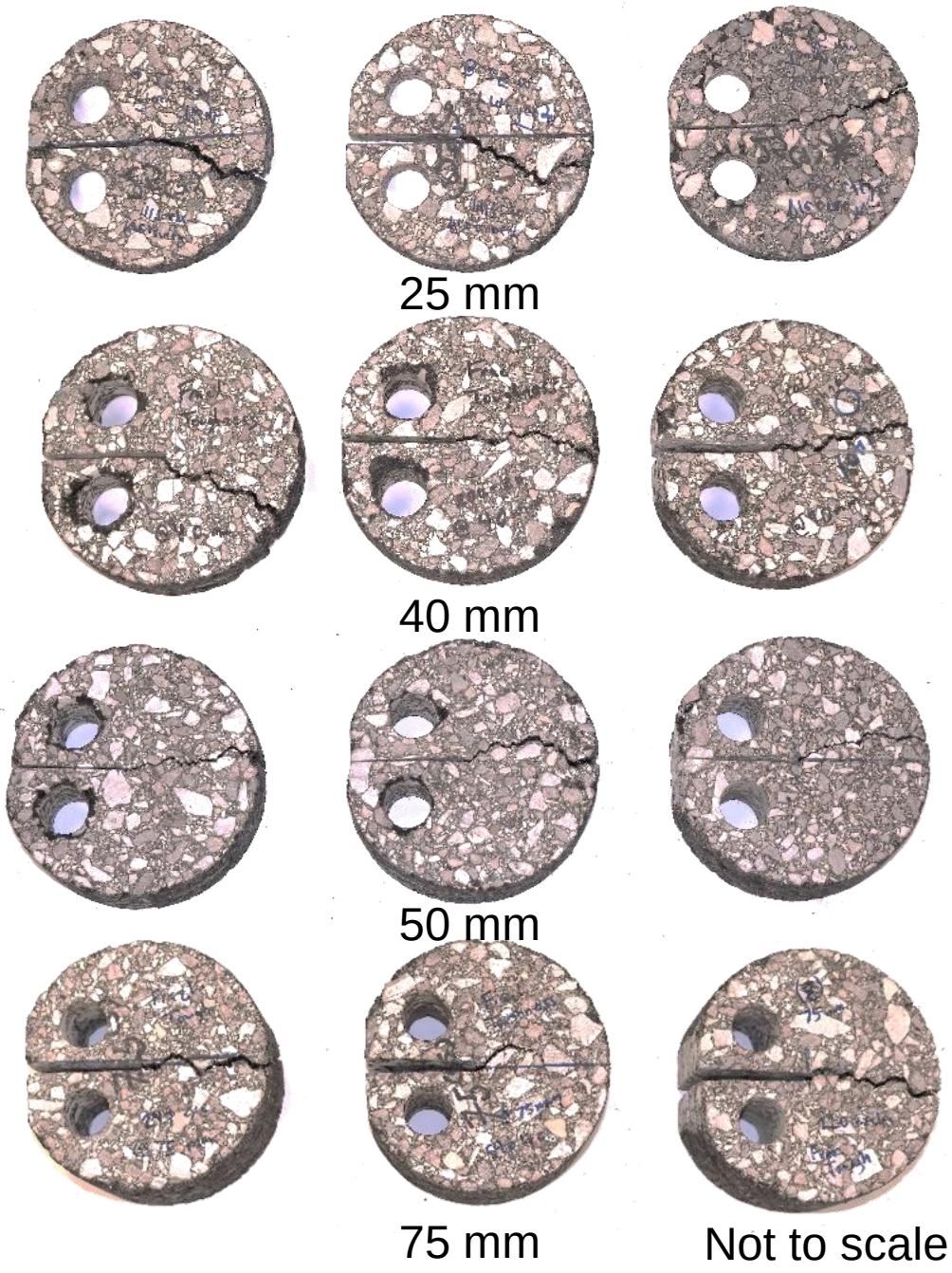

Figure 3.10 – Crack Path observed in K_c specimen

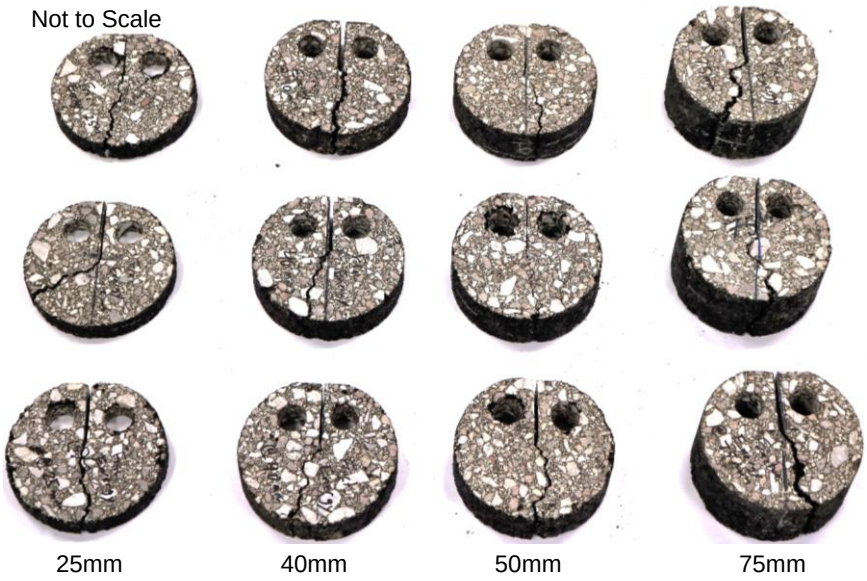

Figure 3.11 – Crack Path observed in G_f specimen

3.6.4. **Crack Path**

Photographs of the crack path for each K_c and G_f specimen are presented in Figure 3.10 and Figure 3.11, respectively. In both tests and at all thicknesses, the primary crack propagates through the bitumen bypassing most large aggregates. From specimen-to-specimen, the crack is torturous and travels uniquely through the heteregenous structure following a path of least resistance. The crack path is perturbed by obstacles (such as large well-bonded aggregates) and weak zones (voids, weakly-bonded interfaces, etc.). In limited cases, the crack bisects moderately sized aggregates. These failed aggregates are primarly found at long cracks near the points where the specimen seperated in half. In summary, for dense-graded HMA at 27°C, there is no trend between crack path and thickness.

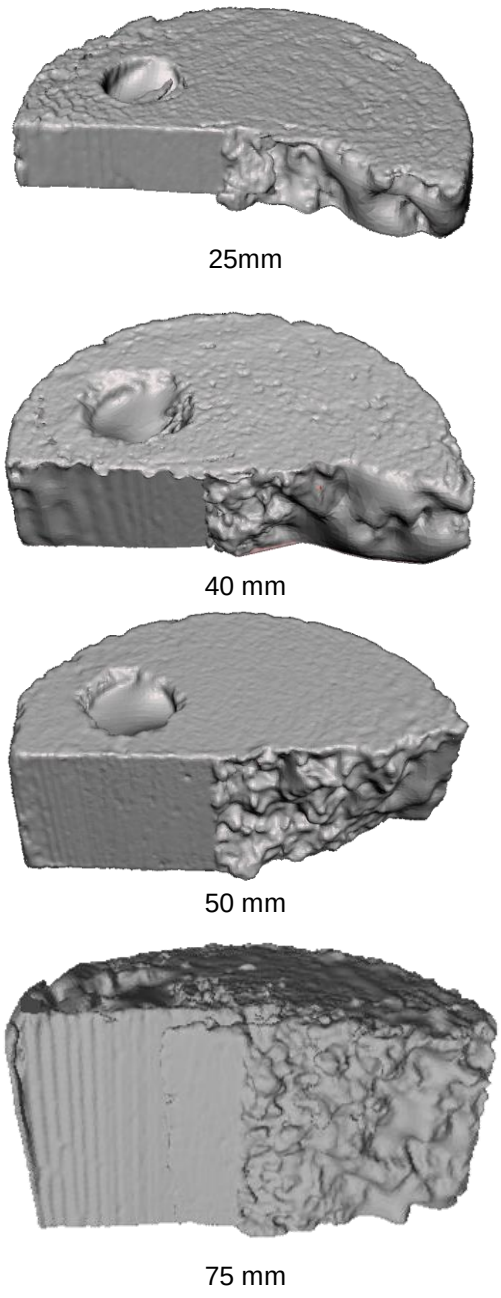

Note: Not to scale

Figure 3.12 – 3D Fracture Surface at specimen thicknesses from 25 to 75 mm

3.6.5. **3D Surface Scanning**

In homogeneous linear-elastic materials, the fracture surface should evolve with thickness as illustrated in Figure 3.2. Under plane-stress, a slant crack should be observed. In the transition from plane-stress to plane-strain a mixed-mode fracture surface, including both shear lips and a flat surface, should be observed. In plane-strain, the fracture surface should be flat with minimal shear lips.

3D surface scans taken of G_f specimens at different thicknesses are shown in Figure 3.12. The trends for homogenous linear-elastic materials do not hold for dense-graded HMA. It was previously determined that dense-graded HMA is in plane stress when $B \leq 88 \text{ mm}$ and plane-strain when $B \geq 244 \text{ mm}$. Examining the 3D scans, the fracture surfaces at all thicknesses are non-planar and reside between 0 and 45°. The crack bypasses aggregates leading to a tortuous and cratered fracture surface. It is possible that the crack may become more planar as the specimen approaches plane-strain, $B \geq 244 \text{ mm}$; however, the gradation chart for the dense-graded mix used (Table 3.2) suggests the fracture surface can remain out-of-plane by up to 19 mm (the largest aggregates size). In summary, for dense-graded HMA at 27°C, 3D scans of the fracture surface cannot reasonable predict the plane-stress or plane-strain condition.

3.7. **Conclusions**

The goal of this effort was to evaluate the effect of thickness on the fracture resistance of HMA mixtures in the DCT configuration. For dense-grade HMA tested at 27°C, it is determined that

- checking the requirements of ASTM E399-12 and E1820-16, [Eq. (1)], the specimens are in plane-stress when $B \leq 88 \text{ mm}$ and plane-strain when $B \geq 244 \text{ mm}$.
- the fracture toughness is maximized at $B = 88 \text{ mm}$.
- the K_c is thickness dependent at all thicknesses tested in this study. The COV of K_c is inconsistent but acceptable (less than 15%) at $B \geq 40 \text{ mm}$.
- the COV of G_f is thickness dependent from 25 to 50 mm and becomes insensitive at $B \geq 50 \text{ mm}$. The standard 50 mm thick specimen is adequate when performing G_f test.
- there is no trend between crack path and thickness. 3D surface scans do not provide enough evidence to determine the plane-stress or plane-strain condition.

This study examined the effect of thickness on fracture toughness at one HMA composition and temperature in the DCT configuration. As the properties of HMA are highly dependent on composition, temperature, and geometry the outcomes of the research are limited to understanding the fracture characteristics of this specific mixture; however, the techniques applied to identify plane-stress versus the plane-strain

condition and the approach of maximizing the fracture toughness by altering the dimensions can be applied to any HMA mixture towards improving the design and performance of flexible pavement layers. In future work, fracture resistance tests will be performed under service-like conditions including the cracking mode, strain rate, temperature, and geometry. Thermo-mechano-chemical fatigue tests will be designed to simulate (in an accelerated manner) the degradation of HMAs.

3.8. References

[56] C.M. Stewart, J.G. Reyes, V.M. Garcia, Comparison of fracture test standards for a super pave dense-graded hot mix asphalt, Eng. Fract. Mech. 169 (2017) 262–275. doi:10.1016/j.engfracmech.2016.10.016.

[57] K.W. Kim, M. El Hussein, Variation of fracture toughness of asphalt concrete under low temperatures, Constr. Build. Mater. 11 (1997) 403–411. doi:10.1016/S0950-0618(97)00030-5.

[58] E. Zegeye, J.-L. Le, M. Turos, M. Marasteanu, Investigation of size effect in asphalt mixture fracture testing at low temperature, Road Mater. Pavement Des. 13 (2012) 88–101. doi:10.1080/14680629.2012.657064.

[59] X. Li, M. Marasteanu, The fracture process zone in asphalt mixture at low temperature, Eng. Fract. Mech. 77 (2010) 1175–1190. doi:10.1016/j.engfracmech.2010.02.018.

[60] A. A. A. Molenaar, A. Scarpas, X. Liu, S. Erkens, Semi-Circular Bending Test; Simple But Useful?, J. Assoc. Asph. Paving Technol. 71 (2002) 794–815.

[61] S. Gourab, K.P. Biligiri, Fracture properties of asphalt mixtures using semi-circular bending test : A state-of-the-art review and future research, Constr. Build. Mater. 105 (2016) 103–112. doi:10.1016/j.conbuildmat.2015.12.046.

[62] ASTM D7313-13, Standard test method for determining fracture energy of asphalt-aggregate mixtures using the disk-shaped compact tension geometry, ASTM International, West Conshohocken, PA, 2013, www.astm.org, doi:10.1520/D7313.

[63] AASHTO TP105-13, Standard method of test for determining the fracture energy of asphalt mixtures using the semi circular bend geometry, AAHSTO, Washington, DC, 2013.

[64] G. Saha, K.P. Biligiri, Homothetic behaviour investigation on fracture toughness of asphalt mixtures using semicircular bending test, Constr. Build. Mater. 114 (2016) 423–433. doi:10.1016/j.conbuildmat.2016.03.169.

[65] S. Im, H. Ban, Y.R. Kim, Characterization of mode-I and mode-II fracture properties of fine aggregate matrix using a semicircular specimen geometry, Constr. Build. Mater. 52 (2014) 413–421. doi:10.1016/j.conbuildmat.2013.11.055.

[66] M.R.M. Aliha, H. Behbahani, H. Fazaeli, M.H. Rezaifar, Study of characteristic specification on mixed mode fracture toughness of asphalt mixtures, Constr. Build. Mater. 54 (2014) 623–635. doi:10.1016/j.conbuildmat.2013.12.097.

[67] M. Ameri, A. Mansourian, S. Pirmohammad, M.R.M. Aliha, M.R. Ayatollahi, Mixed mode fracture resistance of asphalt concrete mixtures, Eng. Fract. Mech. 93 (2012) 153–167. doi:10.1016/j.engfracmech.2012.06.015.

[68] M.R.M. Aliha, A. Bahmani, S. Akhondi, Determination of mode III fracture toughness for different materials using a new designed test configuration, Mater. Des. 86 (2015) 863–871. doi:10.1016/j.matdes.2015.08.033.

[69] M.R.M. Aliha, A. Bahmani, S. Akhondi, A novel test specimen for investigating the mixed mode I+III fracture toughness of hot mix asphalt composites - Experimental and theoretical study, Int. J. Solids Struct. 90 (2016) 167–177. doi:10.1016/j.ijsolstr.2016.03.018.

[70] M.R.M. Aliha, A. Razmi, A. Mansourian, The influence of natural and synthetic fibers on low temperature mixed mode I+ II fracture behavior of warm mix asphalt (WMA) materials. Engineering Fracture Mechanics. (2017) 322-336. doi: 10.1016/j.engfracmech.2017.06.003

[71] F. Zhou, D. Newcomb, C. Gurganus, S. Banihashemrad, E.S. Park, M. Sakhaeifar, R. L. Lytton, Experimental Design for Field Validation of Laboratory Tests to Assess Cracking Resistance of Asphalt Mixtures, Project No. 9-57, National Cooperative Highway Research Program of the Transportation Research Board of the National Academies. Washington, DC.

[72] M. Wagoner, W. Buttlar, G. Paulino, P. Blankenship, Investigation of the Fracture Resistance of Hot-Mix Asphalt Concrete Using a Disk-Shaped Compact Tension Test, Transp. Res. Rec. 1929 (2005) 183–192. doi:10.3141/1929-22.

[73] H. Kim, M.P. Wagoner, W.G. Buttlar, Numerical fracture analysis on the specimen size dependency of asphalt concrete using a cohesive softening model, Constr. Build. Mater. 23 (2009) 2112–2120. doi:10.1016/j.conbuildmat.2008.08.014.

[74] R.J. Sanford, *Principles of Fracture Mechanics*, first ed., Upper Saddle River, New Jersey, 2003.

[75] M. Janssen, J. Zuidema, R. Wanhill, *Fracture Mechanics*, second ed., New York, NY, 2004.

[76] T.L. Anderson, *Fracture Mechanics Fundamentals and Applications*, second ed., Boca Raton, Florida, 1995.

[77] ASTM E399-12e3, Standard test method for linear-elastic plane-strain fracture toughness K_{ic} of metallic materials, ASTM International, West Conshohocken, PA, 2012, doi:10.1520/E399-12E03.

[78] ASTM E1820-16, Standard test method for measurement of fracture toughness, ASTM International, West Conshohocken, PA, 2016, doi:10.1520/E1820-16.

[79] AASHTO T312-15, Preparing and determining density of hot mix asphalt (hma) specimens by means of the superpave gyratory compactor, AAHSTO, Washington, DC, 2015.

[80] ASTM D6925-15, Standard Test Method for Preparation and Determination of the Relative Density of Asphalt Mix Specimens by Means of the Superpave Gyratory Compactor, ASTM International, West Conshohocken, PA, 2015, doi:10.1520/D6925-15.

4. Fatigue Crack Growth of A Hot Mix Asphalt Using Digital Image Correlation

Calvin M. Stewart and Eduardo Garcia
Department of Mechanical Engineering
The University of Texas at El Paso
500 West University Avenue
Suite A126
El Paso, TX 79968-0521

To be submitted to the International Journal of Fatigue

4.1. Abstract

Cracks in hot mixed asphalts (HMAs) are tortuous and difficult to track using traditional crack length measurement techniques. The objective of this study is to demonstrate that digital image correlation can be employed to tracking crack propagation and produce more accurate measurements of the fracture and fatigue resistance of HMAs. Indirect tensile, fracture toughness, and fatigue crack growth (FCG) experiments on a dense-grade HMA at 5, 25, and 40°C are performed. Digital image correlation is shown to capture the crack propagation, crack tip remodeling, fatigue process zone, and strain distribution on the surface of the specimens. The fatigue crack growth rate versus stress

intensity factor is calculated and the Paris law constants measured. Microstructurally-small cracking is observed; where cracking is extremely sensitive to microstructural features. A complex combination of accelerating and retarding cracking mechanisms are observed to contribute to the tortuous, deflective, and bifurcative cracking observed in the HMA.

4.2. **Highlights**

- The fatigue crack growth of hot mix asphalt is studied using linear elastic fracture mechanics.
- Digital image correlation is applied to study the fatigue process zone.
- Distinct fracture mechanics are observed at low and elevate temperature.
- Microstructurally small crack growth is observed at elevated temperature.
- Aggregates act as obstacles accelerating and decelerating crack growth.

4.3. **Graphical Abstract**

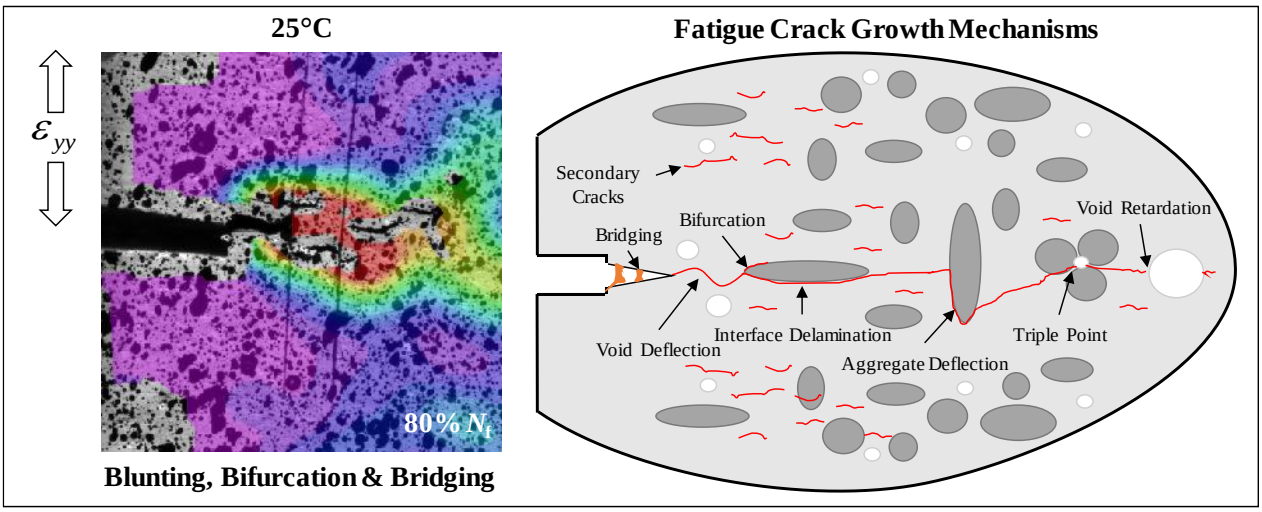

Figure 4.1 – Graphical Abstract

4.4. Introduction

4.4.1. Motivation

Asphalt pavements are subjected to varied traffic loads and climate during service. These periodic boundary conditions contribute to numerous forms of pavement distress. The most prevalent distress in asphalt pavements is fatigue cracking. Fatigue failure is often difficult to predict due to the poor repeatability of asphalt fracture and fatigue tests. The uncertainty of asphalt testing is attributed to

a) the heterogeneous nature of asphalt mixture where the randomly distributed aggregates can produce specimen-specific cracking (i.e., non-planar cracking that is unique to the microstructure in a specimen);
b) the diversity of test methods (specimen geometry, pre-conditioning, loading condition and rate, post-processing of data, etc.) which make it a challenge to separate test-related uncertainties;
c) and the wide assortment of material compositions and temperature profiles (across the world) which make the fracture and fatigue mechanics specific to the selected composition and region of interest.

Recently, a critical review of the state of the art and practice in fatigue cracking evaluation of asphalt concrete pavements was performed involving over fifty leader researchers and organizations [81]. Overall, considerable work has been performed in improving the testing and evaluation of the fatigue-life of pavements; however, comparatively fewer studies have been performed concerning fatigue crack growth.

4.4.2. **Fatigue-Life**

Fatigue-life testing involves subjecting an un-notched specimen to periodic boundary conditions to failure. Failure can be characterized as fracture, a designated loss-of-stiffness, or other loss-of-function parameters. These tests can be said to encompass both crack nucleation (where both surface and sub-surface defects grow into micro-cracks) and crack propagation (where the micro-cracks are of suitable length to align and generally grow perpendicular to the principal loading direction). Typically, crack length is not tracked; rather, other performance metrics such as stress, strain, strain energy, stiffness, etc. are plotted with respect to the cycles to failure, N_f [81]. Several standards are under development to characterize the fatigue-life of asphalt mixtures. One of the earliest and well-established fatigue-life tests, is the 4-point bending test performed on compact beam specimens according to the full ASTM D7460-10 and AASHTO TP321 standards [82,83]. During this test, specimens are subjected to cyclic strain-control to generate a strain-life curve. Fatigue failure is identified as the point where the normalized modulus x cycles is maximized (ASTM) or at a 50% reduction in stiffness (AAHSTO) [84]. Using this data, a variety of strain-life models can be applied to predict life. A more recent fatigue test is a uniaxial fatigue test performed on cylindrical specimen according to provisional standard AASHTO TP107 [87]. During this test, the viscoelastic continuum damage (VECD) approach is applied for life-prediction where the distributed defects within the material are idealized as a phenomenological variable called damage [85,86]. The results of uniaxial fatigue and dynamic modulus tests are applied to generate damage characteristics curves (i.e. pseudo stiffness versus damage

plots). Life-predictions are made using either the pseudo strain-, pseudo strain energy release rate-, or cumulative pseudo stiffness-life curves [88]. This approach has been successfully used to predict bottom-up and top-down fatigue cracking at various load and thermal conditions. When studying pure asphalt binder, the Linear Amplitude Sweep (LAS) test is recommend where systematically increasing strain amplitudes are applied in the dynamic shear rheometer (DSR) to characterize fatigue according to the provisional AAHSTO TP 101-12 [89]. A simplified viscoelastic continuum damage (S-VECD) model is applied for life prediction [90]. Recent studies show that cracking primary occurs within the asphalt or at the asphalt-aggregate interfaces, such that the cracking of pure asphalt binder has a strong correlation to the fatigue performance of mixtures [91]. Another modern fatigue test for asphalt pavements is the Overlay test where rectangular specimens are subject to cyclic displacement-controlled fatigue (applied to the bottom of specimen) according to Tex-248-F [92]. The Overlay test is designed to simulate the reflective cracking of flexible pavements where the opening and closure of joints/cracks in the old pavement below the overlay induce crack nucleation and propagation. Fatigue-life predictions encapsulate both crack nucleation and propagation process using the strain-life and linear elastic fracture mechanics approaches respectively [93]. The crack length is not tracked during this test, so the crack growth rates are estimated using finite element simulations. Beyond these provisional and full standards, many attempts to use alternative geometry (such as the Marshall, indirect tension, dog-bone, trapezoidal, load wheel tester, etc.), failure criterion

(plateau value of the ratio of dissipated energy change, etc.) and life prediction models have been explored [81,94,95].

4.4.3. **Fatigue Crack Growth**

Relatively fewer studies into the fatigue crack growth (FCG) behavior of HMAs have been performed. This is primary due to the difficultly with tracking the crack as it oscillates through heterogeneous HMA. Fatigue crack growth tests are typically performed on notched specimen which have been specially preconditioned to simulate a fully developed crack (bypassing the crack nucleation phase). Often, FCG predictions are made using one of four approaches: linear-elastic fracture mechanics (LEFM), elastoplastic fracture mechanics (EPFM), nonlinear/time-dependent fracture mechanics (NLFM/TDFM), or VECD-based parameters. While many standards exist for measure the fracture parameters in HMAs [96,97]; standards for FCG in HMAs are lacking. The lack of standards has led to a large diversity of studies with various geometry, failure criterion, and prediction models [81,98-106]. For crack propagation using LEFM, the stress intensity factor, K_I is calculated as

$$K_i = f\left(\sigma, a, X_n\right) \tag{6}$$

where σ is the applied stress, a is the crack length, and X_n are the dimensions of the specimen that influence the K_I. Fracture occurs when K_I is greater than or equal to the fracture toughness, K_{Ic} material property. It is essential for the crack length to be tracked throughout testing to accurately calculate the K_I during a test. Since, K_I does

not depend on material properties, the relationship between the K_I and a is approximated using the analytical solution of Euler's equilibrium equations (balance of energy and balance of linear and angular momentum) or, for more complex geometry, finite element analysis (traditional, cohesive-zone, continuum damage mechanics, etc.) [98]. Unfortunately, this approach is based on continuum mechanics which assumes that matter is continuously distribution everywhere within a volume. This idealization does not reflect the reality of asphalt pavements, where aggregates of diverse size and shape are heterogeneously distributed within the volume. In practice, the idealization is preserved. Zhou and Scullion used finite element analysis to approximate the relationship between K_I and a in an Overlay specimen [99]. Koohi switching to the strain energy release rate, J_I and developing a method to estimate crack growth incorporating healing effects [100]. Gu applied this procedure to estimate the Paris law constants of field aged concrete [101,102]. Literature review finds that FCG tests have been performed in many configurations including the overlay test (OT), notched indirection tension (n-IDT), semi-circular bending (SCB), disk-shaped compact tension (DCT), single edge notched beam (SENB), double edge notched prism (DENP), wedge splitting (WS), etc. [103-106]. In most of these studies the crack length is not physically measured.

4.4.4. Crack Length Measurement

Few FCG studies physically measure the crack length [105-107]. In these studies, a diverse set of crack length measurement techniques are applied. The simplest approach is to affix a series of strain gauges and/or conductive wires across the crack path to

detect crack growth [105, 106]. More advanced techniques utilize optics to track the crack [107-109]. These methods achieved limited success due to the fineness of cracks preventing consistent tracking. To overcome these issues, Muniandy and colleagues developed the crack meandering technique and software for more consistent identification of fine cracks [110]. Computed tomography has also been employed to evaluate the volumetric distribution of fatigue cracks in HMA; however, these scans are not performed in real-time and the evaluation and implementation of the data into prediction models is a challenge [111].

4.4.5. Digital Image Correlation

An alternative crack length measurement technique is to employ digital image correlation (DIC). Digital image correlation (DIC) is an optical non-contact method for measuring the displacement and strain field on the surface of objects. The advantage of DIC over traditional devices such as strain gauges, LVDTs, and extensometers is that DIC provides local information that is not restricted by gauge length but rather resolution (i.e. pixel density) enable measurements ranging from the atomistic to geophysical scale [112]. The advantage of DIC over the crack meandering technique is that the displacement and strain fields are tracked; such that crack opening is readily identified even when it is not apparent upon visual inspection. In DIC, a speckle pattern is applied to the specimen and digital images taken during testing. The speckles act as reference points enabling the relative displacement on the surface of the specimen to be tracked

(using a selected cross-correlation criterion) and the displacement gradient and strain calculated according to continuum mechanics [113].

In asphaltic mixtures, DIC has been applied to assess the adequacy of test standards [96,114-36] and elucidate the fracture process zone (FPZ) [118-122]. Recently, DIC has been employed to study the tensile strain ahead of the crack tip in HMA during isothermal fatigue [123]. It has yet to be employed to aid crack length measurement.

4.4.6. Problem Statement

It is evident that crack length is not typically tracked during fracture and fatigue testing of HMAs. In addition, the large variety of geometry, test methods, and modeling approaches make it difficult to assess the fracture and fatigue crack growth of HMAs. There is a need to implement a high-fidelity and consistent technique for crack length measurement. It is hypothesized that DIC can be used for this purpose.

4.5. OBJECTIVE

The objective of this study is to demonstrate that DIC can be employed to tracking crack propagation and produce more accurate measurements of the fracture and fatigue resistance of HMAs. To achieve this objective, disk-shaped compact tension (DCT) specimens of a dense-grade HMA are prepared. Preliminary experiments including indirect tensile and fracture toughness tests are conducted at 5, 25, and 40°C. Fatigue crack growth tests are performed on pre-cracked specimen under load-control at a stress ratio of $R = 0.1$ and frequency of $f = 0.1\ \mathrm{Hz}$. Digital image correlation (DIC) is employed to compute the crack length and study the crack tip remodeling, fracture and

fatigue process zone, and strain distribution on the surface of the specimens. As a supplemental, the Paris law is applied to study the intensity and uncertainty of crack growth with respect to temperature.

4.6. Material And Test Methods

4.6.1. Dense Grade Hot Mix Asphalt (HMA)

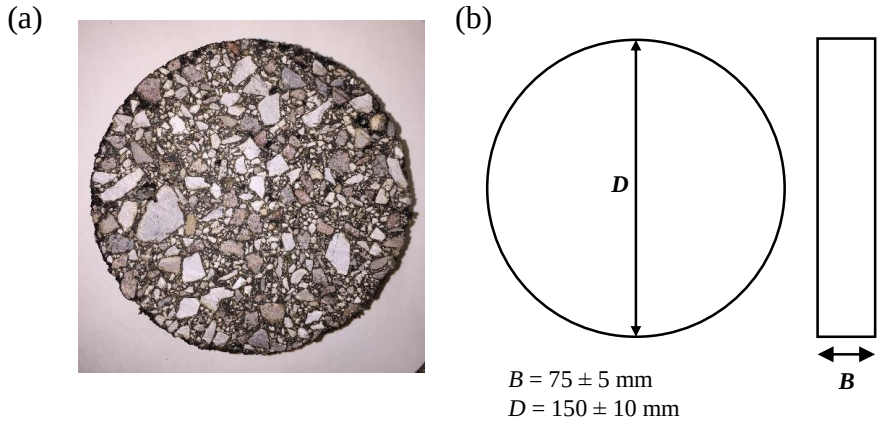

Figure 4.2 – Indirect tension (IDT) specimen (a) photo and (b) dimensions

In this study, the subject material is a dense graded hot mix asphalt (HMA) used in West Texas. The gradation of the mix is shown in Table 4.1. The asphalt performance grade, binder substitution, asphalt content, and other material properties are shown in Table 4.2. The general distribution of aggregates in the asphalt binder matrix is depicted in Figure 4.2a with the dimensions of the disk illustrated in Figure 4.2b.

Table 4.1 – Gradation chart of Type-C mix

Sieve Size	Percentage
1’’	100.0
3/4”	99.3
3/8”	82.4
No.4	52.7
No. 8	36.9
No. 30	18.6
No. 50	14.0
No. 200	5.6

Table 4.2 – Material properties of Type-C mix

NMAS (mm)	19
Asphalt Performance Grade	PG 70-22
Binder Substitution	PG 64-22
Optimal Asphalt Content (%)	4.7
Specific Gravity	1.001
Binder Percent (%)	4.6
VMA (%) at optimum AC	15.2

4.6.2. **Specimen Preparation**

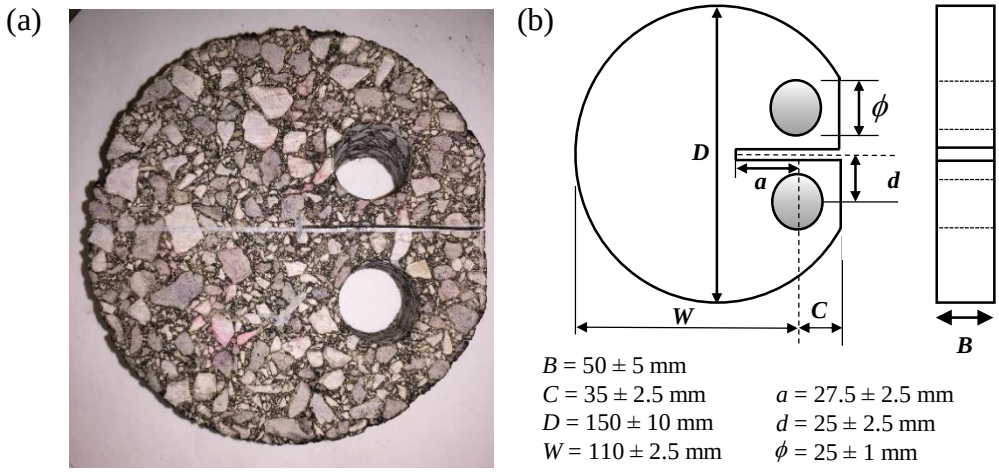

Figure 4.3 – Disk-shaped compact tension (DCT) specimen (a) photo and (b) dimensions

Two types of specimen are prepared for this study: indirect tension (IDT) and disk-shaped compact tension (DCT) as depicted in Figure 4.2a and Figure 4.3a respectively. The dimensions of these specimens are illustrated in Figure 4.2b and Figure 4.3b respectively. The specimens are manufactured according to AASHTO T312-15 and ASTM D6928-15 [124, 125]. The crack mouth, load holes, and notch are fabricated using a water-cooled saw in accordance with ASTM 7313-13 [126]. The notch is cut using a bandsaw.

4.6.3. Mechanical Test Equipment

The IDT tests are conducted in an MTS 810 Universal Test System (UTM) while the DCT specimens are conducted in an Instron 5969 Table-top UTM. The servo-hydraulic MTS 810 is equipped with an 11-kip load cell and resides within a walk-in temperature and humidity-controlled room. The electro-mechanical Instron 5969 is equipped with a 50 kN load cell and configured with a 3119-609 environmental chamber enabling temperature control from -100 to +350°C. Specimen are preconditioned to an isothermal set temperature before testing and held at that temperature for the duration of each experiment.

4.6.4. Indirect Tension Tests

The indirect tensile tests (IDT) are conducted to determine the tensile strength of the asphalt mixture according to the ASTM D6931-12 [127]. During the test, load is applied on the vertical diametral plane of the specimen at a constant displacement rate until

rupture or the load drops below 40 N. The tests are run at a displacement rate of 50 mm/min at three isothermal set temperatures; 5, 25, and 40°C respectively. The specimens were precondition overnight (>8 hrs) before testing. The IDT strength, S_t is calculated as follows

(7) $$S_t = \frac{2P_{\max}}{\pi BD}$$

where $P_{\max}$ is the maximum load, B is the specimen thickness, and D is the specimen diameter [127].

4.6.5. **Fracture Toughness**

Fracture toughness tests are performed according to ASTM E399-12 the “standard test method for plane-strain fracture toughness of metallic materials” [128]. The DCT specimen dimensions depicted in Figure 4.3b are according to ASTM 7313-13 [126]. In this study, the plane-strain criterion from ASTM E399-12 is employed as follows

(8) $$2.5\left(\frac{K_{Ic}}{\sigma_{YS}}\right)^2 \leq (W-a)$$

where K_{Ic} is the approximate plane-strain fracture toughness, σ_{YS} is the yield strength, and $(W-a)$ is the initial ligament length [128]. According to [Eq. (8)] and preliminary

data recorded in this study, the current DCT dimensions are inadequate to achieve the plane-strain condition in the material at all three temperatures. Thus, according to ASTM E399-12, the fracture toughness recorded in this study hereon is defined as the "apparent" fracture toughness and reported everywhere with respect to the thickness [128].

Another requirement for a valid K_{Ic} is that the elastic regime not exceed a certain degree of nonlinearity. For, the calculated K to bear relation to K_{Ic}, the condition

$$P_{\max}/P_Q \leq 1.10 \quad (9)$$

must be true where $P_{\max}$ is the maximum load during the test and P_Q is the intersect point of the 95% slope secant line starting at the initial nonlinearity of the force vs displacement curve. In the current study, the material meets this requirement at all temperatures.

Pre-cracking is an important procedure that conditions (sharpens) the machined notch tip to simulate a "real" fully developed crack in a structure. Few pre-cracking procedures have been performed for HMAs [129]. In this study, the DCT specimens are subjected to fatigue pre-cracking per ASTM E647-15 [130]. The maximum stress intensity factor, $K_{\max}$, during pre-cracking must not exceed 60% of the estimated plane-strain fracture toughness K_{Ic} at a force ratio R of 0.1. An estimate of K_{Ic} and subsequently $K_{\max}$ is

calculated using [Eq. (8)]. All stress intensity factors, K are calculated according to ASTM E399-12 as follows

(10) $$K = \frac{P}{B\sqrt{W}} f\left(a/W\right)$$

where *P* is the load, B is the specimen thickness, W is the specimen width, and $f\left(a/W\right)$ is the geometry factor calculated as

(11) $$f\left(a/W\right) = \frac{\left(2+\frac{a}{W}\right)\left[0.76+4.8\frac{a}{W}-11.58\left(\frac{a}{W}\right)^2+11.43\left(\frac{a}{W}\right)^3-4.08\left(\frac{a}{W}\right)^4\right]}{\left(1-\frac{a}{W}\right)^{3/2}}$$

where a is the crack length measured from the load-line as depicted in Figure 4.3b. According to ASTM E647-15, fatigue pre-cracking must continue until the crack has extended $\geq 0.1B$ (e.g. ≥5 mm) beyond the initial notch length. In this study, due to the large aggregates present in the material, pre-cracking is performed until the crack grew $\geq 0.2B$ (e.g. ≥10 mm). The length of the pre-crack on the front and back of the specimen must remain within $0.25B$ of each other. The ASTM E647-15 standard requires that the crack not deviate from the plane of symmetry by more than $\pm 20°$; however, due to the large aggregates this condition is not enforced. The pre-cracking parameters at each temperature are listed in Table 4.3.

Table 4.3 – Pre-cracking parameters

Temperature, *T* (°C)	Maximum Stress Intensity, K_{max} ($\mathrm{MPa}\sqrt{\mathrm{m}}$)	Load Range, ΔP (N)	Stress Intensity Range, ΔK ($\mathrm{MPa}\sqrt{\mathrm{m}}$)
5	0.340	900	0.3060
25	0.085	225	0.0765
40	0.018	36	0.0162

Fracture toughness tests are conducted at a constant rate. Here the load rate applied in ASTM E399-15 for metallic materials is not appropriate for HMAs due to the extremely low strength of HMAs. Instead, ASTM 7313-13 is applied at a crack mouth opening displacement (CMOD) rate of 0.017 mm/s.

4.6.6. **Fatigue Crack Growth Tests**

Fatigue crack growth (FCG) tests are conducted following the ASTM E647-15 “standard test method for measurement of fatigue crack growth rates” [130]. The dimensions of the specimen are kept according to ASTM 7313-13 [126]. Pre-cracking is carried out according to Table 4.3. During FCG testing, load-controlled fatigue is performed at a stress ratio of $R = 0.1$ and frequency of $f = 0.1\ \mathrm{Hz}$ with a triangular waveform. The FCG test parameters at each temperature are listed in Table 4.4. Different stress intensity ranges, ΔK are applied at each temperature to remain below the temperature-dependent K_c. The crack growth rate is calculated using both the secant (SM) and incremental polynomial methods (IPM) for data reduction [130].

Table 4.4 – Fatigue crack growth test parameters

Temperature, T (°C)	Load Range, ΔP (N)	Stress Intensity Range, ΔK ($\mathrm{MPa}\sqrt{\mathrm{m}}$)
5	900	0.2430
25	90	0.0283
40	*NA	*NA

*NA – Not Applicable due to failure at load holes

4.6.7. **Three-Dimensional Digital Image Correlation (3D-DIC)**

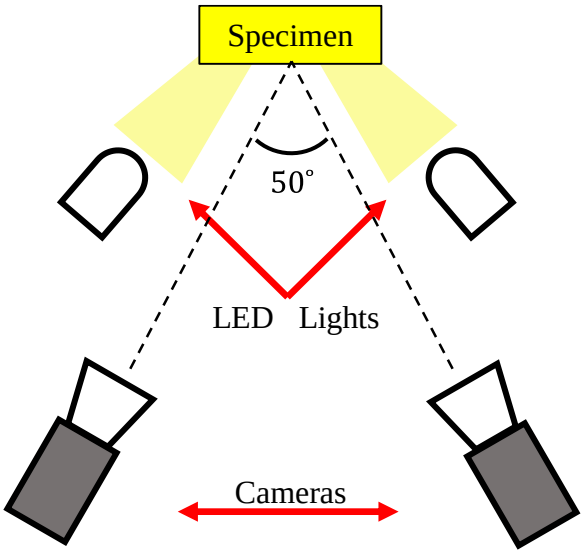

Figure 4.4 – DIC system

Three-dimensional digital image correlation (3D-DIC) is performed using equipment and software (VIC-Snap, VIC-Gauge, and VIC-3D) developed by Correlated Solutions. An illustration of the DIC system is illustrated in Figure 4.4. The system consists of two 17-mm CCD cameras and two tunable LED lights focused on a speckled specimen. The cameras are precisely leveled and inclined at an angle of 25° or greater. Using the VIC-Snap software, high-contrast photos are taken of the specimen during testing.

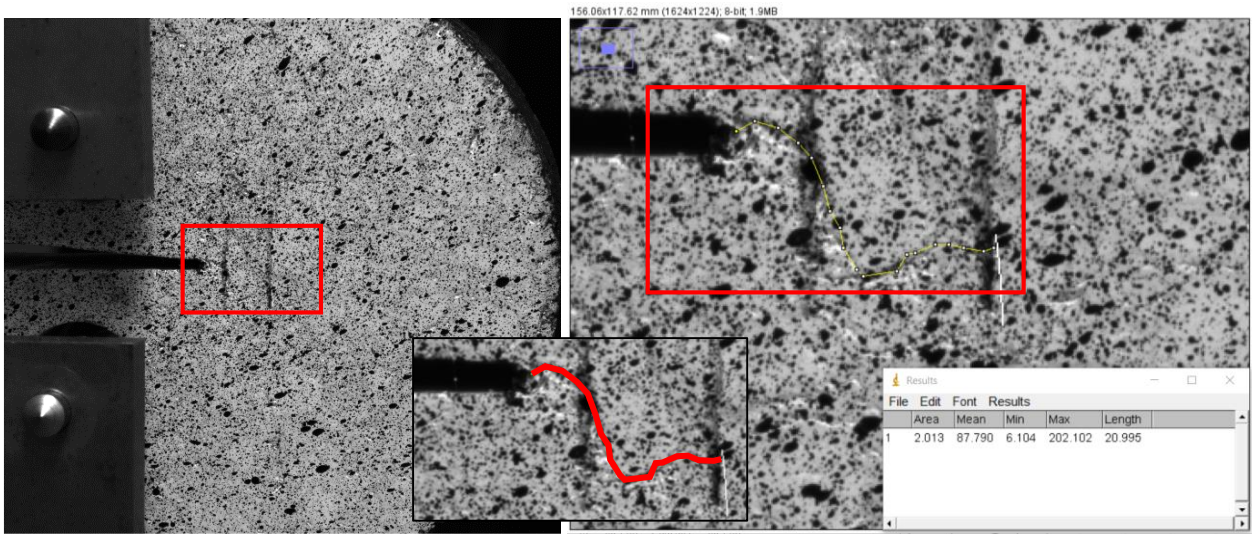

Figure 4.5 – Crack length measurement

The displacement and strain fields on the surface of the specimen are calculated using the VIC-3D software. Specimens are prepared with a random speckle pattern using spray-paint as shown in Figure 4.5. These speckles create subsets that the software tracks. The software calculates the displacement vector (*u*, *v*, and *w*) and subsequently the strain vector on the surface of the specimen. Calibration is performed prior to each test where a calibration square is photographed to provide a physical reference of distance.

The crack length is measured by superimposing strain fields over the photos to produce high-fidelity and consistent crack length measurements even when the crack is not readily apparent. For example, the crack depicted in Figure 4.5 is not visually perceptible. The DIC contours were applied to identify the crack. Photos are captured at the peak load with a frequency of 0.1 Hz. The crack length is measured every 30 cycles

at 5°C and every 50 cycles at 25°C. Measurements are taken from the front of the specimens only.

4.7. Results And Discussion

4.7.1. Indirect Tensile Strength

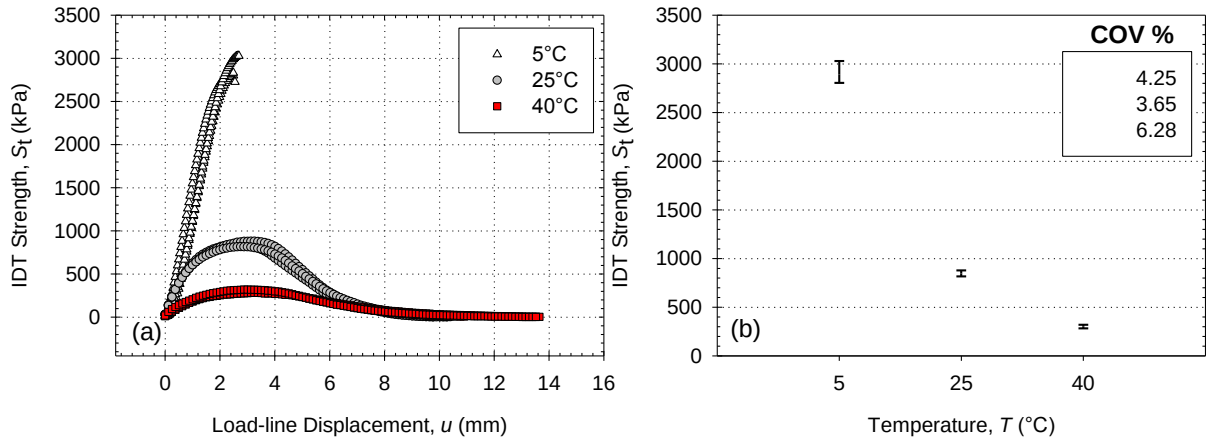

Figure 4.6 – IDT (a) strength-displacement and (b) strength-temperature

Table 4.5 – Indirect tensile strength properties

Specimen No.	Temperature, T (°C)	Air Voids, AV (%)	Max. Load, P_{max} (kN)	IDT Strength, S_t (KPa)	IDT Strength, S_t Avg. (KPa)	IDT Strength, S_t Std. Dev. (KPa)	IDT Strength, S_t COV (%)
IDT5-1	5	6.8	35.28	2805.36	2889.52	±122.84	4.25
IDT5-2	5	7.5	35.63	2832.71	2889.52	±122.84	4.25
IDT5-3	5	7.2	38.11	3030.49	2889.52	±122.84	4.25
IDT25-1	25	7.9	10.99	850.59	849.15	±30.98	3.65
IDT25-2	25	6.6	11.06	879.45	849.15	±30.98	3.65
IDT25-3	25	7.8	10.29	817.48	849.15	±30.98	3.65
IDT40-1	40	7.6	3.81	303.21	302.73	±19.00	6.28
IDT40-2	40	7.0	3.56	283.58	302.73	±19.00	6.28
IDT40-3	40	6.5	4.04	321.53	302.73	±19.00	6.28

The IDT strength-displacement and strength-temperature graphs are shown in Figure 4.6 with the results summarized in Table 4.5. As temperature increases from 5 to 40°C, the constitutive behavior of the material changes from linear-elastic-brittle to viscoelastic-plastic. The average strength logarithmically decreases with increased temperature. The Coefficient of variation (COV) of the IDTs remains low (<7%) and does not trend with temperature.

4.7.2. **Apparent Fracture Toughness**

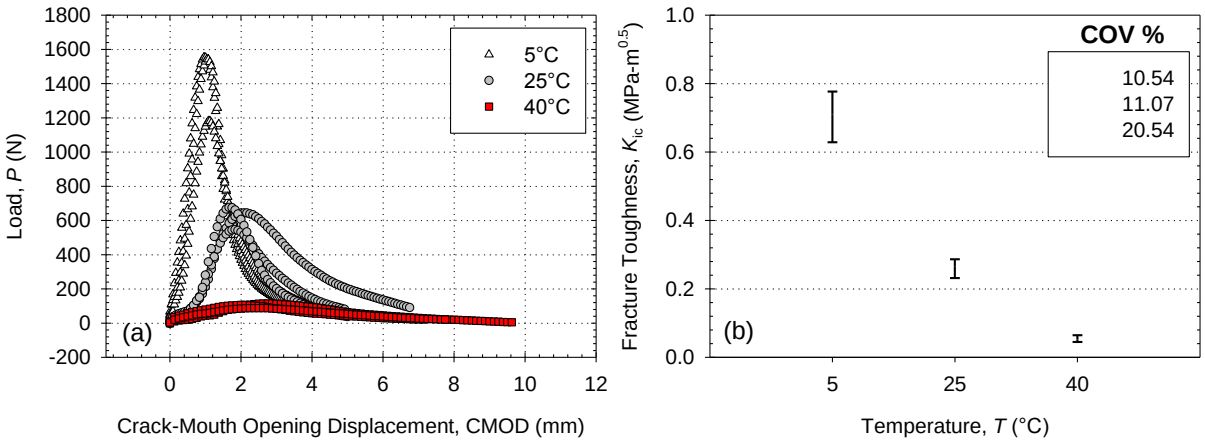

Figure 4.7 – Apparent fracture toughness (a) load-CMOD and (b) strength-temperature

Table 4.6 – Apparent fracture toughness properties at $B = 50 \pm 5\text{mm}$

Specimen No.	Temperature, T (°C)	Air Voids, AV (%)	Notch Length, a (mm)	Apparent Fracture Toughness, K_c ($\text{MPa}\sqrt{\text{m}}$)	Apparent Fracture Toughness, K_c Avg. ($\text{MPa}\sqrt{\text{m}}$)	Apparent Fracture Toughness, K_c Std. Dev. ($\text{MPa}\sqrt{\text{m}}$)	Apparent Fracture Toughness, K_c COV (%)
K5-1	5	7.2	46.88	0.777	0.709	±0.074	10.56
K5-2	5	6.9	43.75	0.722	0.709	±0.074	10.56
K5-3	5	6.9	48.97	0.629	0.709	±0.074	10.56
K25-1	25	7.3	38.47	0.232	0.265	±0.029	11.07
K25-2	25	6.8	40.30	0.287	0.265	±0.029	11.07
K25-3	25	6.4	47.77	0.276	0.265	±0.029	11.07
K40-1	40	6.3	39.21	0.045	0.053	±0.010	20.54
K40-2	40	7.4	52.72	0.065	0.053	±0.010	20.54
K40-3	40	7.5	50.82	0.049	0.053	±0.010	20.54

The load-CMOD and apparent fracture toughness-temperature graphs are shown in Figure 4.7 with the results summarized in Table 4.6. Unlike the IDT tests, the fracture toughness specimens were pre-cracked. The average apparent fracture toughness decreases as temperature increases. These properties reflect literature [96, 131]. The COV of the apparent fracture toughness increases with temperature. The high COV at 40°C is due to both the low force exerted on the specimen and tendency of the bitumen to flow at elevated temperature while the aggregates remain stiff.

4.7.3. **DIC of Fracture Toughness**

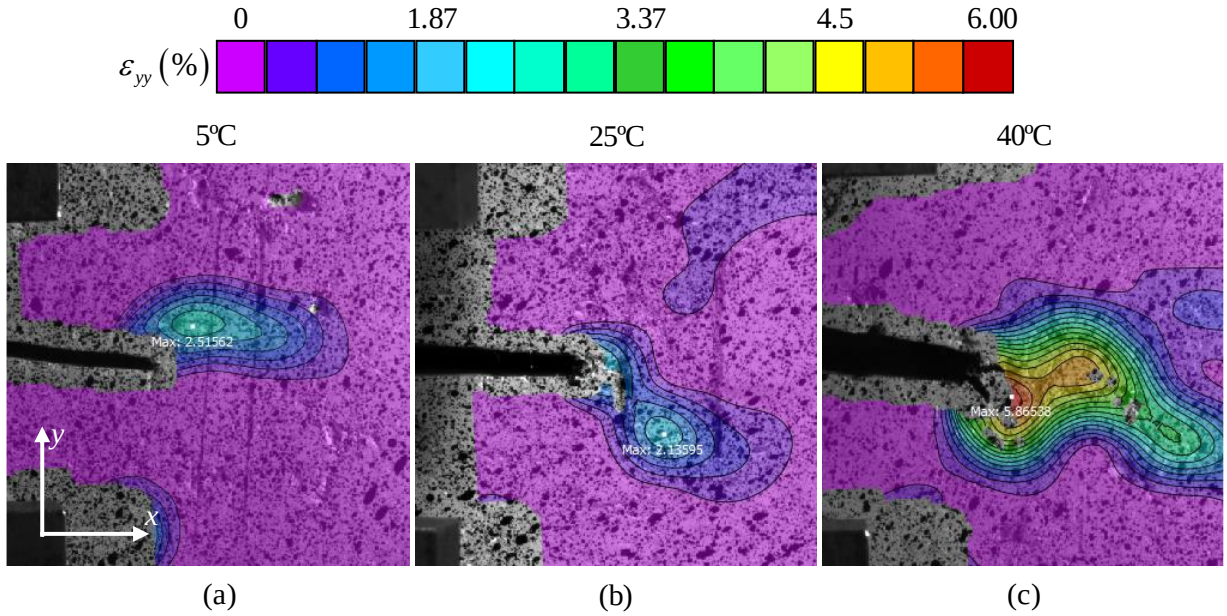

Figure 4.8 – Contours of longitudinal percent strain, ε_{yy} (%) at the maximum load during fracture tests

Digital image correlation was performed on the fracture toughness specimens. Contours of the longitudinal percent strain, ε_{yy} at the maximum load (the instant where the fracture toughness was measured) are depicted in Figure 4.8. The maximum strain at peak load increases with temperature. The size and intensity of the fracture process zone (FPZ) also increases with temperature. Notch tip blunting increases with temperature where yielding at the notch root remodels the shape of the notch reducing

the stress intensity. For temperatures 25ºC and above, secondary strain concentrations form due to material property mismatch between the bitumen and aggregate.

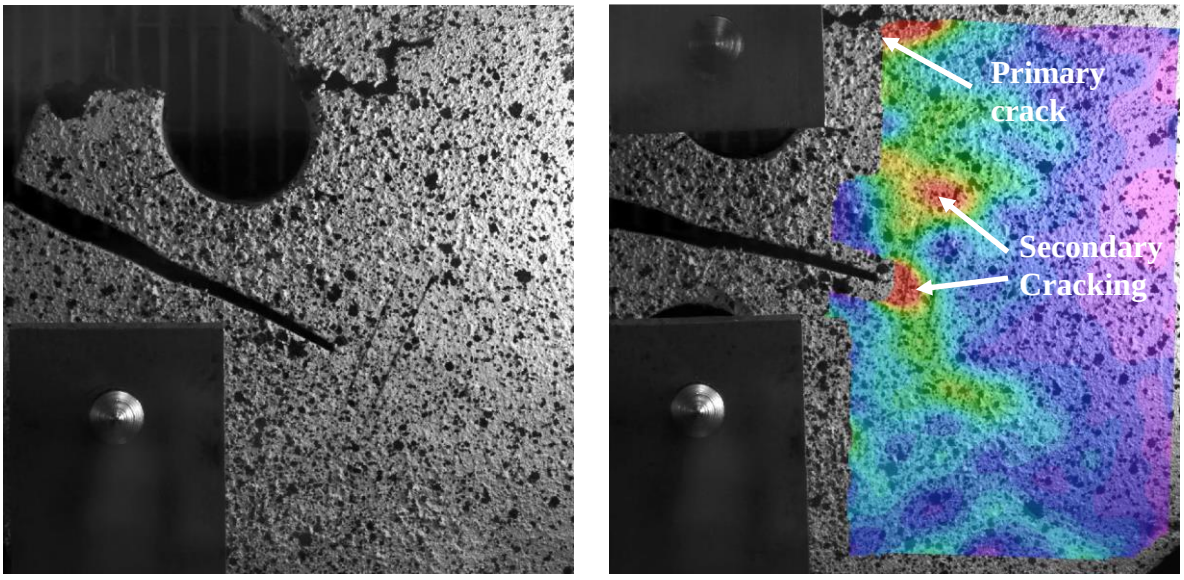

(a) (b)

Figure 4.9 – Loading hole failure at 40 ºC during FCG tests (a) photo and (b) DIC

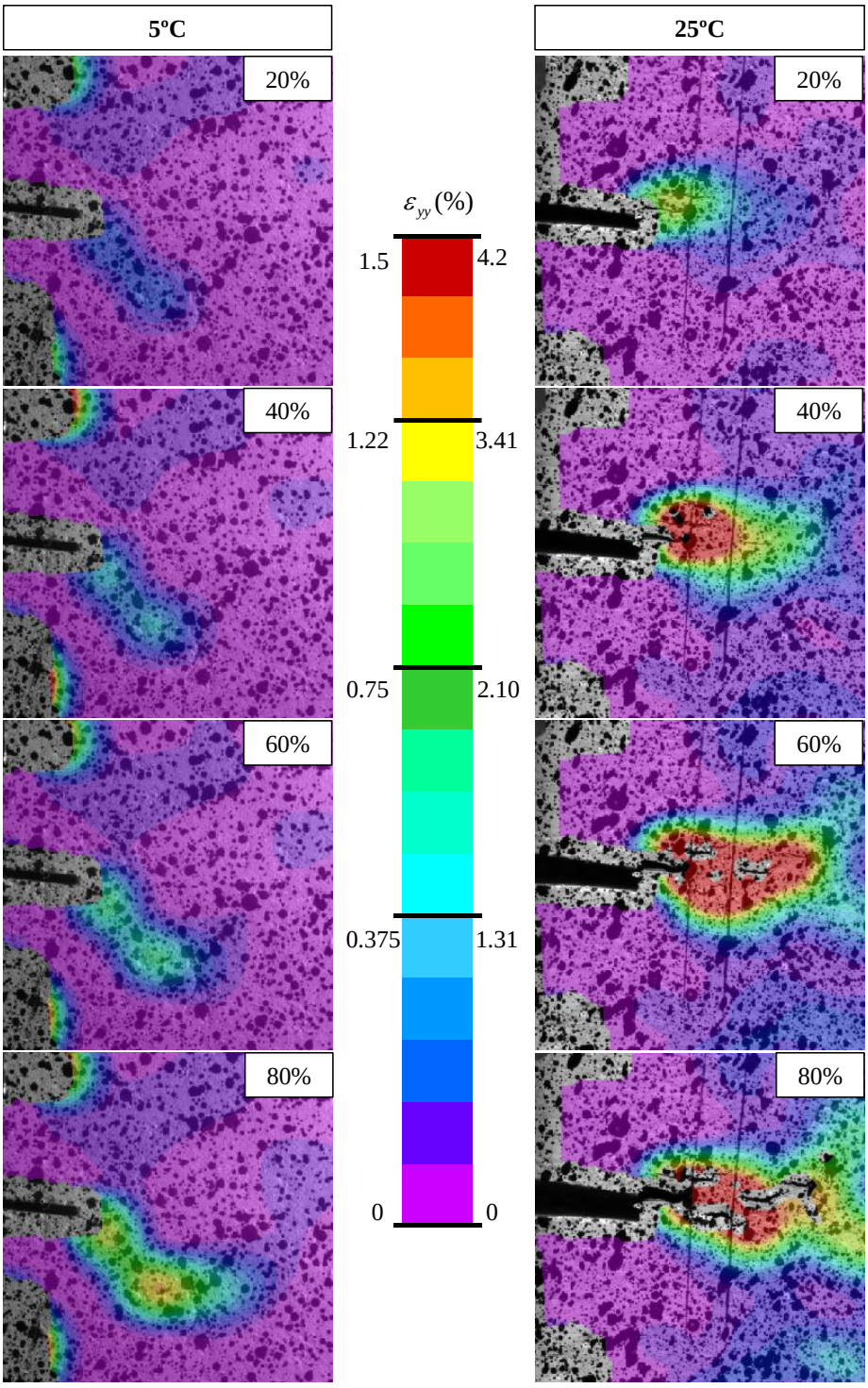

Figure 4.10 – Contours of longitudinal percent strain ε_{yy} (%) measured during FCG at various fatigue life fractions, n_i/N_f

4.7.4. DIC of Fatigue Crack Growth

To measure fatigue crack growth (FCG), digital image correlation was performed. The 40°C tests failed at the load holes as shown in Figure 4.9. During the pre-cracking procedure, the load holes are observed to distort but not crack. During FCG, excessive plastic deformation at the load holes contributed to crack initiation and propagation to the left and right of the holes. Digital image correlation shows that the primary crack developed at the top load hole with secondary cracking at the pre-cracked notch and within the asphalt matrix. This indicates there exists a critical temperature above which FCG testing is not feasible due to the malleability of the material. The 5ºC and 25ºC FCG tests did not exhibit this issue.

For the 5ºC and 25ºC FCG tests, contours of the longitudinal percent strain, ε_{yy} recorded at 20, 40, 60, and 80% of the fatigue life fraction, n_i/N_f are shown Figure 4.10. The 5°C FCG test is distinguished by limited cracking before fracture, localized strain, and low ductility. There is no notch tip blunting and the crack does not open making it difficult to distinguish crack extension except when the peak load is achieved during a cycle. Strain builds slowly ahead of the crack tip and remains localized due to the high strength asphalt-aggregate interfaces and asphalt matrix. Interestingly, secondary strain concentrations are observed above and below the machined notch. It is hypothesized that these strain concentrations represent microstructural defects that reduce the stress concentration at the machine notch tip and retarding crack extension. Crack extension remained short ($a =$ 29.28 to 59.51 mm) up to fracture.

The 25°C FCG test is distinguished by significant cracking before fracture, distributed strain (suggesting creep/viscoplasticity), and high ductility. The notch tip becomes blunt and the crack mouth opens with an appreciable angle as shown in Figure 4.10. Life is dominated by torturous crack extension with frequent crack deflections. The crack is observed to bridge (where secondary cracks nucleate ahead of the primary crack observe at life fractions 60%>) and bifurcate (where the primary crack branches into two or more subcracks one of which continues to propagate while the others arrest is observed at life fractions 80%>). These are symptoms of a weaker and more ductile asphalt matrix enabling a large fatigue process zone (FPZ) at the crack tip [106]. Crack extension was significant (a = 33.3 to 83.18 mm) up to fracture.

4.7.5. **Fatigue Crack Growth**

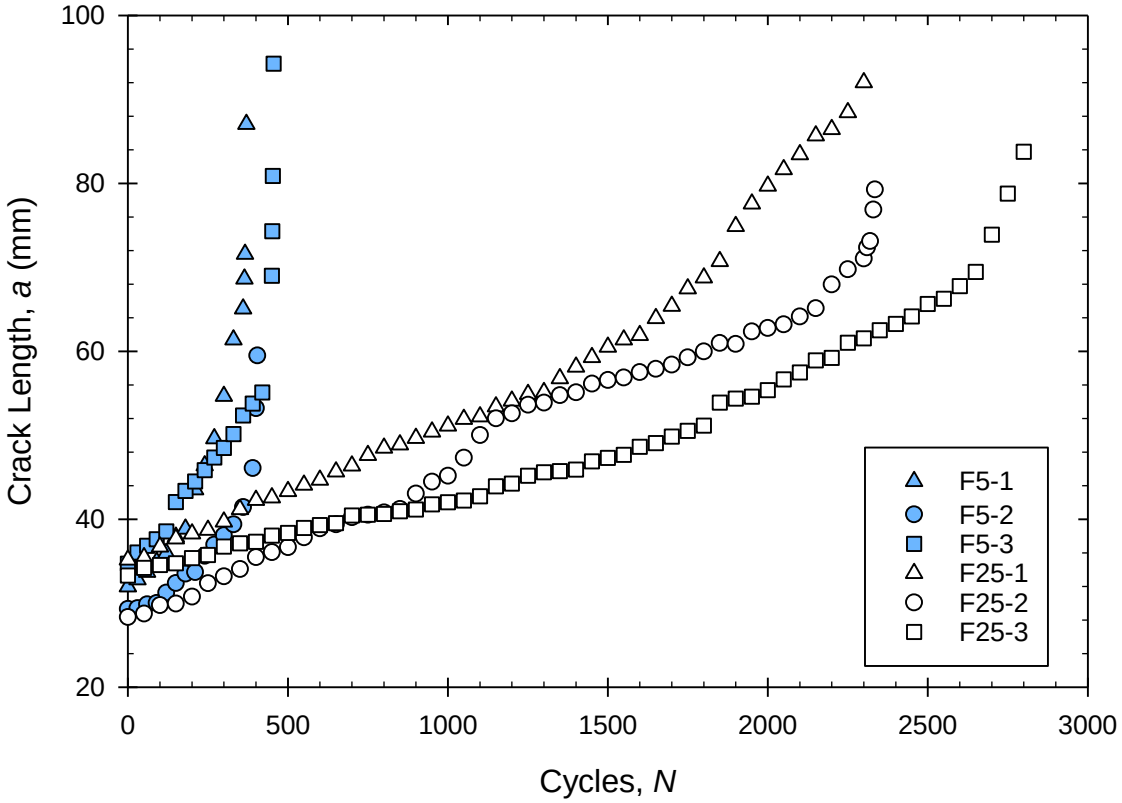

Figure 4.11 - Fatigue crack length (mm) versus cycles

Table 4.7 – FCG properties

Specimen No.	Temperature, T(°C)	Air Voids, AV(%)	Loading Range, ΔP (N)	Initial Notch Length, a (mm)	Cycles to Failure, N_f (cycles)
F5-1	5	6.8	900	31.97	371
F5-2	5	6.7	900	29.28	404
F5-3	5	7.6	900	34.70	455
F25-1	25	7.5	90	35.16	2300
F25-2	25	6.7	90	28.33	2330
F25-3	25	7.2	90	33.33	2840

Processing the DIC results, crack length versus cycles was calculated as presented in Figure 4.11 with the test conditions summarized in Table 4.7. At 5°C, FCG is unstable, accelerating rapidly to fracture. On average, fracture occurred within 410 cycles. At 25°C, FCG is dominated by what appears to be stable crack growth. Looking closer, the stable FCG oscillates. This instability is most noticeable in Specimen No. F25-2 where between 1000 to 1200 cycles the crack growth rate starts at a moderately level increases dramatically and then slowdowns to less than the initial value. These instabilities are related to the tortuous cracking of HMAs where the crack travels through the lowest energy path in the material (i.e, interaggregate, traveling through the binder and around the aggregates). On average, fracture occurred within 2490 cycles.

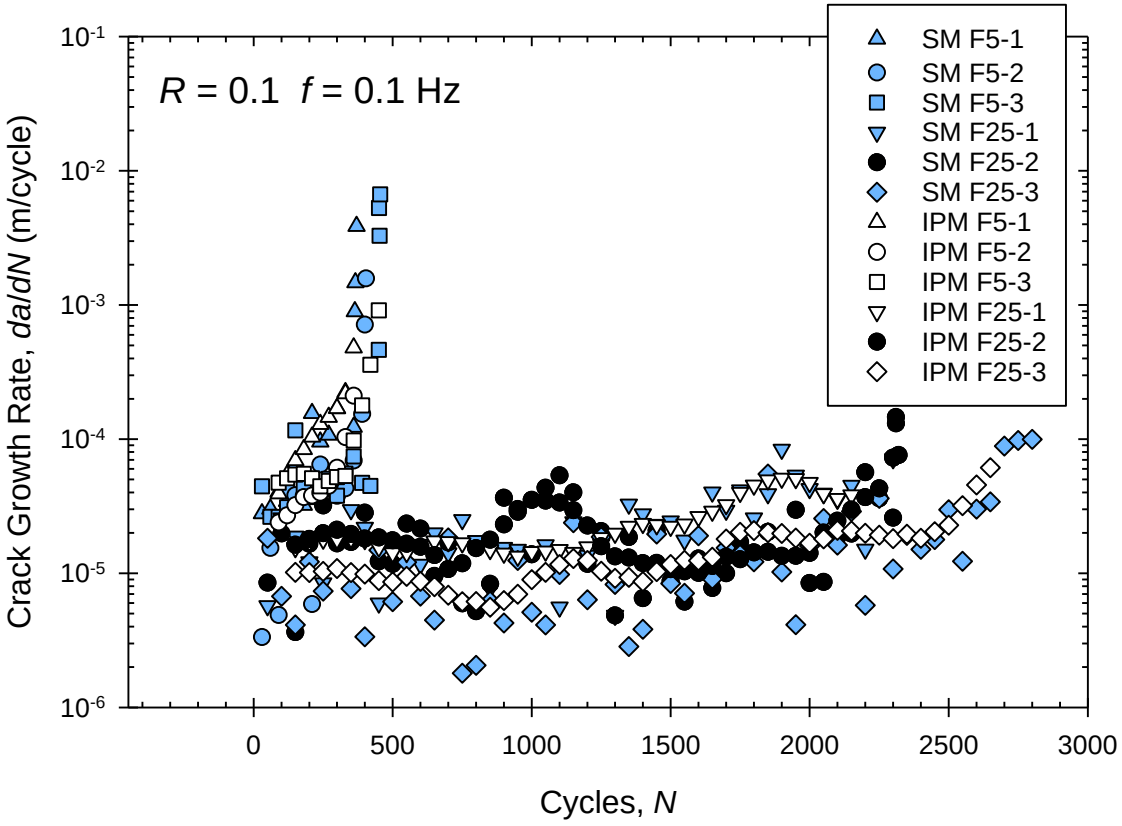

Figure 4.12 – Crack growth rate (m/cycle) versus cycles. SM indicates the secant method. IPM indicates the incremental polynomial method.

The FCG rate, da/dN versus cycles of the 5 and 25°C tests is depicted in Figure 4.12. Following ASTM E647, the da/dN is calculated using both the secant method (SM) and the incremental polynomial method (IPM) [130]. When using SM, the da/dN is inconsistent with no discernable trend. When applying IPM, the noise and uncertainty in the data is reduced and the trends in the da/dN are identifiable. Hereon, IPM is applied.

The da/dN oscillates as the crack progresses. This corresponds to the torturous crack deflection and meandering observed the DIC [133].

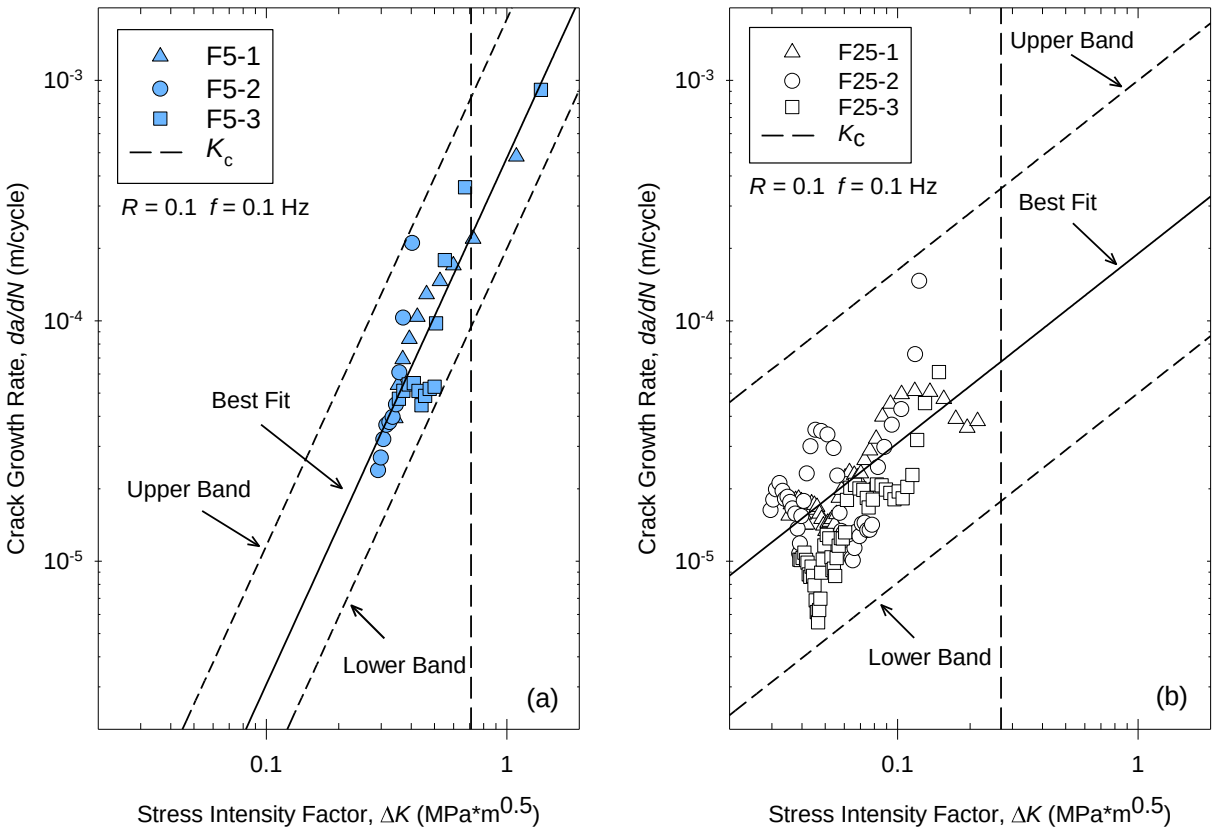

Figure 4.13 – Summary of fatigue crack growth data (a) 5°C and (b) 25°C

The FCG rate, da/dN (calculated using IPM) is plotted with respect to stress intensity factor range, ΔK (calculated using [Eq. (10)]) in Figure 4.13. The "average" K_c is plotted as a vertical dotted line. The da/dN is unstable and increases rapidly to the K_c [132]. In

the 5°C tests, the ΔK generally exceeds the average K_c suggesting that the reported COV of K_c is not conservative. In the 25°C tests, the average K_c is conservative.

The da/dN is modeled using the Paris law

(12) $$da/dN = A(\Delta K)^n$$

where da/dN is the crack growth per cycle (m/cycle), ΔK is the stress intensity factor range $\left(MPa \cdot m^{0.5}\right)$, and A and n are material constants. On a log-log scale, $\log(A)$ is the y-intercept and n is the slope of the curve. The Paris law is applied to compare the intensity of crack growth across isotherms (via the slope, n) and to characterize the uncertainty of crack growth using upper and lower prediction bands (via the y-intercepts, $\log(A)$). The upper and lower prediction bands are the best fit shifted by the y-intercept to encompass the triplicate experiments.

The best fit and prediction bands are shown in Figure 4.13. The Paris law material constants are listed in Table 4.8. The slope, n, decreases as temperature increases; indicating FCG rates are higher at low temperature. The y-intercept, $\log(A)$, decreases as temperature increases; indicating that the FCG threshold, ΔK_{th} is smaller at elevated temperature (i.e. cracks will propagate at a lower ΔK at elevated temperature).

Table 4.8 – Paris law constants

Temp, T (°C)	Upper A, $(\mathrm{m/cycle})$	Best Fit A, $(\mathrm{m/cycle})$	Lower A, $(\mathrm{m/cycle})$	$\Delta\log(A)$	n
5	1.800E-3	4.765E-4	2.000E-4	0.954	2.190
25	1.000E-3	1.903E-4	5.000E-5	1.301	0.788

The uncertainty of crack growth can be estimated using the range of the upper and lower bound y-intercepts, $\Delta\log(A)$ as follows

$$\Delta\log(A) = \log(A_{upper}) - \log(A_{lower}) \tag{13}$$

where $\log(A_{upper})$ and $\log(A_{lower})$ are the constants associated with the upper and lower prediction bands. The $\Delta\log(A)$ is found to increase with temperature; indicating that the FCG rates exhibit larger oscillations and larger inconsistences from specimen-to-specimen at elevated temperature. The increased instability corresponds to lower strength in the asphalt matrix and at asphalt-aggregate interfaces.

In continuum mechanics, the minimum representative volume element (RVE) is the smallest volume of matter that can represent the average response of the entire body. For instance, the minimum RVE size in polycrystalline metals is on the order of a few grains while the size in fissured rock could be on the order of meters or tens of matters [134]. For asphaltic materials, the large aggregates embedded in the asphaltic matrix cause the RVE size to be as large, if not larger, than the specimen size. Consider the DCT specimen shown in Figure 4.3. The heterogeneous aggregates in the ligament area

do not represent an RVE, in fact, a safe estimate of the RVE size would be a 90^3 mm^3. In this study, microstructural mechanics are dominant.

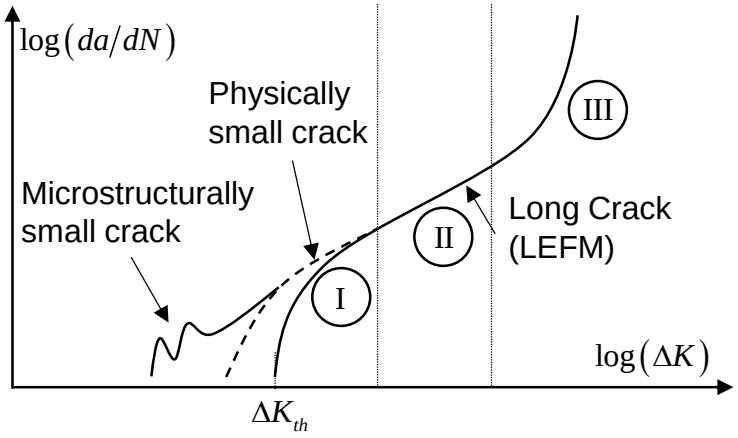

Figure 4.14 – Typical crack growth rate behavior of microstructurally small, physically small, and long cracks

Fatigue crack growth can generally be divided into three regions (I, II, and III) called short, stable, and unstable crack growth as illustrated in Figure 4.14 [132]. Depending on the size of the initial crack length, a_I and subsequently the initial stress intensity range, ΔK_I three distinct FCG curve can be generated relating to long, physically-small, and microstructurally-small cracking behavior. Note: “small” is a misnomer as it indicates the scale of the initial crack length relative to the minimum RVE size. For bodies with long cracks, where the initial crack length is >10x the RVE size, there exists a threshold

stress intensity range, ΔK_{th}, below which the crack will not grow. For bodies with physically small cracks, where the initial crack length is <10x of the RVE size, the FCG rates are much higher and cracks grow at a ΔK below the ΔK_{th}. For microstructurally small cracks, where the initial crack length is near ≤ 1 RVE, FCG rates are even faster and extremely sensitive to the microstructure. Microstructurally small cracks are charaterized by ocsllations in the da/dN. This discontinuous crack growth is associated with the crack interacting with microstructural obstacles/weak zones contributing to the intermittent acceleration and deceleration of the crack. The da/dN data in Figure 4.13 shows that the HMA is dominated by microstructurally small crack growth (particularly in the tests conducted at 25°C).

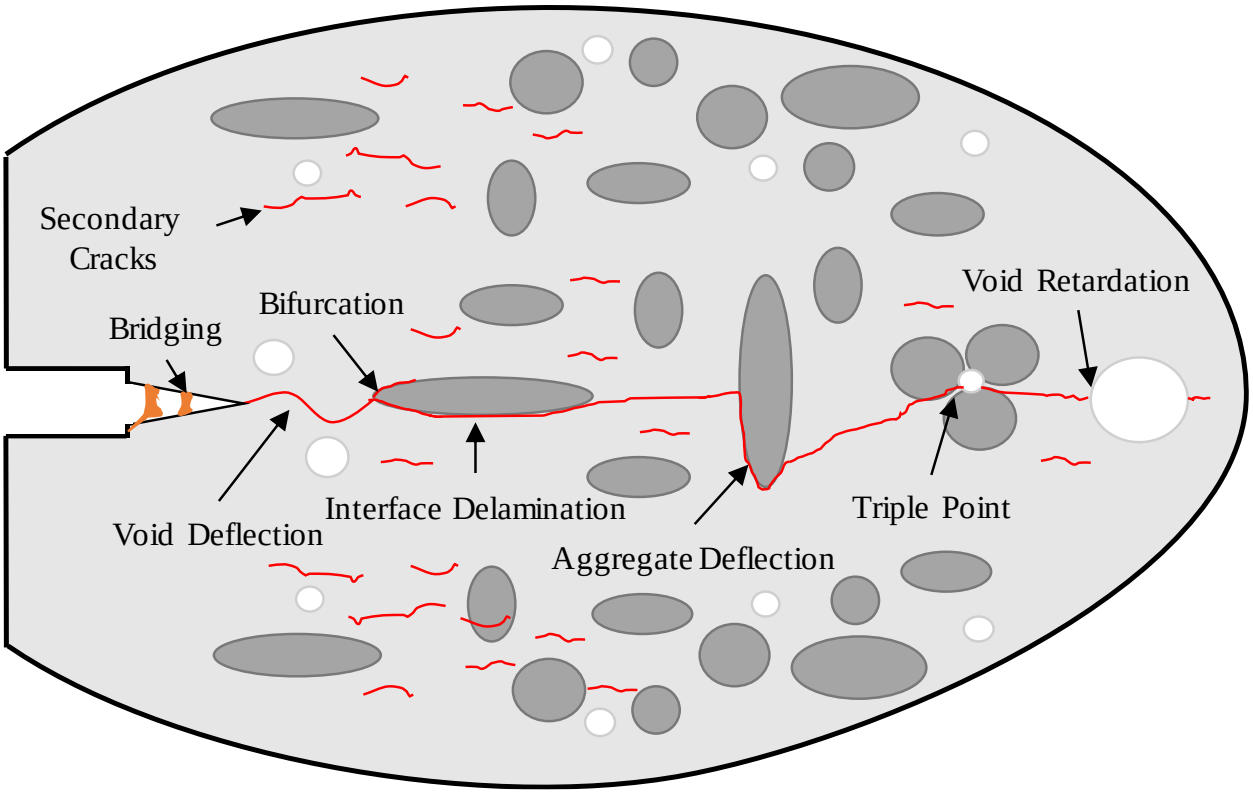

Figure 4.15 – Cracking mechanisms in HMAs

When examining results of DIC, many competing cracking mechanisms are apparent as illustrated in Figure 4.15. The primary crack propagates on the lowest energy path through the material. The size, shape, orientation, and distribution of aggregates, defects, and voids play a dominant role in FCG. Crack tip bridging can occur where the asphalt matrix remains intact behind the crack tip retarding FCG. Hard aggregates behind the crack tip can inhibit crack closure and accelerate FCG. Voids act as stress concentrators and are energy-free surfaces, attracting and deflecting the primary crack. When the crack encounters long aggregates, it has a propensity to bifurcate with the

dominant crack propagating along the asphalt-aggregate interface. The crack deflects around tall aggregates retarding FCG. When aggregates are tightly placed, the crack tends to travel through voids (double & triple points) that exist between aggregates. Large voids tend to arrest or retard the primary crack until it can reinitiate. Depending on the intensity of the stress concentration at these voids, it's possible for primary crack to propagate at the void first. Secondary cracks form at weak zones in the asphalt matrix and asphalt-aggregates interfaces. Gross plasticity can become the dominant failure mechanism at elevated temperature. Overall, the fatigue process zone includes many complex cracking mechanisms that contribute to crack propagation to fracture.

4.8. **CONCLUSIONS**

The objective of this study is to demonstrate that DIC can be employed to tracking crack propagation and produce more accurate measurements of the fracture and fatigue resistance of HMAs. Fracture and fatigue crack growth tests were performed on a dense-graded HMA mixture in the DCT configuration according to a mixture of AASHTO and ASTM standards. Tests were performed at 5, 25, and 40°C respectively. It is determined that

- Digital image correlation can be employed to capture the crack propagation, crack tip remodeling, fatigue process zone, and strain distribution on the surface of specimens.

- The 5°C FCG tests are distinguished by brittle fatigue and fracture where the high strength matrix contribute to fatigue crack growth resistance. The slope of the da/dN curve is high indicating that a minor change in the stress intensity produces a dramatic increase in the crack growth rate while the intercept is high suggesting that there exists a high threshold stress intensity range below which cracking will not occur. Little crack extension occurs before fracture.
- The 25°C FCG tests are distinguished by ductile fatigue and fracture where the low strength matrix contribute to less fatigue crack growth resistance. The slope of the da/dN curve is low indicating that a minor change in the stress intensity range produces a moderate increase in the crack growth rate while the intercept is low suggesting that there exists a low threshold stress intensity range below which cracking will not occur. A significant amount of crack propagation occurs before fracture.
- There exists a critical temperature (between 25 and 40°C) above which FCG experiments (and subsequently DIC) cannot be employed due to excessive plasticity deformation and secondary crack formation.
- Microstructurally-small FCG occurs in the HMA. This type of cracking is extremely sensitive to the microstructure. Many microstructural cracking mechanisms are observed. The complex combination of accelerating and retarding cracking mechanisms contributes to the tortuous, deflective, and bifurcative cracking observed in the experiments.

Overall, DIC is found to be a useful tool for tracking crack propagation and produces accurate measurements and insightful observation of the fracture and fatigue resistance of HMAs.

4.9. **REFERENCES**

[81] Braham, A., and Underwood, B. S. (2016). State of the Art and Practice in Fatigue Cracking Evaluation of Asphalt Concrete Pavements.

[82] ASTM. D7460-10 Standard Test Method for Determining Fatigue Failure of Compacted Asphalt Concrete Subjected to Repeated Flexural Bending 2010:1-14.

[83] AASHTO. TP321-17 Standard Method of Test for Determining the Fatigue Life of Compacted Asphalt Mixtures Subjected to Repeated Flexural Bending 2017:1-12.

[84] Rowe, G.M., Blankenship, P. & Bennert, T. (2012) Fatigue assessment of conventional and highly modified asphalt materials with ASTM and AASHTO standard specifications. Proceedings of the Third Conference on Four Point Bending, Davis, CA, 17-18 September 2012, pp. 113–122.

[85] Underwood, B.S., Kim, Y.R. and Guddati, M.N., "Improved Calculation Method of Damage Parameter in Viscoelastic Continuum Damage Model," International Journal of Pavement Engineering, 11 (6): 459-476.

[86] Underwood, B. S. (2016). A continuum damage model for asphalt cement and asphalt mastic fatigue. International Journal of Fatigue, 82, 387-401.

[87] AASHTO. TP107-14 Determining the Damage Characteristic Curve of Asphalt Mixtures from Direct Tension Cyclic Fatigue Tests 2014:1-14.

[88] Sabouri, M., and Kim, Y. R. (2014). Development of a Failure Criterion for Asphalt Mixtures Under Different Modes of Fatigue Loading. Transportation Research Record: Journal of the Transportation Research Board, 2447, 117-125.

[89] AASHTO. TP101-12 Estimating Fatigue Resistance of Asphalt Binders Using the Linear Amplitude Sweep 2012: 1-8.

[90] Safaei, F., Castorena, C., and Kim, Y.R., (2016) "Linking asphalt binder fatigue to asphalt mixture fatigue performance using viscoelastic continuum damage modeling," Mechanics of Time Dependent Materials, 20(3): 299-323.

[91] Safaei, F., Lee, J., Nascimento, L. A. H., Hintz, C, and Kim, Y.R., "Implications of Warm-Mix Asphalt on Long Term Oxidative Aging and Fatigue Performance of Asphalt Binders and Mixtures," Journal of the Association of Asphalt Paving Technologists, Vol. 83, 2014, pp.143-170.

[92] TxDOT Designation: TEX-248-F. Overlay Test. Construction Division, Texas Department of Transportation, 2017.

[93] Zhou, F., S. Hu, T. Scullion, *et al.* (2007). Development and Verification of the Overlay Tester Based Fatigue Cracking Prediction Approach, *Journal of Association of Asphalt Paving Technologists*, Vol. 76, pp. 627-662.

[94] Moghadas Nejad, F., Aflaki, E., & Mohammadi, M. A. (2010). Fatigue behavior of SMA and HMA mixtures. Construction and Building Materials, 24(7), 1158-1165.

[95] The British Standards Institution, "BS EN 12697-24:2012. Bituminous mixtures — test methods for hot mix asphalt. Part 24: Resistance to fatigue," The British Standards Institution, 2012.

[96] Stewart, C. M., Reyes, J. G., & Garcia, V. M. (2017). Comparison of fracture test standards for a super pave dense-graded hot mix asphalt. Engineering Fracture Mechanics, 169, 262-275.

[97] Stewart, C. M., Oputa, C. W., & Garcia E. (2017). Effect of Specimen Thickness on the Fracture Resistance of Hot Mix Asphalt in the Disk-Shaped Compact Tension (DCT) Configuration, Construction and Building Materials, (accepted for publication).

[98] Zhou, F. et al, (2010) Development, Calibration, and Verification of a New Mechanistic-Empirical Reflective Cracking Model for HMA Overlay Thickness Design and Analysis, Journal of Transportation Engineering Volume 136 Issue 4 - April 2010

[99] Zhou, F., S. Hu, and T. Scullion (2010). Advanced Asphalt Overlay Thickness Design and Analysis System, *Journal of Association of Asphalt Paving Technologists (AAPT)*, Vol. 79, Sacramento, CA.

[100] Yasser Koohi and Robert L. Lytton, (2013) New Methodology to Find the Healing and Fracture Properties of Asphalt Mixes Using Overlay Tester

[101] Gu, F., Y. Zhang, X. Luo, R. Luo, and R. L. Lytton (2015a). Improved Methodology to Evaluate Fracture Properties of Warm Mix Asphalt Using Overlay Test. Transportation Research Record: Journal of the Transportation Research Board, No. 2506, pp. 8-18.

[102] Gu, F., X. Luo, Y. Zhang, and R. L. Lytton (2015b). Using Overlay Test to Evaluate Fracture Properties of Field- Aged Asphalt Concrete. Construction and Building Materials, Vol. 101, pp. 1059-1068.

[103] Cao, W., Mohammad, L.N., Elseifi, M. (2016b) "Assessing the Effects of RAP/RAS and Warm Mix Technologies on Fatigue Performance of Asphalt Mixtures and Pavements Using the Viscoelastic Continuum Damage Approach," Road Materials and Pavement Design, submitted.

[104] Mobasher, B., Mamlouk, M. S., & Lin, H. M. (1997). Evaluation of crack propagation properties of asphalt mixtures. Journal of Transportation Engineering, 123(5), 405-413.

[105] Stempihar, J. "Development of the C* Fracture Test for Asphalt Concrete Mixtures." Order No. 3559647, Arizona State University, Ann Arbor, 2013.

[106] Tschegg, E. K., Jamek, M., & Lugmayr, R. (2011). Fatigue crack growth in asphalt and asphalt-interfaces. Engineering Fracture Mechanics, 78(6), 1044-1054.

[107] Read, J. M. (1996). Fatigue cracking of bituminous paving mixtures (Doctoral dissertation, University of Nottingham).

[108] Hartman, A. M., & Gilchrist, M. D. (2004). Evaluating four-point bend fatigue of asphalt mix using image analysis. Journal of materials in civil engineering, 16(1), 60-68.

[109] Nguyen, M. T., Lee, H. J., & Baek, J. (2012). Fatigue analysis of asphalt concrete under indirect tensile mode of loading using crack images. Journal of Testing and Evaluation, 41(1), 148-158.

[110] Muniandy, R., Akhir, N. A. B. C. M., Hassim, S., & Moazami, D. (2014). Laboratory fatigue evaluation of modified and unmodified asphalt binders in stone mastic asphalt mixtures using a newly developed crack meander technique. International Journal of Fatigue, 59, 1-8.

[111] Braz, D., Lopes, R. T., & Motta, L. M. G. (2004). Research on fatigue cracking growth parameters in asphaltic mixtures using computed tomography. Nuclear Instruments and Methods in Physics Research Section B: Beam Interactions with Materials and Atoms, 213, 498-502.

[112] Roux, S., Réthoré, J., & Hild, F. (2009). Digital image correlation and fracture: an advanced technique for estimating stress intensity factors of 2D and 3D cracks. Journal of Physics D: Applied Physics, 42(21), 214004.

[113] Pan, B. (2011). Recent progress in digital image correlation. Experimental Mechanics, 51(7), 1223-1235.

[114] Romeo, E. (2013). Two-dimensional digital image correlation for asphalt mixture characterisation: interest and limitations. Road Materials and Pavement Design, 14(4), 747-763.

[115] Kim, Y. R., & Wen, H. (2002). Fracture energy from indirect tension testing. Asphalt Paving Technology, 71, 779-793.

[116] Montepara, A., Romeo, E., Isola, M., & Tebaldi, G. (2011). The role of fillers on cracking behavior of mastics and asphalt mixtures. Journal of the Association of Asphalt Paving Technologists, 80.

[117] Ramos, E., Gutierrez, A., Tirado, C., Stewart, C., Abdallah, I., & Nazarian, S. (2016). Explaining Overlay Tester Results with Digital Image Correlation and Finite Element Analysis. In International Conference on Transportation and Development 2016 (pp. 884-894).

[118] Trivedi, N., Singh, R. K., & Chattopadhyay, J. (2015). Investigation on fracture parameters of concrete through optical crack profile and size effect studies. Engineering Fracture Mechanics, 147, 119-139.

[119] Seo, Y. (2003). A comprehensive study of crack growth in asphalt concrete using fracture mechanics.

[120] Chehab, G. R., Seo, Y., & Kim, Y. R. (2007). Viscoelastoplastic damage characterization of asphalt–aggregate mixtures using digital image correlation. International Journal of Geomechanics, 7(2), 111-118.

[121] Hill, B., & Buttlar, W. G. (2016). Evaluation of polymer modification in asphalt mixtures through digital image correlation and performance space diagrams. Construction and Building Materials, 122, 667-673.

[122] Birgisson, B., Montepara, A., Romeo, E., Roque, R., & Tebaldi, G. (2010). Influence of mixture properties on fracture mechanisms in asphalt mixtures. Road Materials and Pavement Design, 11(1), 61-88.

[123] Gao, L., Ni, F., Ling, C., & Yan, J. (2016). Evaluation of fatigue behavior in cold recycled mixture using digital image correlation method. Construction and Building Materials, 102, 393-402.

[124] AASHTO. T312-15 Preparing and Determining Density of Hot Mix asphalt (HMA) Specimens by Means of the Superpave Gyratory Compactor 2015:1–6.

[125] ASTM Standard D6928 (2015), "Standard Test Method for Preparation and Determination of the Relative Density of Asphalt Mix Specimens by Means of the Superpave Gyratory Compactor," ASTM International, West Conshohocken, PA, 2013, DOI: 10.1520/D6925-15.

[126] ASTM Standard D7313 (2013), " Standard Test Method for Determining Fracture Energy of Asphalt-Aggregate Mixtures Using the Disk-Shaped Compact Tension Geometry," ASTM International, West Conshohocken, PA, 2013, DOI: 10.1520/D7313-13.

[127] ASTM Standard D6931 (2012), " Standard Test Method for Indirect Tensile (IDT) Strength of Bituminous Mixtures," ASTM International, West Conshohocken, PA, 2013, DOI: 10.1520/D6931-12.

[128] ASTM Standard E399 (2012), "Standard Test Method for Linear-Elastic Plane-Strain Fracture Toughness K_{ic} of Metallic Materials," ASTM International, West Conshohocken, PA, 2013, DOI: 10.1520/E399-12E03.

[129] Zofka, A., & Marasteanu, M. (2006). Development of double edge notched tension (DENT) test for asphalt binders. Journal of Testing and Evaluation, 35(3), 1-7.

[130] ASTM Standard E647, 1978 (2015), "Standard Test Method for Measurement of Fatigue Crack Growth Rates," ASTM International, West Conshohocken, PA, 2013, DOI: 10.1520/E0647-15E01.

[131] Aliha, M. R. M., Fazaeli, H., Aghajani, S., & Nejad, F. M. (2015). Effect of temperature and air void on mixed mode fracture toughness of modified asphalt mixtures. Construction and Building Materials, 95, 545-555.

[132] I. Stephens, Ralph, A. Fatemi, R. Stephens, Robert, O. Fuchs, Henry, Metal Fatigue in Engineering, J. Eng. Mater. Technol. (2001) 472. doi:10.1115/1.3225026.

[133] Ritchie, R.O. (1999). Mechanisms of fatigue-crack propagation in ductile and brittle solids. International Journal of Fracture, 100, 55–83.

[134] Rudnick, J.W., Fundamentals of Continuum Mechanics

5. Acknowledgments

The authors would like to thank Steven D. Ambriz, Carlos A. Catzin, Jose L. Coronel, Eduardo Garcia, Victor M. Garcia, Mohammad Shafinul Haque, Chinedu William Oputa, Victor M. Ornelas, and Jesús Gerardo Reyes for their contributions to project. We also would like to thank the Center for Transportation Infrastructure Systems (CTIS), especially their Executive Director Dr. Imad Abdallah and Director Dr. Soheil Nazarian for the use of equipment and materials to prepare HMA samples. We would like to thank the Materials at Extremes Research Group for the use of equipment to complete the mechanical tests.